Particle-identification capability of the straw tube tracker and feasibility studies for the charmed-baryon program with PANDA

Vejdani, Solmaz

university of groningen

Particle-Identification Capability of the Straw Tube Tracker and Feasibility Studies for the Charmed-Baryon Program with $\bar{\text{P}}$ANDA

PhD Thesis

to obtain the degree of PhD at the
University of Groningen
on the authority of the
Rector Magnificus Prof. E. Sterken
and in accordance with
the decision by the College of Deans.
This thesis will be defended in public on
Monday 29th of October 2018 at 11.00 hours

by

Solmaz Vejdani
born on 21st of March 1986
in Tehran, Iran

Supervisors
Prof. N. Kalantar-Nayestanaki
Prof. J. Ritman

Co-supervisors
Dr. J.G. Messchendorp
Dr. P. Wintz

Assessment committee
Prof. Klaus Peters
Prof. Olaf Scholten
Prof. Bernd Krusche

ISBN: 978-94-034-1090-6 (Paperback)
ISBN: 978-94-034-1091-3 (Hardback)
ISBN: 978-94-034-1089-0 (Electronic version)

To my parents

Contents

Chapter 1

Introduction

Ancient Greek philosophers had put forward an atomic theory of matter, based on philosophical considerations. In their view the various phenomena observed in daily life could be explained by the motions and shapes of the indivisible constituents of matter, which they called atoms. This theory, forgotten for a long time, was revived in the nineteenth century through the work of chemists. Yet, even in late nineteenth and early twentieth century there were many scientists who rejected the idea of atoms. The general acceptance of atomic theory only came in 1905 after the publication of Einstein's paper on Brownian motion [1].

It is an irony that by this time new phenomena had been observed which pointed the way to subatomic entities, of which the atoms were presumably made of. In 1897, J. J. Thomson showed that cathode rays, first observed in 1869, are streams of negatively charged particles which were later named electrons [2]. In 1911, Rutherford's observation eventually led to a model of the atom. He proposed that the atom contains a positively charged and heavy nucleus, concentrated at a very small volume at its center [3]. The discovery by Bothe and Becker in 1931 [4], of an uncharged penetrating radiation resulting from the incidence of alpha radiation from polonium onto beryllium or boron or lithium, led to the discovery of the neutron by Chadwick in 1932 [4]. In 1934, Fermi [5] explained beta radiation as the decay of the neutron in the nucleus into a proton, an electron, and a yet undiscovered neutral particle called neutrino [5].

Following the footsteps of the original Geiger-Marsden experiment in 1913 [3], various techniques were developed for the acceleration of charged particles to higher energies and using them to probe the structure of the nucleus. Rolf Wideroe and Ernest Lawrence [6] came up with the idea of passing charged

particles through the same voltage step multiple times. The milestones on the path to present-day accelerators were the discovery of the stability conditions for particle orbits in radially symmetric magnetic fields by Kerst [6] in 1940, the discovery of the principle of phase stability independently by Veksler and McMillan in 1945 and 1946 [6], and the development of strong focusing by Courant, Livingston, and Snyder in 1952 [6]. These led to the construction of the alternating gradient synchrotron in Brookhaven, and with the development of larger accelerators, a bewildering variety of particles, some of which had already been seen in cosmic ray experiments, appeared on the scene [6].

In the previous century, the Mendeleev table was able to reveal the underlying order among the multitude of chemical elements, find the relationship between them, and predict the existence of new elements not seen before. Gradually during the 1960s and 70s, a model was developed that made sense of the particle zoo revealed in experiments done with accelerators, and that was used to predict the existence of new particles; the model which has now come to be known as the Standard Model (SM) of particle physics. Any progress beyond the present SM, requires further and more precise elucidation of the properties of these fundamental particles of nature.

Many researchers all around the world create sophisticated machines to search for the physics within the current SM and understanding the interactions of the particles. One of these machines is the future multi-purpose detector antiProton ANnihilation at DArmstadt ($\bar{\text{P}}$ANDA). $\bar{\text{P}}$ANDA will be one of the key experiments at the future Facility for Antiproton and Ion Research (FAIR), which is under construction in Darmstadt, Germany. The $\bar{\text{P}}$ANDA experiment will explore collisions of an antiproton beam with a fixed proton or nuclear target. The physics program of the $\bar{\text{P}}$ANDA detector focuses on the investigation of the hadron structure and the properties of the underlying strong interaction. $\bar{\text{P}}$ANDA will operate with an antiproton beam with center-of-mass energies of up to $\sqrt{s}$= 5.48 GeV, enabling investigations of hadrons with strange and charm quarks up to excited charmonium states. One particular aspect of the physics program is hadron spectroscopy and in particular the interest is focused towards hidden-charm (charmonium), open-charm spectroscopy, and (strange) baryon spectroscopy. There is a great interest in studying the charmed baryon production, and there are still many unanswered questions about the dynamics, excited states, mass and width of these states. The annihilation of antiprotons with protons in $\bar{\text{P}}$ANDA will produce many charmed baryon states, and it will offer a great opportunity to perform extensive studies of charmed baryons and precise measurements. $\bar{\text{P}}$ANDA has a unique setup among other physics experiments. $\bar{\text{P}}$ANDA will provide unique access to the various physics topics, but it will be challenged by the production of a huge background. To distinguish signal from background events, the detector is designed to have a superb

momentum and energy resolution and equipped with the capabilities to identify various particle types. $\bar{\text{P}}$ANDA is divided into sub-detectors optimized for individual tasks. One of the important tasks is the track reconstruction, that is based on the information obtained from the tracking detectors. $\bar{\text{P}}$ANDA has four main tracking detectors and one of them is the Straw Tube Tracker (STT), a cylindrical-shaped detector consisting of gas-filled tubes. The tasks of the STT are to determine the momenta of charged particles, via a precise spatial reconstruction of particle tracks in combination with a solenoid magnetic field, and to perform particle identification (PID) by measuring the specific energy loss.

This thesis presents Monte Carlo (MC) simulations which performed to investigate the capability of $\bar{\text{P}}$ANDA in charmed baryon production. In addition, the results of tests performed with a prototype STT detector are presented to investigate the electronic readout and tracking and PID performance, as well as to eventually make a decision for the readout of the $\bar{\text{P}}$ANDA STT detector.

The thesis is structured as follows:

Chapter 2 gives a concise introduction into the SM and the strong interaction. In addition, a general overview of the theories, QCD and the physics motivation of studying charmed baryons are highlighted.

Chapter 3 is devoted to the FAIR facility and $\bar{\text{P}}$ANDA. After that, the physics program of $\bar{\text{P}}$ANDA is outlined. Following, the different sub-detectors of the experiment are discussed and finally, the software analysis tools and framework are presented.

In chapter 4, the analysis of the process $p\bar{p} \rightarrow \Lambda_c\bar{\Lambda}_c \rightarrow p^+K^-\pi^+\bar{p}K^+\pi^-$ in $\bar{\text{P}}$ANDA is presented. MC simulated events are reconstructed both inclusively, in which the decay products of only one of the charmed baryons is reconstructed, and exclusively, for which the final states of both baryons are reconstructed. Finally, background-like events are studied and the signal-to-background ratio is evaluated with the aim to evaluate the cross section sensitivity of the signal channel with $\bar{\text{P}}$ANDA.

Chapter 5 discusses the outcome of two different in beam-test measurements with a STT prototype. The experimental setup is described followed by a description of the data analysis procedure and track reconstructions. Finally, the results and conclusions are presented.

Chapter 6 concludes the work of this thesis, summarizes the results and gives an outlook.

Chapter 2

Physics Background

This chapter gives a concise introduction to the basic principles of particle physics and the motivation for the $\bar{\text{P}}$ANDA experiment at FAIR. The details of FAIR and $\bar{\text{P}}$ANDA will be presented in the next chapter. Here, we focus primarily on the underlying physics aspects that motivated the construction of these new facilities.

2.1 Fundamental Forces

Every child, as the marvels of the world unveil in front of his or her curious eyes, seeks the answer of the famous question "What is the world made of?". It is also the question that mankind has pondered about for a long time. The answers to this riddle have ranged from the simple solution offered by the ancient Greek philosophy, which proposed air, water, fire and earth as the building blocks of nature to, later, the well structured table of elements proposed by Mendeleev. All the answers, in spite of their variety, show our quest to describe nature using fundamental building blocks and basic interactions among them. The fundamental forces of nature are the gravitational force, the weak nuclear force, the electromagnetic force and the strong nuclear force. These forces can be classified by their range and strength. We experience the gravitational and electromagnetic forces in our daily life. Gravity and the electromagnetic force have an infinite range. Gravity is the weakest and the electromagnetic force is many times (about 40 orders of magnitude) stronger than gravity. The weak and strong forces are effective only over a very short range and dominate only at the level of subatomic particles. The strong force, as the name suggests, is the strongest of all four fundamental interactions.

2.2 The Standard Model

The Standard Model (SM) of particle physics was proposed around 1970. The SM provides an explanation for sub-nuclear physics phenomena and some aspects of cosmology in the earliest moments of the universe. The SM is conceptually simple and contains a description of the elementary particles and forces. The main elements of the SM were experimentally confirmed culminating with the discovery of the Higgs boson in 2012. The particles involved in the SM, are characterized by their spin, their mass, and the quantum numbers such as (charge) parity. Their electric, weak and strong charges determine the corresponding interaction strength. The SM particles are 12 spin = 1/2 fermions (6 quarks and 6 leptons), 4 spin = 1 gauge bosons and a spin = 0 Higgs boson (see Fig. 2.1).

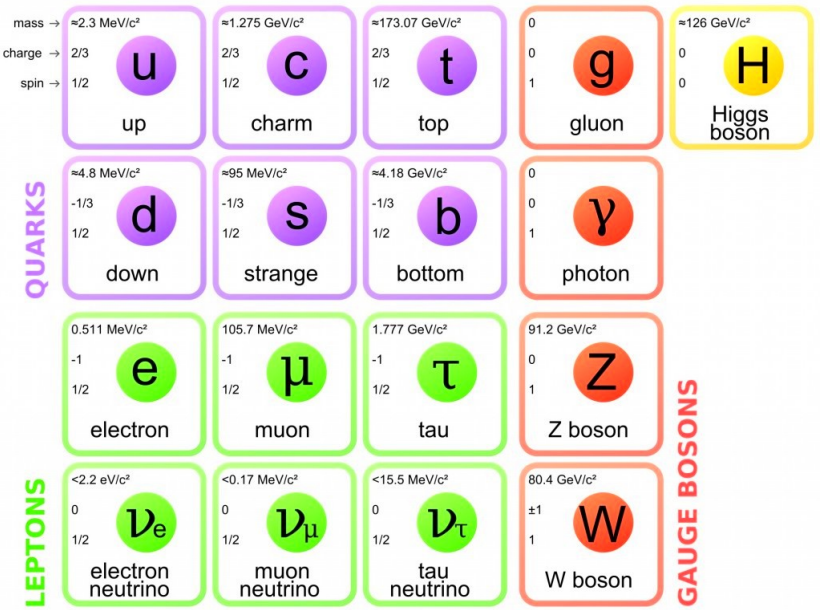

Figure 2.1: Fundamental particles in the Standard Model. The Standard Model consists of elementary particles with the three generations of fermions in the first to third column (purple and green), gauge bosons in the fourth column (red), and the Higgs bosons in the fifth column (yellow). The figure is taken from Ref. [7].

On a mathematical level, the SM is described as a Quantum Field Theory (QFT), with the fundamental quantum fields of the different SM interactions. It follows the successful description of the electromagnetic interactions within the framework of quantum electrodynamics (QED) and expands it for the other interactions. Both the fermions which build up matter and the bosons which mediate the interactions are described by fields, which, when quantized,

gives rise to particles. The interactions between particles enter the theory by demanding that the Lagrangian is gauge invariant under a U(1)× SU(2) × SU(3) symmetry. The electroweak component of the symmetry group, the group SU(2) × U(1), combines the description of electromagnetic and weak interactions. The SU(3) part of the SM originates from the strong interaction mediators. The theory involves one massless mediator particle (the photon) and three massive bosons (W^+, W^-, and Z) [12].

2.2.1 Fermions

The matter surrounding us is built up by fermions, particles with half-integer spin. There are six types of quarks, known as flavors: up, down, strange, charm, top and bottom (labeled in purple in Fig. 2.1). The quarks are strongly interacting particles, while the leptons are not. The six flavors of quarks are also divided into three electroweak SU(2) doublets:

$$\begin{pmatrix} u \\ d \end{pmatrix} \quad \begin{pmatrix} c \\ s \end{pmatrix} \quad \begin{pmatrix} t \\ b \end{pmatrix},$$

where the quarks in the upper and lower row have electric charge $+2/3e$ and $-1/3e$, respectively, with e being the charge of the electron. Flavor can only be changed through the weak interaction. Transitions within the same SU(2) doublet are the most probable, even though transitions between the doublets can happen. The probabilities for transitions between different flavors are given by the CKM matrix [10, 11]. The leptons also form three electroweak SU(2) doublets:

$$\begin{pmatrix} e \\ \nu_e \end{pmatrix} \quad \begin{pmatrix} \mu \\ \nu_\mu \end{pmatrix} \quad \begin{pmatrix} \tau \\ \nu_\tau \end{pmatrix}.$$

The leptons either carry integer electric charge or are neutral. The charged leptons are: electron, muon and tauon in the upper row which have electric charge of $-e$. The electron is the lightest of these particles. The electrical neutral leptons are called neutrinos. Neutrinos have different flavors (ν_e, ν_μ, ν_τ), and each neutrino is paired with a charged lepton. The quarks also, in contrast to the leptons, interact via the strong force. The charge of the strong interaction comes in three colors, which are labeled red, blue and green. The name is given since the charges share the property of color that a combination of them all gives a neutral (white) charge. Due to the naming of its charge after color, the theory of the strong interaction is called Quantum Chromo Dynamics, abbreviated QCD. A quark carries one of these three colors and an antiquark carries one of the corresponding anticolors.

Fermions are organized in three generations with identical quantum numbers and different masses. An SU(2) doublet of quarks together with an SU(2)

doublet of leptons is called a generation and there are thus three generations of fermions. Table 3.4 shows an overview of the fermions of the Standard Model, all with spin $s = 1/2$, sorted into leptons and quarks. The first column describes the elementary charge, q, of the particles of this row. Following, the three generations of leptons and quarks, are ordered by their masses, m. For each fermion an antiparticle exists, summing up to 24 particles in total. Antiparticles have opposite charge-like quantum numbers.

Table 2.1: Overview of the fermions of the Standard Model with their masses and electrical charges, sorted into quarks and leptons and in groups of three generation. Each particle has a spin of 1/2 and an associated antiparticle with opposite charge. In total, 24 fermions are listed in the SM [9]. Mass values (m) are taken from Ref. [8].

Fermions							
		1		2		3	
	q/e	Name	m (keV/c^2)	Name	m (MeV/c^2)	Name	m (GeV/c^2)
Quarks	2/3	u	2300	c	1275	t	173.21
	-1/3	d	4800	s	95	b	4.18
Leptons	-1	e	511	μ	105.7	τ	1.7
	0	ν_e	<0.002	ν_μ	<0.19	ν_τ	<0.018

2.2.2 Bosons

The SM interactions are associated with the exchange of four vector bosons, with one unit of spin. There are five known gauge bosons, namely: γ, W^+, W^-, Z^0 and g.

Table 2.2: Overview of the bosons of the Standard Model , all with integer spin s, sorted by their associated field [9]. Given is also the electrical charge, q, and the mass m. Mass values (m) are taken from Ref. [8]

Associated Field	Boson	$s/\hbar$	q/e	m (GeV/c^2)
Electromagnetic	γ	1	0	0
Weak	$W^\pm$	1	±1	80.4
	Z^0	1	0	91.2
Strong	$g^{(8)}$	1	0	0
Higgs	H	0	0	125.7

The photon is the mediator of the electromagnetic interaction. The gluon mediates strong interactions and the W^+, W^-, and Z^0 mediate weak interactions. The photon and the gluons are massless, while the Z and the W are massive, which is the reason why weak interactions are weak at low energy

(they are suppressed by powers of $E/M_{Z,W}$, where E is the energy of the process). The mass of W is 80.4 GeV/c^2 (80 times heavier than a proton) and the mass of Z is 91.2 GeV/c^2. Despite their weakness, they give rise to distinctive signatures because they violate parity P, charge conjugation C, their combination CP, time-reversal T, and family number, which all are symmetries of the electromagnetic and strong interactions. In particular, the decay of heavier into lighter families is due to weak interactions. Gluons, g, are the mediators of the strong interaction. There are eight types of massless gluons, distinguished by their QCD color charge content. Gluons carry a combination of color and anticolor. Since they carry this charge, they can themselves participate in the strong interaction and self-interact. Self interaction leads to the phenomenon of confinement: Quarks and gluons cannot be measured as isolated particles, they always form composite structures when observed from a distance. Another boson, the Higgs boson (H), is a scalar, spin-less boson. It has a mass of approximately 125 GeV/c^2. The Higgs mechanism and the associated Higgs bosons are essential part of the Standard Model. The Higgs mechanism provides a description on how the W and Z bosons acquire their masses without breaking the local gauge symmetry. It also gives mass to the fundamental fermions. The Higgs boson was predicted within Standard Model already since a long time, until it was finally presented on 4th of July, 2012 by the ATLAS [13] and CMS [15], at the Large Hadron Collider (LHC) at CERN.

2.3 Strong interaction

The strong force is described mathematically by the quantum field theory of QCD, a gauge theory analagous to Quantum Electrodynamics (QED), the theory of the electromagnetic force. Since the $\bar{\text{P}}$ANDA experiment mainly focusses on aspects of the strong interaction, this section highlights this topic in more detail. The modern theory of the strong interaction is called Quantum chromodynamics (QCD). Historically the roots of QCD can be found in nuclear physics, in the description of ordinary matter understanding what protons and neutrons are and how they interact. Nowadays, the physicists use QCD in order to describe most of what goes on at high-energy accelerators such as, the discovery of the heavy W and Z bosons, or of the top quark. They would have a precise and reliable understanding of the more common processes governed by QCD. Physicists still look for other Higgs-like particles predicted by certain models and for manifestations of super symmetry that depend on a detailed understanding of production mechanisms and backgrounds calculated by means of QCD.

2.3.1 Color and QCD

Quantum Chromodynamics describes the strong interaction between the quarks and gluons. It is generally assumed that all fundamental particles are represented by local quantum fields. QCD appears as an expanded version of QED. QED corresponds to a U(1) local gauge symmetry of the universe. The underlying symmetry associated with QCD is the invariance under SU(3) local phase transformation [17],

$$\Psi(x) \rightarrow \Psi'(x) = \exp\left(ig_s\alpha(x)\cdot\hat{\mathbf{T}}\right)\Psi(x). \tag{2.1}$$

In Eq. 2.1, $\hat{\mathbf{T}} = T^a$ are the eight generators of the SU(3) symmetry group, which are related to Gell-Mann matrices by $T^a = 1/2\ \lambda^a$, and $\alpha^a(x)$ are eight functions of the space-time coordinate x. Because the generators of SU(3) are represented by 3×3 matrices, the wave function Ψ must now include three additional degrees of freedom that can be represented by the three component vector in SU(3) flavor symmetry. This new degree of freedom is called color. The states are labeled by convention, red, blue and green. The SU(3) local phase transformation corresponds to rotating states in color space about an axis whose direction is different at every point in space-time. For the local gauge transformation of the Eq. 2.1, the Dirac equation becomes [17],

$$i\gamma^\mu\left[\partial_\mu + ig_s(\partial_\mu\alpha).\hat{\mathbf{T}}\right]\Psi = m\Psi, \tag{2.2}$$

The gauge invariance can be asserted by introducing the eight new fields, ${G_\mu}^a(x)$, where the index $a = 1, 2, ..., 8$, each one corresponds to one of the eight generators of the SU(3) symmetry. The new Dirac equation, including the interactions with the new gauge fields becomes [17],

$$i\gamma^\mu\left[\partial_\mu + ig_s{G_\mu}^a\mathbf{T}^a\right]\Psi - m\,\Psi = 0, \tag{2.3}$$

which is invariant under SU(3) phase transformation provided by the new transform as [17],

$${G_\mu}^k \rightarrow {G_\mu}^{k'} = {G_\mu}^k - \partial_\mu\alpha_k - g_s f_{ijk}\alpha_i\,{G_\mu}^j, \tag{2.4}$$

In Eq. 2.4, the last term appears because the generators of the SU(3) symmetry do not commute. The parameters f_{ijk} refer to the structure contents of the SU(3) group. Because these SU(3) generators do not commute, QCD is known as a non-Abelian gauge theory. The presence of the additional term give rise to gluon self-interactions. Fig. 2.2 shows the corresponding Feynman diagrams representing triple and quartic gluon vertices. The eight new fields G^a are called gluons, that mediate the strong force. The quark-gluon interaction

appears in Eq. 2.3, from the term of qqg interaction vertex [17],

$$g_s T^a \gamma^\mu G_\mu{}^a \Psi = g_s \frac{1}{2} \lambda^a \gamma^\mu G_\mu{}^a \Psi. \tag{2.5}$$

The self-interaction of gluons lead to the phenomena of confinement. Quarks and gluons cannot be observed in an isolated state. In Eq. 2.5, g_s, is the interaction strength associated with the QCD coupling constant, $\alpha_s = {g_s}^2/4\pi$. The coupling constant of QCD, varies depending on the momentum, energy or distance scale, it is evaluated at. Its value drops significantly when the scale becomes much smaller than the size of the proton, corresponding to high-momentum scale; see Fig. 2.3. The variation of α_s enables the possibility to describe accurately data from particle physics experiment at very high energies, e.g. the LHC experiments, using perturbative methods [18].

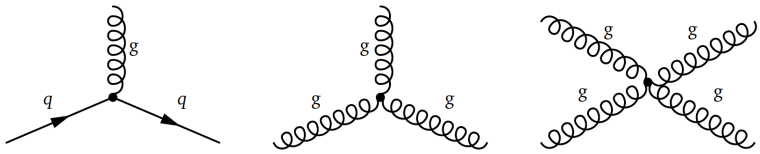

Figure 2.2: The predicted QCD interaction vertices from the requirement of SU(3) gauge invariance. From left to right: quark-gluon interaction, three-gluon interaction, four-gluon interaction. Figure is taken from Refs. [8, 17]

2.4 Hadrons

Strongly-interacting particles, the hadrons, are bound states of quark and gluon fields. Hadrons are categorized by their number of constituting quarks into two groups of baryons and mesons. Hadrons provide a rich experimental environment for the study of the strong interaction, from details of the resonance spectrum to form factors and transition decays via electromagnetic probes. These studies provide information on the underlying substructure of bound states by resolving, in a non-trivial way, the quarks and gluons of which they are composed. Quarks, with spin 1/2, are strongly interacting fermions. By convention, quarks have positive parity and antiquarks have negative parity. Quarks have the additive baryon number 1/3, antiquarks $-1/3$. Table 5.8 summarises the other additive quantum numbers (flavors) for the three generations of quarks. They are related to the charge Q through the generalized Gell-Mann-Nishijima formula [19]:

$$Q = I_z + \frac{B' + S + C + B + T}{2}, \tag{2.6}$$

where Q is in units of the elementary charge e and B' is the baryon number. The flavor of a quark has the same sign as its charge, by convention.

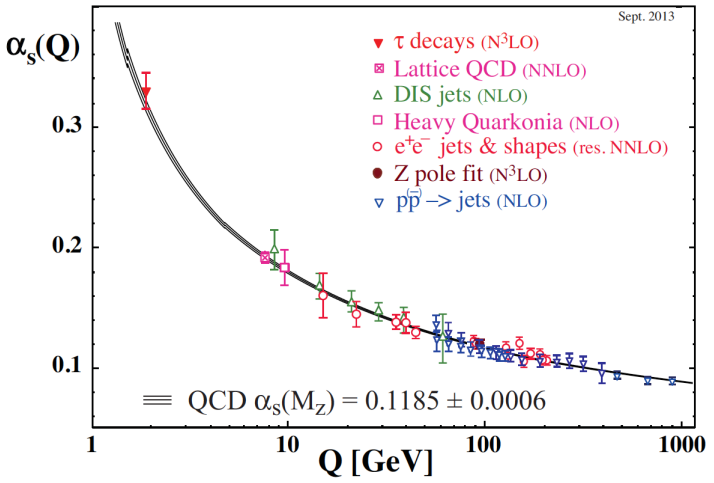

Figure 2.3: Summary of measurements of the coupling constant of QCD, α_s, as a function of the energy scale Q. The different data points employ perturbative theories up to different levels of perturbation in their extraction of the values: NLO refers to next-to-leading order corrections, NLO next-to-leading order corrections, and so on. α_s is usually evaluated at the scale of the mass of the Z boson, $\alpha_s(M_Z) = 0.1185 \pm 0.0006$. Figure is taken from Ref. [16].

Table 2.3: Additive quantum numbers of the quarks. Here, the notations are defined as: Q: electric charge (in units of the elementary charge e), I: isospin, I_z: third component of isospin , S: strangeness, C: charm, B: bottomness and T: topness.

	d	u	s	c	b	t
Q	$-1/3$	$+2/3$	$-1/3$	$+1/3$	$-1/3$	$+2/3$
I	$1/2$	$1/2$	0	0	0	0
I_z	$-1/2$	$+1/2$	0	0	0	0
S	0	0	-1	0	0	0
C	0	0	0	$+1$	0	0
B	0	0	0	0	-1	0
T	0	0	0	0	0	$+1$

2.4.1 Mesons

The mesons have integer spins with the baryon number $B' = 0$. In the quark model, they are $q\bar{q}$ bound states of quarks q and antiquarks $\bar{q}$ (the flavors of q and $\bar{q}$ may be different). If the orbital angular momentum of the $q\bar{q}$ state is l then the parity P is $(-1)^{l+1}$. The meson spin J, is given by the usual relation $|l - s| \leq J \leq |l + s|$, where s is 0 (antiparallel quark spins) or 1 (parallel

quark spins). The charge conjugation, or C-parity, $C = (-1)^{l+1}$, is defined only for the $q\bar{q}$ states made of quarks and antiquarks of the same flavor-type. For mesons made of quarks and their own antiquarks (isospin $I_z = 0$), and for the charged $u\bar{d}$ and $d\bar{u}$ states (isospin $I = 1$), the C-parity can be generalized to the G-parity, $\mathrm{G} = (-1)^{I+l+s}$. The mesons are classified in J^{PC} multiplets. The 1^{--} states are the vectors and, the $l = 0$ states are the pseudoscalars (0^{-+}). The orbital excitations $l = 1$ are the scalars (0^{++}), the axial vectors (1^{++}) and (1^{+-}) , and the tensors (2^{++}). Radial excitations n_r are denoted by the principal quantum number n, as $n = l + n_r + 1$. The very short lifetime of the t quark prevents it from forming into bound-state hadrons [8, 32].

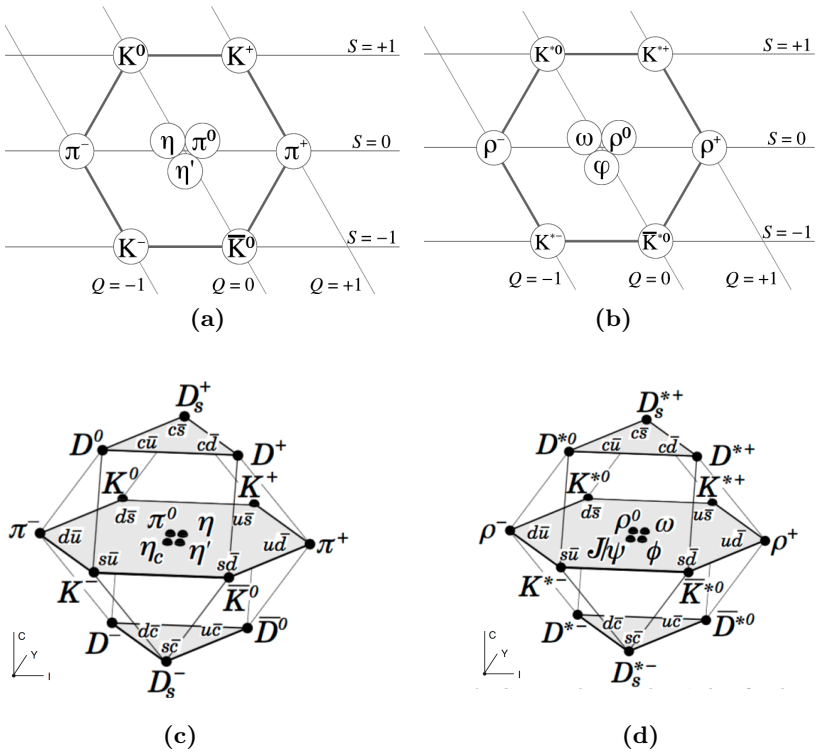

Figure 2.4: SU(3) and SU(4) weight diagrams. SU(3) weight diagrams (top) showing the ground state mesons without orbital angular momentum (l =0), consisting of the three lightest quarks (u, d, and s). (a) shows nine sates of mesons with $J^P = 0^-$, and (b) represents the the mesons with $J^P = 1^-$. The figures in the bottom represent the SU(4) weight diagrams, consisting of the 16-plets, for the pseudoscalar and vector mesons (c), and (d) respectively. They are made of the u, d, s, and c quarks. In the bottom figures, I, C and Y refer to isospin, charm and hyper charge, respectively. Figures are taken from Refs. [8, 20, 24, 25].

The symmetry is a fascinating feature of the quark model. The nine possible $q\bar{q}$ combinations containing the light u, d, and s quarks, by following SU(3),

are grouped into a singlet of light quark and an octet mesons:

$$3 \otimes \bar{3} = 8 \oplus 1. \tag{2.7}$$

A charm quark c can be included, as a fourth quark, and extends SU(3) to SU(4). SU(3) is also broken and the only reasonable symmetry is isospin, e.g. SU(2). However, SU(4) is also badly broken owing to the much heavier c quark. Nevertheless, in an SU(4) classification, the sixteen mesons are grouped into a 15-plet and a singlet [32]:

$$4 \otimes \bar{4} = 15 \oplus 1. \tag{2.8}$$

The ground state mesons without orbital angular momentum ($l = 0$) consisting of the three lightest quarks (u, d, and s) are shown in Fig. 2.4 (a),(b). The weight diagrams for the ground-state pseudoscalar (0^+) and vector (1^{--}) mesons which also include c-quarks, such as D^0, are depicted in Fig. 2.4 (c),(d). Moreover, there are now many 4-quark candidate states found in nature, such as the ones reported by BESIII [21], LHCb [22] and DØ experiment [23].

2.4.2 Baryons

Baryons are fermions with baryon number $B' = 1$ and half-integer spin which are assumed to be bound states of three quarks. The antibaryons are assumed to be the corresponding bound states of three antiquarks. So far, all established baryons are 3-quarks $|qqq\rangle$ configurations, although very recently a $J/\Psi p$ resonance observed at the LHCb experiment which possibly originates from a $|qqqq\bar{q}\rangle$ pentaquark state [26]. In 2011, the WASA at COSY experiment found a possible multiquark state [27], which was interpreted as a hidden color six-quark state [28]. This experimental observation was confirmed in another process [29]. However, the nature of this state is still unclear. Besides the six-quark state, it can also be regarded as a di-baryon system, i.e. a $\Delta\Delta$ bound state, or a mixture of both configurations. Quarks are fermions, so the baryon wave function must be overall antisymmetric under quark interchange. Baryons are color singlets, and so have an antisymmetric color wave function. In the ground state, the orbital angular momentum L is zero (S-wave) and the spatial wave function is symmetric. This wave function consists of four parts

$$\Psi = \psi(space)\phi(flavor)\chi(spin)\xi(color). \tag{2.9}$$

Therefore, for ground-state baryons, the product of the spin and flavor wave functions must also be symmetric. So, both wave functions can be fully symmetric, or both can have mixed symmetry with the product being symmetric. The three flavors imply an approximate flavor SU(3), which requires that

baryons made of these quarks (u, d, and s) belong to the multiplets on the right side of

$$3 \otimes 3 \otimes 3 = 10_S \oplus 8_{M_s} \oplus 8_{M_A} \oplus 1_A. \tag{2.10}$$

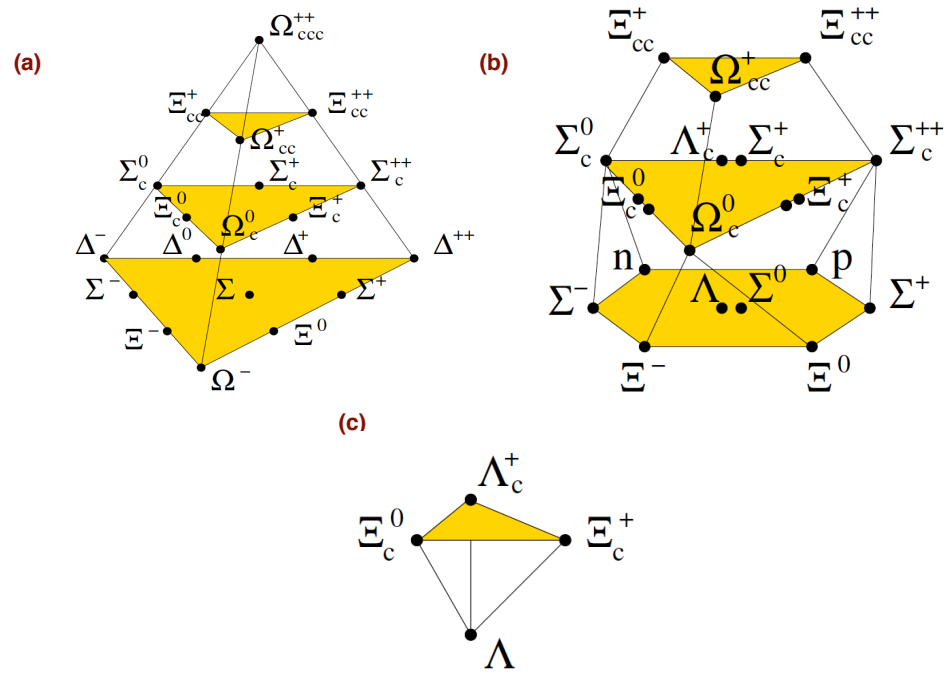

Figure 2.5: (a) The symmetric 20_S-plets of SU(4), showing the SU(3) decuplet on the lowest layer. (b) The mixed-symmetric 20_M-plets, (c) and the and the antisymmetric 4 of SU(4). The 20-plets has the SU(3) octet on the lowest layer, while the 4 has the SU(3) singlet at the bottom. Figure is taken from Ref. [32].

The subscripts describe the symmetry properties of the wavefunctions; S/A means symmetric/antisymmetric with respect to the interchange of any two of the quarks, while M_S/M_A means mixed symmetry properties [32]. In flavor SU(3), the baryon multiplets that arise from $3 \otimes 3 \otimes 3$ are the well-known decuplet (containing the Δ), a singlet and two octets (containing the nucleon). The corresponding multiplet structure [32] for SU(4) is

$$4 \otimes 4 \otimes 4 = 20_S \oplus 20_{M_S} \oplus 20_{M_A} \oplus \bar{4}_A. \tag{2.11}$$

The symmetric 20_S-plet contains the decuplet as a subset, forming the ground floor of the weight diagram (shown in Fig. 2.5 (a)), and all the ground-state

baryons in this multiplet have $J^P = \frac{3}{2}^+$. The mixed-symmetric 20_M-plet (shown in Fig. 2.5 (b)) contains the octets on the lowest level, and all the ground-state baryons in this multiplet have $J^P = \frac{1}{2}^+$. The ground-floor state of the $\bar{4}$ (shown in Fig. 2.5 (c)) is the singlet Λ state with $J^P = \frac{1}{2}^-$ [32].

2.5 Charmed baryons and the $\bar{\text{P}}$ANDA experiment

Charmed baryons are a category of baryons including at least one charm valence quark. Shortly after the discovery of J/ψ, the first charmed baryon was detected in 1975, the $\Lambda_c{}^+$, at the BNL [34], followed by the discovery of $\Xi_c{}^+$ in 1976 at FNAL [35]. Since the first observation in the 1970s, a large number of distinct charmed baryon states have been identified and currently, 20 charmed baryons are present in the Particle Data Group (PDG) summary tables [8].

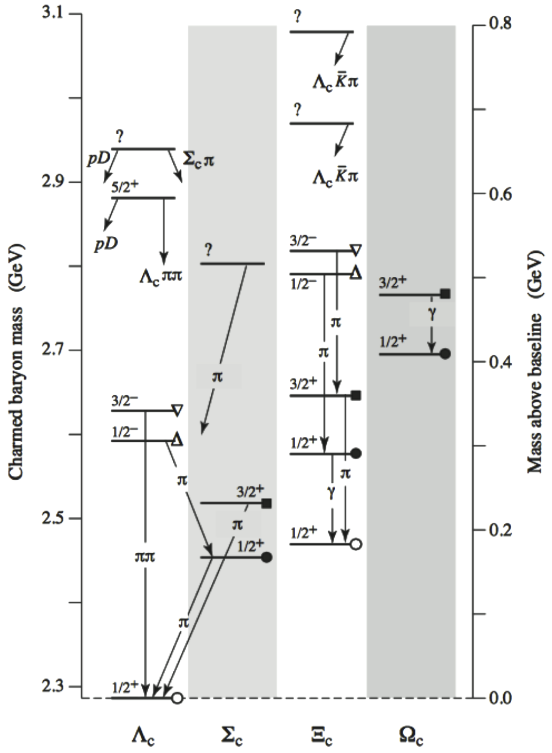

Figure 2.6: The spectra of known singly-charmed baryons and their mass splittings. Figure is taken from Ref. [8].

Baryons with two heavy quarks are predicted to exist and some preliminary results from the SELEX experiment at FermiLab [36] indicate they have been seen. In 2017, the detection of a baryon containing two charm quarks has been

made by physicists working on the LHCb experiment at the Large Hadron Collider (LHC) at CERN. With a mass of 3621 MeV/c^2, the ${\Xi_{cc}}^{++}$ particle has about the same mass as a helium-3 nucleus. The ${\Xi_{cc}}^{++}$ was created in proton collisions at 7 TeV and 13 TeV in HLCb. ${\Xi_{cc}}^{++}$ was identified via its decay into a ${\Lambda_c}^{+}$ baryon and three lighter mesons: the K^-, π^+ and π^+ [37]. Recent years have seen great advances in our understandings of the charmed baryons. The B-factories, in particular the Belle and BaBar experiments, have been successful in making a wide variety of first observations of excited singly-charmed baryons . The current best knowledge of the spectra of singly-charmed baryons is given in Fig. 2.6. The spin-parity assignments of many of the observed states are still to be discovered [40, 41, 42]. The "doubly charmed" baryons are rare and will be neglected in this discussion.

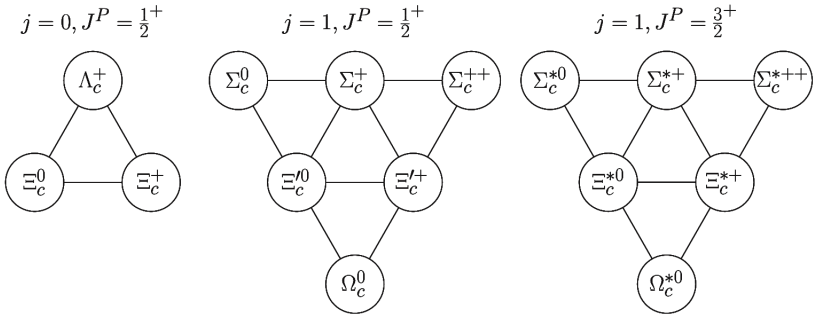

Figure 2.7: The spectra of known singly-charmed baryons and their mass splittings. Figure is taken from Ref. [8].

A singly-charmed baryon consists of a heavy c quark and a light diquark with spin-parity J^P. There are four possibilities for the flavor content of the diquark, by assuming isospin symmetry and letting q denote a u or a d. These four possibilities are: qq with isospin 0 (flavor antisymmetric), qq with isospin 1 (flavor symmetric), sq with isospin 1/2 (either), and ss with isospin 0 (flavor symmetric). These correspond to the Λ_c, Σ_c, Ξ_c, and Ω_c states, respectively. The diquark wave function must be antisymmetric under quark interchange. Its color wave function is antisymmetric and its spatial wave function is symmetric, in the ground state. So it may be either flavor-symmetric and spin-symmetric ($J^P = 1^+$) or flavor-antisymmetric and spin-antisymmetric ($J^P = 0^+$) [33]. Combining the diquark with the charm quark gives rise to the possible states illustrated in Fig. 2.7. In this figure, the multiplets of the full SU(3) symmetry, formed by the u, d, and s quarks, are shown. Those with $J^P = \frac{1}{2}^+$ are all members of the same multiplet as the proton, and those with $J^P = \frac{3}{2}^+$ are all members of the same multiplet as the Δ and Ω. There is a second isospin doublet of Ξ_c states with $J^P = \frac{1}{2}^+$, denoted Ξ_c' [33].

2.5. Charmed baryons and the $\bar{\text{P}}$ANDA experiment

Over the last several years, experimental and theoretical studies of charmed baryons have been the focus of research. Singly and doubly heavy baryon spectroscopy, in particular, have received significant attention. In addition to the previous discoveries, there are still many states of heavy and doubly heavy baryons remaining to be discovered. The new Beijing Spectrometer (BESIII), by accumulating large numbers of events, helps us to understand more about charmed hadrons. The LHCb and the antiProton ANnihilation at DArmstadt ($\bar{\text{P}}$ANDA) experiment, at FAIR, are also expected to provide new results to help experimentally map out the heavy-baryon sector.

The $\bar{\text{P}}$ANDA experiment will explore collisions from an antiproton beam with a fixed proton target. Antiproton-proton annihilation enables a wide range of produceable particles that cannot be directly created in e^+e^- colliders. If protons and antiproton collide at sufficiently high energy, the light quark-antiquark pairs might annihilate, and s or c quark-antiquark pairs may be created. At the hadron scale, this means that a hyperon-antihyperon pair is created. The momentum range between 1.5 GeV/c and 15 GeV/c is chosen to produce states in the overlap of perturbative and non-perturbative QCD regimes. The center-of-mass energies from $\sqrt{s}$= 2.26 GeV to $\sqrt{s}$= 5.48 GeV, are well above the threshold for all of the multi-strange and the lightest charmed baryons. This means that multi-strange and charm-rich baryons can be produced and used to study extensively their properties and interaction dynamics. It is feasible to assess the exclusive production of baryons such as $p\bar{p} \to \Lambda_c\bar{\Lambda}_c$.

The physics program of the $\bar{\text{P}}$ANDA detector focuses on the investigation of the hadron structure and the properties of the strong interaction. Hadron spectroscopy is one of the main topics of the $\bar{\text{P}}$ANDA physics program, and in particular the interest is focused on the charmonium, open-charm spectroscopy and the baryon spectroscopy. Hence, there is a great interest in studying the charmed baryon production in the proton-antiproton collisions to be measured by the $\bar{\text{P}}$ANDA experiment. This thesis investigates the feasibility to study the charmed baryons, by simulating the production of the Λ_c baryons production, $p\bar{p} \to \Lambda_c\bar{\Lambda}_c$. The Λ_c baryon plays a significant role in understanding both charm and bottom baryons. As the lightest charm baryon, the Λ_c is common to many decays of the more massive baryons. The Σ_c states decay strongly through pion emission directly to Λ_c, as this is the only kinematically allowed strong decay. Baryons containing a bottom quark, decay weakly to states including a charm baryon. It is through the decay to a Λ_c that bottom baryons are most often detected.

Chapter 3

$\bar{\text{P}}$ANDA Experiment at FAIR

In this chapter, the next generation hadron physics experiment, $\bar{\text{P}}$ANDA is presented. The $\bar{\text{P}}$ANDA (Anti**P**roton **AN**ihilation at **DA**rmstadt) experiment, will be one of the key experiments at the future **F**acility for **A**ntiproton and **I**on **R**esearch (FAIR). The FAIR facility is under construction adjacent to GSI Helmholtz Center for Heavy Ion Research in Darmstadt, Germany. $\bar{\text{P}}$ANDA will use an antiproton beam with a momentum between 1.5 GeV/c and 15 GeV/c, interacting with various internal targets. The antiproton beam will be provided by HESR, the **H**igh **E**nergy **S**torage **R**ing in FAIR. The FAIR accelerator complex is introduced in section 3.1. The $\bar{\text{P}}$ANDA physics program is highlighted in section 3.2. Subsequently, the $\bar{\text{P}}$ANDA detector and the $\bar{\text{P}}$ANDA analysis software framework are presented in section 3.3, 3.4 and 3.5, respectively.

3.1 Overview of FAIR

FAIR is a new international laboratory, under construction at the existing GSI site near Darmstadt in Germany. FAIR, the largest European research infrastructure and a unique research center with ions and antiprotons is currently under construction. A variety of physics experiments will be conducted at FAIR. The experiments are structured into four pillars, thereby covering different scientific areas and physics programs:

- **A**tomic, **P**lasma, and **A**pplied **P**hysics (APPA).
- **C**ompressed **B**aryonic **M**atter (CBM).
- **NU**clear **ST**ructure, **A**strophysics and **R**eactions (NUSTAR).

- Anti**P**roton **An**nihilation at **DA**rmstadt ($\bar{\text{P}}$ANDA).

Figure 3.1 shows the existing GSI site together with the future FAIR; the existing GSI facility is shown in blue and the new facility is in red. An overview of the experiments at FAIR is provided and summarized in Table 3.4. Using a complex accelerator chain with various routes, FAIR will be able to provide different types of beams with the intention to serve in parallel different experiments. As shown in Fig. 3.1, FAIR consists of different accelerators: linear accelerators, synchrotron and storage rings. Three synchrotrons are responsible for increasing the energy of protons and ions produced in the linear accelerators. Two distinct linear accelerators, UNILAC and p-LINAC accelerate ions and protons, respectively, for the injection into SIS18. SIS18 is the first ring accelerator in the accelerator's chain for accelerating of ions and protons. The acceleration is done in two possible modes: namely with a fast ramp rate of 10 T/s up to 12 Tm maximum magnetic bending power (magnetic rigidity), or with 4 T/s to a higher maximum bending power of 18 Tm. SIS18 gets its name from its maximum magnetic rigidity of 18 Tm. The main accelerator for FAIR is SIS100. Ions and protons, pre-accelerated by SIS18, are brought to beam energies of 2.7 AGeV (U^{28+}) and 29 GeV (protons). 4×10^{11} ions per pulse or 2×10^{13} protons per cycle can be accelerated and compressed to bunch lengths of 60 ns and 25 ns, respectively. SIS100 has a circumference of 1084 m and gets its name from its magnetic rigidity of 100 Tm [45]. SIS300 is another synchrotron which is located next to SIS100. SIS300 will have a magnetic rigidity that is a factor of three larger than SIS100. It will be used for additional acceleration of ion beams and to store beams for slow extraction while SIS100 is accelerating beams for other experiments. The accelerator will be equipped with 6 T magnets, ramping at 1 T/s. SIS300 is not part of the planned initial start version of FAIR. The further preparation of the different beams such as storing, accumulation and cooling is performed by a number of rings.

The **C**ollector **R**ing (CR) collects antiprotons and ions from SIS100 and Super-FRS, respectively, and pre-cools the beams stochastically. Normal conducting dipoles are used for this task in a ring of ∼211 circumference. In addition, the CR will be used as a mass spectrometer for short-lived isotopes in an isochronous mode, employing an internal Time-Of-Flight (TOF) detector [46]. The antiprotons are extracted and accumulated in the **R**ecuperated **E**xperimental **S**torage **R**ing (RESR) and the ions are transferred to the **N**ew **E**xperimental **S**torage **R**ing, (NESR). The RESR is dedicated to accumulation and deceleration of antiprotons and short-lived ions. The ring surrounds the CR and has a circumference of 245 m. Up to 10^{11} antiprotons at a fixed energy of 3 GeV can be accumulated and cooled in the RESR. The antiprotons are either transferred to NESR or into the **H**igh **E**nergy **S**torage **R**ing (HESR).

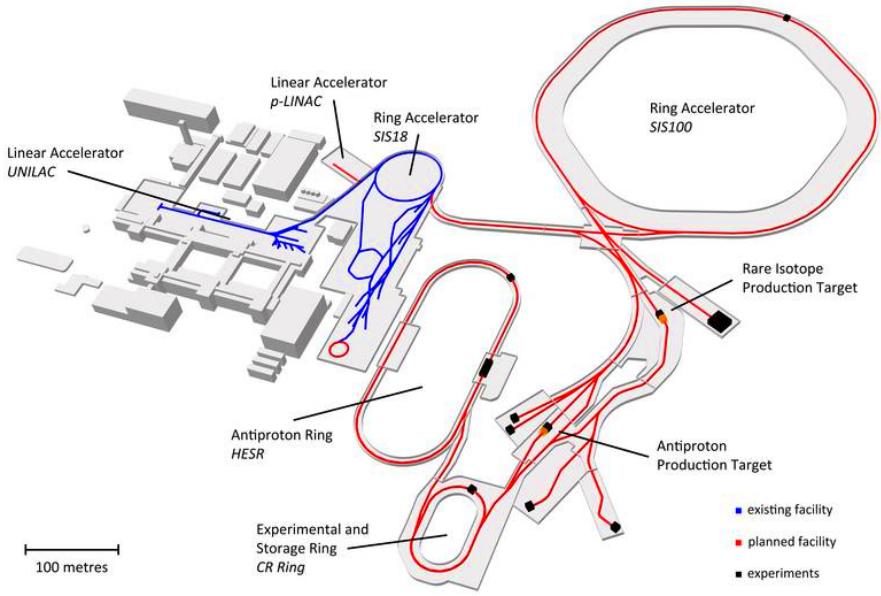

Figure 3.1: The future FAIR facility with different accelerators and experiments annotated. On the left side, the existing buildings of GSI are located. The accelerator chain outlined in blue is already existing, the red chain is planned for FAIR. This figure corresponds to the start version of FAIR. It does not show SIS300, RESR and NESR. Figure is taken from Ref. [43].

The RESR is also not part of the initial start version of FAIR. The NESR is a storage ring for stable and unstable ions and antiprotons. Different experimental facilities are connected to NESR and make use of its high-intensity beams. NESR can receive its beam from various sources. Stable ions can be delivered by SIS100 or SIS300, unstable ions by RESR, CR, or directly by Super-FRS and antiprotons by RESR or CR. The circumference of NESR will be 222 m, including four straight sections of 18 m each. In one straight section, NESR will join with an electron ring (eA Collider). The HESR, shown in Fig. 3.2, is an antiproton synchrotron and storage ring designed for the momentum range of 1.5 to 15 GeV/c. The antiprotons are injected into the HESR, which is capable of collecting and then accelerating or decellerating them [47]. The components of the FAIR complex are grouped into six modules to enable an expeditious start of FAIR. The first four modules (0-3) compose of FAIR's initial version, the so-called Modularized Start Version (MSV) [51]. They include the mandatory accelerator components of SIS100 and the connection to the existing GSI essential (both module 0) as well as the experimental halls for CBM, High-Acceptance DiElectron Spectrometer (HADES), and Atomic, Plasma Physics and Applications (APPA) (module 1) and Super Fragment Separator (Super-FRS) (module 2). The antiproton infrastructure is included in module 3, comprising the storage rings CR and HESR as well as the hall for

P̄ANDA. Within the Modularized Start Version (MSV), RESR will not be built initially and will not be available for antiproton accumulation at the start-up of FAIR. Only CR is available for pre-cooling and collection of antiprotons.

3.1.1 High Energy Storage Ring (HESR)

P̄ANDA is located in one of the HESR's straight sections, see Fig. 3.2. HESR is designed for experiments with antiprotons of high energies. It is the main ring used at the initial stage of FAIR. A proton beam is produced in the p-LINAC and further accelerated with SIS18 and SIS100. At the antiproton production target, antiprotons are created. They are collected and cooled in CR and RESR and then transferred to HESR. Since RESR is absent in the initial version of FAIR, a combination of CR and HESR is used to prepare the beam.

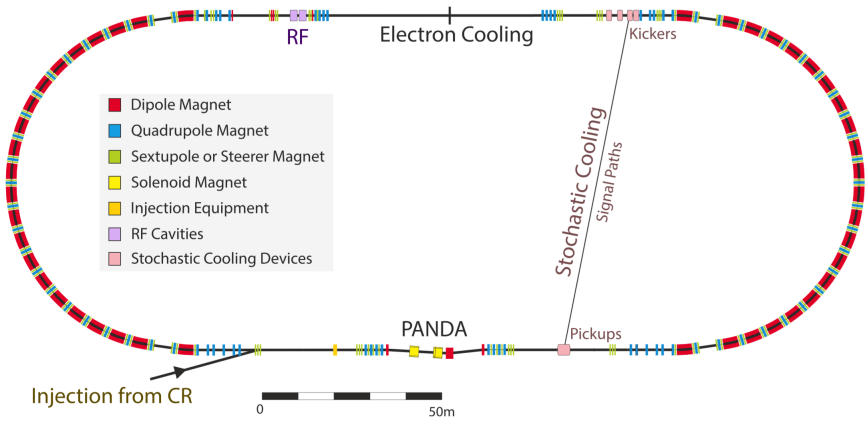

Figure 3.2: Schematic view of the High-Energy Storage Ring (HESR). The P̄ANDA experiment will be located in the lower straight section. Figure is taken from Ref. [44].

The antiprotons are generated by impinging a primary proton beam of 28 GeV onto a metal target. Behind the target, the antiprotons are collected in a magnetic horn and separated from collision residue particles in a subsequent 58 m long beam line. Thirteen quadrupoles and two sextupoles modify the beam to match the properties needed for injection into CR. The target itself has a length of roughly 10 cm and it is made of either copper, nickel, or iridium. The material is chosen to be not too light, in order to produce a sufficient number of antiprotons in a short distance, but also to be not so dense that it melts under the deposited proton energy [48].

The circumference of the HESR ring is 574 m. It has two straight sections

of 132 m each and 44 dipole magnets with a total maximum bending power of 50 Tm. The desired beam quality and beam intensity will be prepared for two different operation modes, namely the high-luminosity (HL) and high-resolution (HR) modes. In the high luminosity (HL) mode a peak luminosity of 2×10^{32} cm^2 s^{-1} is attained with 10^{11} antiprotons and a target thickness of 4×10^{15} atoms/cm^2. It should be available in the whole energy range of the HESR with a momentum spread of $\Delta p/p \leqslant 10^{-4}$. More stringent requirements are necessary in the high resolution (HR) mode with an expected momentum resolution of $\Delta p/p \approx 4 \times 10^{-5}$. Here a peak luminosity of 2×10^{31} cm^2 s^{-1} can be attained with 10^{10} antiprotons. A high-resolution beam is particularly beneficial for high precision line-shape analyses of charmonium(-like) states. To obtain an antiproton beam with a small momentum spread, the beam must be cooled. Cooling is a process to shrink the size, divergence, and energy spread of charged particle beams without removing particles from the beam. To accomplish these goals, two beam cooling methods are foreseen namely, stochastic cooling and electron cooling. Stochastic cooling uses the electrical signals produced by the circulating beam to drive an electro-magnetic device, usually an electric kicker, that will kick the bunch of particles to reduce the momentum of a group of particles. These individual kicks are applied continuously and over an extended period of time. This beam cooling method has the advantage that the longitudinal and transversal spreads of the beam are reduced. Systems for stochastic cooling are installed in both straight sections. The signal pickups are located downstream of $\bar{\text{P}}$ANDA, the beam kickers at the beginning of the next straight section [53]. Using the electron cooling method, the phase space of stored antiprotons can be compressed by aligning the antiproton beam with a cold dense electron beam. HESR will be equipped with an electron cooler with relativistic energies up to 4.5 MeV located in the straight section opposite of $\bar{\text{P}}$ANDA [9, 49, 50]. HESR has methods for antiproton accumulation, but the particle numbers needed for the high luminosity mode cannot be reached without additional accumulation in RESR: instead of 10^{11}, only 10^{10} antiprotons will circulate in the ring. Consequently, HESR will only run in high resolution mode in the MSV. Also, the duty cycle of $\bar{\text{P}}$ANDA is lowered, as HESR needs time for antiproton accumulation, in which no physics experiments can occur. The duty cycle will be less optimum and it will result in maximum luminosities of order 10^{31} cm^2 s^{-1}. The scheme for antiprotons reaching $\bar{\text{P}}$ANDA in the MSV is as follows: Protons from SIS100 create antiprotons at the antiproton production target. 10^8 antiprotons are collected in CR. They are cooled for 10 s, then transferred to HESR. There, the antiprotons are cooled, while the next 10^8 antiprotons are collected in CR. After 10 s cooling, the CR antiprotons are, again, transferred to HESR. This procedure is repeated 100 times until 10^{10} antiprotons are accumulated in HESR [9, 52].

3.2 Physics Program of $\bar{\text{P}}$ANDA

The $\bar{\text{P}}$ANDA experiment will explore collisions of an antiproton beam with a fixed proton or nuclear target. Antiproton-proton annihilations enable the production of a wide range of hadrons that cannot be created directly in e^+e^- colliders. The physics program of the $\bar{\text{P}}$ANDA detector focuses on the investigation of the hadron structure and the properties of the underlying strong interaction. The momentum range between 1.5 GeV/c and 15 GeV/c is chosen to produce states in the overlap of perturbative and non-perturbative QCD regimes with center-of-mass energies from $\sqrt{s}$= 2.26 GeV to 5.48 GeV. Hadron spectroscopy is one of the main topics of the $\bar{\text{P}}$ANDA physics program, and in particular the interest is focused towards hidden-charm (charmonium) and open-charm spectroscopy, and (strange) baryon spectroscopy. The $\bar{\text{P}}$ANDA detector will also be used to search for gluonic excitations and to study further QCD dynamics. Another important topic of the physics program is the investigation of nucleon structure. Finally, there will also be investigations of the properties of hadrons in nuclear matter and searches for (double) hypernuclei. Fig. 3.3 represents the mass range of hadrons accessible at the HESR with antiproton beams.

3.2.1 Hadron Spectroscopy

One of the key physics programs of $\bar{\text{P}}$ANDA focuses on the measurements and classification of hadrons and the hadronic bound-state spectrum. Special attention is given to mesons with charm content as well as to baryons with strange and charm content. Mesons with open charm (D, D_s), charmonium states like the J/ψ, strange and charmed baryons, and the search for signs of new physics are the topics of interest.

Charmonium Spectroscopy

Charmonium spectroscopy refers to precise measurements of mass, width, decay branches of all charmonium states with the aim to extract information on the details of the quark-confinement potential. Charmonium is a bound state of a charm quark and its antiquark ($c\bar{c}$). Below the threshold for ($D\bar{D}$) production ($\sqrt{s}$ = 3.73 GeV), the spectrum consists of eight states. All eight charmonium states are predicted and observed, but the measurement of their parameters and decays is far from complete. Charmonium spectroscopy will provide new insights to the fundamental understanding of strong interactions. The results of the charm and anti-charm quark ($c\bar{c}$) spectroscopy will help to tune the potential models of mesons. The most accurate measurements have been obtained for the vector ($J^{PC} = 1^{--}$) states (ψ). These can be formed

directly at e^+e^- colliders. With an antiproton beam, charmonium states of all (conventional) quantum numbers could be formed directly and the precision of the mass and width measurement depends only on the beam quality.

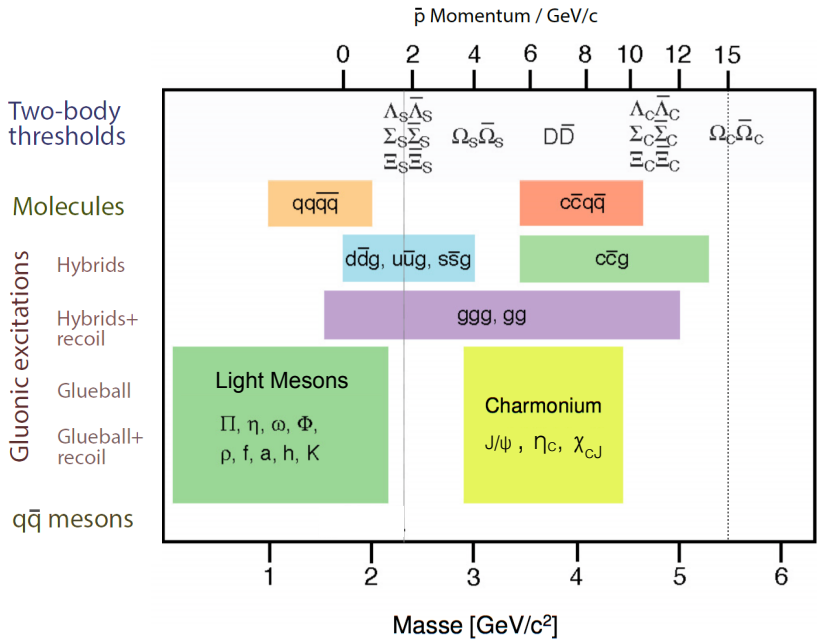

Figure 3.3: The mass range of hadrons accessible at the HESR with antiproton beams. The figure indicates the antiproton momenta required for charmonium spectroscopy, the search for charmed hybrids and glueballs, the production of D-meson pairs and the production of Σ baryon pairs for hypernuclear studies. The range within the two dotted lines is accessible by HESR. The antiproton beam momentum is given on the top axis with the corresponding center-of-mass energies on the bottom axis, a part of the figure is taken from Ref. [54]. The antiproton beam momentum is well above the threshold for all of the multi-strange and the lightest charmed baryons. So, it is possible to assess the exclusive production of baryons such as $p\bar{p} \to \Lambda_c\bar{\Lambda}_c$. The feasibility studies of this specific channel are presented in chapter 4.

$\bar{\text{P}}$ANDA will contribute with a resonance scan, measuring masses and widths with a very high precision. $\bar{\text{P}}$ANDA will run with an improved beam-momentum resolution compared to the previous charmonium-targeted experiments at Fermilab (E760 and E835). $\bar{\text{P}}$ANDA will consist of a variety of specialized detectors and sub-detectors with greater spatial coverage and magnetic field. Besides the conventional $c\bar{c}$ bound states, many narrow charmonium-like resonances, known as the "XYZ" states, have been discovered in the recent years. For the XYZ states, "X" stands in general for all unassigned particles, "Y" specifies the $J^{PC} = 1^{--}$ states which are found in e^+e^- mode and "Z" labels the charged states. Various models proposed by theorists for the XYZ res-

onances include conventional quarkonium, quarkonium hybrids, quarkonium tetraquarks, meson molecules, etc.. So far, none of the models has provided a compelling pattern for the XYZ states. Additional hints will be given by future experiments like $\bar{\text{P}}$ANDA, which is going to measure their properties in the center-of-mass energy range below 5.48 GeV. Masses of the charmonium as well as many XYZ states lie within this energy range.

Open-Charm Spectroscopy

Besides the charmonium spectroscopy program, the open-charm spectroscopy will be an integral part of the physics program of $\bar{\text{P}}$ANDA. Open charm mesons (called D mesons) consist of a charm and a light constituent quark. These hadrons are complementary objects for studying the properties of the strong interaction. D mesons combine the aspect of the heavy quark as a static color source on one side and the aspect of chiral symmetry breaking and restoration due to the presence of the light quark on the other. Since a light quark and a heavy quark are bound together, such mesons can be seen as the hydrogen atom of QCD. The quark model was capable of describing the spectra of D mesons with reasonable accuracy and even of making predictions, until two new resonances, $D_s(2317)$ and $D_s(2460)$ were found at BELLE [55], BABAR [54] and CLEO [56]. HESR running with full luminosity at momenta larger than 6.4 GeV/c would produce large numbers of D meson pairs. $\bar{\text{P}}$ANDA, will perform threshold scans to enable high precision measurements of the masses and widths of these recently discovered states and contribute to solving the open problems.

Baryon Spectroscopy

Besides meson spectroscopy, also baryons will be investigated with $\bar{\text{P}}$ANDA. An understanding of the baryon spectrum is one of the primary goals of the non-perturbative QCD. For many baryon states, listed by the PDG, the properties like mass and width as well as the different decay channels are measured. Often, they are missing sufficient amount of data and have been seen only qualitatively. The baryon spectroscopy of light-quark baryons is pursued intensively at electron accelerators. Whenever the baryons contain strange or even charm quarks, the data become extremely sparse. For instance, the properties of Ξ resonances were not significantly improved since the 1980s [57]. Baryons containing heavy strange quarks like the Λ and Σ ($|S|= 1$), Ξ ($|S|= 2$), and Ω ($|S|= 3$), provide an interesting laboratory for studying QCD. For excited heavy baryons the data sets are typically too small. This is the main reason for limited knowledge of radially and orbitally excited states. In contrast to ground states, whose properties are in good agreement with the quark model,

the spectrum of excited states is much less clear. The $\bar{\text{P}}$ANDA experiment is well-suited for a comprehensive baryon spectroscopy program, in particular in the spectroscopy of (multi-)strange and possibly also charmed baryons. A particular advantage of using antiprotons in the study of (multi-)strange and charmed baryons is that in antiproton-proton annihilation no additional kaons or D mesons are required for strangeness or charm conservation. The baryons can be produced directly close to the threshold, which reduces the number of background channels, for example compared to high-energy $p\bar{p}$ collisions [44]. The very poorly known Ω spectrum [58] can also be studied at $\bar{\text{P}}$ANDA, and no experimental data exist for the reaction $p\bar{p} \to \Omega\bar{\Omega}$. In $p\bar{p}$ collisions, a large fraction of the inelastic cross section is associated with channels resulting in a baryon anti-baryon pair in the final state. For reactions such as $p\bar{p} \to \Lambda_c\bar{\Lambda}_c$, and $\Sigma_c\bar{\Sigma}_c$, no experimental data exist and they are also expected to be accessible at $\bar{\text{P}}$ANDA. Table 3.4 shows the expected production cross sections and corresponding detection rates for the various $p\bar{p}$ collisions that result in hyperon-baryon production. The numbers in the table are achieved from the simulation of the reactions in the framework of $\bar{\text{P}}$ANDA at the phase one with the luminosity of 10^{31} cm^2 s^{-1}. The aim of this thesis to investigate the capability of $\bar{\text{P}}$ANDA in charmed baryon production via the decay channel $p\bar{p} \to \Lambda_c\bar{\Lambda}_c$. The results are presented in chapter 4.

Table 3.4: Cross sections and reconstructed event rates for various reaction channels produced in $p\bar{p}$ collisions. The numbers in tables [97] are achieved from the simulations of the reactions in the framework of $\bar{\text{P}}$ANDA at phase-1.

Momentum (GeV/c)	Reaction	σ (μm)	Efficiency (%)	Rate (with 10^{31}cm^2 s^{-1})
4	$p\bar{p} \to \bar{\Lambda}\Sigma^0$	~ 40	$\sim$30	~ 50 s^{-1}
4	$p\bar{p} \to \Xi\bar{\Xi}$	~ 2	$\sim$20	$\sim$1.5 s^{-1}
12	$p\bar{p} \to \Omega\bar{\Omega}$	~ 0.002	$\sim$30	~ 4 h^{-1}
12	$p\bar{p} \to \Lambda_c\bar{\Lambda}_c$	~ 0.1	$\sim$35	~ 2 d^{-1}

Gluonic Excitations

Hadronic states bound together by an excited gluon field, such as glueballs, hybrid mesons, and hybrid baryons, are a potentially rich source of information concerning the confining properties of QCD. Interest in such states has been sparked by observations of resonances with exotic 1^{-+} quantum numbers [59] at Brookhaven. The glueball spectrum in general is not well understood. There is lack of experimental data and ab-initio (QCD-based) theoretical prediction that go beyond a quenched approximation [62]. Lattice QCD calculations predict 15 glueball states accessible with the momentum range of HESR. The ground state is $J^{PC} = 0^{++}$ and the first excitation is at $J^{PC} = 2^{++}$ [59]. The

masses are expected to be around 1.7 GeV/c^2 and 2.4 GeV/c^2, respectively, although the calculations still have large uncertainties. Glueballs with an exotic quantum number configuration that are not feasible just with quarks are called oddballs. Out of the 15 mentioned states, two are oddballs: $J^{PC} = 2^{+-}$ and $J^{PC} = 0^{+-}$. Decays of glueballs include channels going to ϕ, η and J/ψ states. The momentum region of $\bar{\text{P}}$ANDA is suitable for finding some of the proposed states. Since the annihilation of quarks with anti-quarks will produce gluons in the intermediate state, the production cross section of gluon-rich hadrons is expected to be large. So the $p\bar{p}$ annihilations are a distinguished setup for finding the lighter, heavier and regular glueballs more easily and potentially allow to collect more statistics compared to existing measurements [54].

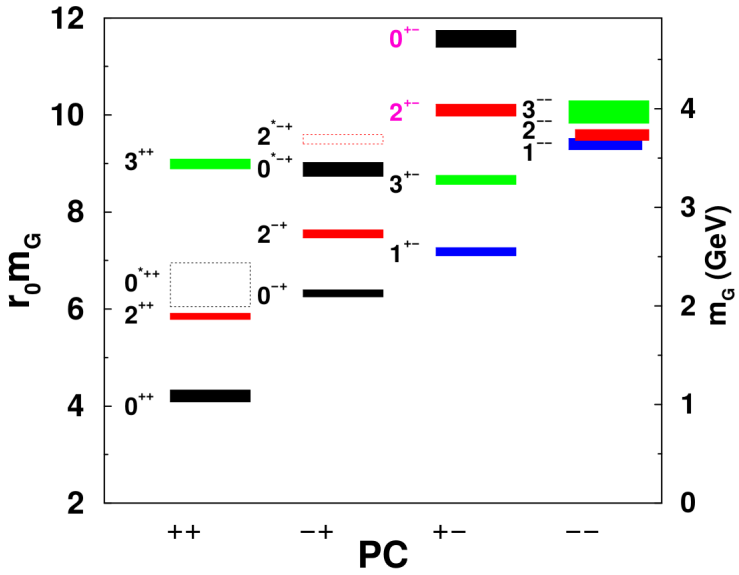

Figure 3.4: The mass spectrum of glueballs from lattice-QCD calculation [62]. The masses are given in terms of the hadronic scale r_0 along the left vertical axis and in units of GeV along the right vertical axis (assuming ${r_0}^{-1} = 410(20)$ MeV). The locations of states whose interpretation requires further studies are indicated by the dashed hollow boxes. Figure is taken from Ref. [59].

3.2.2 Nucleon Structure

A wide area of the physics program of $\bar{\text{P}}$ANDA concerns studies of the non-perturbative region of QCD. In addition to the hadron spectroscopy, $\bar{\text{P}}$ANDA is also well suited to investigate the quark and gluon distributions of the ground state of the nucleon, the proton. The inclusive deep-inelastic scattering can be used to study quark and anti-quark distributions in the nucleon via a measurement of the forward virtual Compton amplitude. With the antiprotons from

the HESR it will be possible to study the crossed-channel Compton scattering of the exclusive $p\bar{p}$ annihilation into two photons. It has been shown that the space-like process can be well described with the model of Generalized Parton Distributions (GPDs) [63, 64, 65]. GPDs developed in the recent years, are accessible via $p\bar{p}$ annihilations using a so-called handbag approach. The wide-angle Compton scattering processes ($p\bar{p} \to \gamma\gamma$) can be divided in parts described by GPD (soft parts), and parts for which a perturbative QCD approach is valid, as the involved photon has very high momentum (hard parts). The high luminosity and sub-detector configuration (especially the Electromagnetic Calorimeter (EMC)) enables $\bar{\text{P}}$ANDA to probe the nucleon structure by studying $p\bar{p} \to \gamma\gamma$. Additional nucleon structure analysis at $\bar{\text{P}}$ANDA will be achieved by studying the Transverse Parton Distributions (TPDs) in the dilepton Drell-Yan processes ($p\bar{p} \to l^+ l^- X$). The Drell-Yan production of muon pairs in proton-antiproton collisions, is a useful tool to access transverse spin effects within the nucleon [54, 66]. Drell-Yan processes allow for analysis of momenta of quarks bound in a nucleon. Pure dilepton final states, $p\bar{p} \to e^+e^-$ and $p\bar{p} \to \mu^+\mu^-$ give access to the time-like region of the proton form factor and allow for the independent extraction of the electric and magnetic form factors (G_E) and (G_M), respectively, and provide insight into non-perturbative and QCD regimes likewise.

3.2.3 Hadrons in Matter

Besides the study of antiproton-proton collisions, $\bar{\text{P}}$ANDA will also investigate the effects of hadrons implanted into nuclear matter. $\bar{\text{P}}$ANDA can be used for the study of antiproton-nucleus collisions by replacing the frozen hydrogen cluster-jet target by a solid wire or fibre target made of carbon ^{12}C or other materials. The antiproton-nucleus collisions at $\bar{\text{P}}$ANDA offer a very promising opportunity to study the properties of the hadrons inside the matter and the nuclear medium. A special focus of these investigations is the modification of the rest mass and lifetime of hadrons in nuclear matter, which is expected due to a partial restoration of chiral symmetry in a nuclear medium. For mesons containing light quarks (i.e. π, ω, K) many intensive studies have already been performed at experiments like Crystal Barrel/TAPS at ELSA, Crystal Ball at MAMI and HADES at GSI. With $\bar{\text{P}}$ANDA, it will be possible to extend these investigations to hadrons containing charm quarks.

Theoretical studies on charmonium production in $\bar{p}A$ reactions, presented in Ref. [67], predict that with $\bar{\text{P}}$ANDA high rates are to be expected which makes such studies feasible and worthwhile to pursue. In particular, the J/ψ nucleon dissociation cross section becomes accessible. Besides charmonium, $\bar{\text{P}}$ANDA will be able to study the properties of open-charm mesons in the nu-

clear medium. For example, it will be feasible to investigate the in-medium mass splitting of the D mesons. The detection capabilities of $\bar{\text{P}}$ANDA opens the opportunity to study the in-medium properties of a number of hadrons in the light-quark sector which can be produced at rest or at very small momenta inside the nuclei. For example the nuclear potential for $\bar{p}$, $\bar{\Lambda}$ and $\bar{K}$ is a quantity of interest, but could not be determined experimentally up to now. An overview of the perspectives of $\bar{\text{P}}$ANDA for the $\bar{p}A$ studies can be found in Ref. [54].

3.2.4 Hypernuclei

Another topic involving nuclear matter is the implantation of strange quarks into nuclei. Conventional atomic nuclei consist of protons and neutrons, which themselves consist of up and down quarks. If one or more of these light quarks of a nucleon are replaced by a strange quark, a new degree of freedom called strangeness is introduced and the baryon is called hyperon. Examples for light hyperons are the Λ hyperon (i.e. Λ=uds), the Σ hyperons (i.e. Σ^+=uus), the Ξ hyperons (i.e. Ξ^0=uss) and the Ω hyperon (i.e. Ω^+=sss) with masses between 1.1 and 1.7 GeV/c^2 [54].

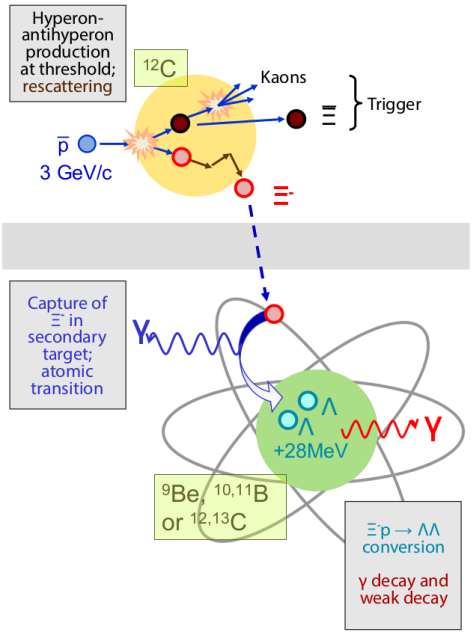

Figure 3.5: The production process of double Λ hypernuclei with an antiproton beam in $\bar{\text{P}}$ANDA. Slow Ξ from the initial reaction will be stopped in a secondary target (^{12}C) and captured in a nucleus where they will decay into two Λ_s. Figure is taken from Ref. [54].

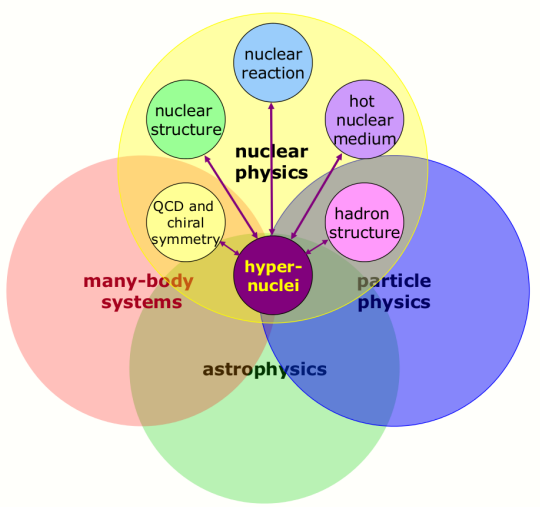

Figure 3.6: Hypernuclei and their link to other fields of physics. Figure is taken from Ref. [54].

The lifetime of these systems is typically in the order of 10^{-10} s which is long enough to become bound in the nucleus. If one or more nucleons of a nucleus are replaced by a hyperon, the resulting system consisting of the core of the remaining nucleus and the hyperon(s) is called a hypernucleus. The existence of hypernuclei is known since the 1950s [68, 69] and so far only six double-Λ hypernuclei have been detected [54]. The investigation of such systems can provide a deeper understanding of the nucleus as a many-body system and of the forces acting in it. In addition, it will enable the investigation of the behavior of strangeness in nuclear matter. With $\bar{\text{P}}$ANDA, single and double Λ hypernuclei can be investigated. The latter would be produced via an intermediate Ξ production which get decelerated in a secondary target (see Fig. 3.5). The slow Ξ can be captured in nuclei where they decay into two Λ_s. The gamma rays from the double hypernuclei can be detected. Performing high-precision gamma-ray spectroscopy allows to gain information about these double Λ hypernuclei. A hyperon bound in a nucleus offers a selective probe of the hadronic many-body problem, as it is not restricted by the Pauli principle in populating all possible nuclear states, in contrast to neutrons and protons. While it is difficult to study nucleons deeply bound in ordinary nuclei, a Λ hyperon not suffering from Pauli blocking can form deeply bound hypernuclear states which are directly accessible in experiments. In turn, the presence of a hyperon inside the nuclear medium may give rise to new nuclear structures which cannot be seen in normal nuclei consisting only of nucleons. Furthermore, a comparison of ordinary nuclei and hypernuclei may reveal new insights in key questions in nuclear physics like, for example, the origin of the nuclear spin-orbit force [70]. Therefore, a nucleus may serve as a laboratory offering unique possibility to

study basic properties of hyperons and strange exotic objects. Thus, as shown in Fig. 3.6, hypernuclear physics represents an interdisciplinary science linking many fields of particle, nuclear, astrophysics and many-body physics.

3.3 The $\bar{\text{P}}$ANDA detector

The physics program described in the previous section can only be realized with a specially optimized detector setup. $\bar{\text{P}}$ANDA is about 13 m long, it consists of a system of sub-detectors that are arranged into two parts: The Target Spectrometer (TS) and the Forward Spectrometer (FS). These two parts of the detector are shown in Fig. 3.7 and Fig. 3.8, respectively.

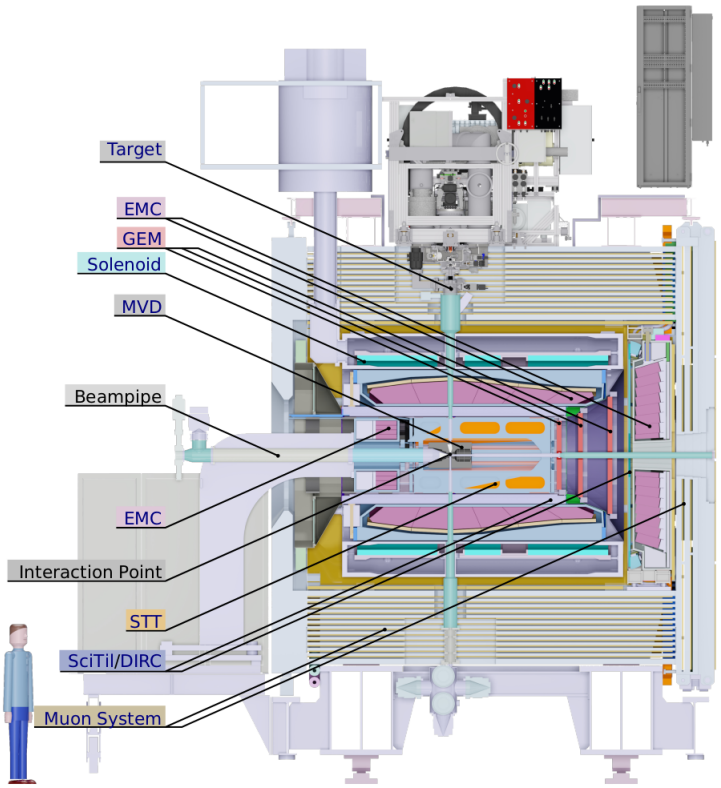

Figure 3.7: Side view of the $\bar{\text{P}}$ANDA Target Spectrometer (TS) with all sub-detectors. The antiproton beam approaches from the left. Figure is taken from Ref. [71].

The TS has a cylindrically symmetrical form surrounding the Interaction Point (IP), which is defined by crossing of the beam and the target pipe. The TS covers nearly the full 4π solid angle. The TS of $\bar{\text{P}}$ANDA has a diameter of

about 5 m. Apart from the subsystem which is responsible for the detection and identification of muons, all other detector subsystems are placed inside a superconducting solenoid magnet, which will provide a magnetic field with a strength of 2 T. Polar angles greater than 22° (with respect to the beam axis) are covered by the barrel part of the TS, polar angles smaller than 22° are covered by detectors built as endcaps.

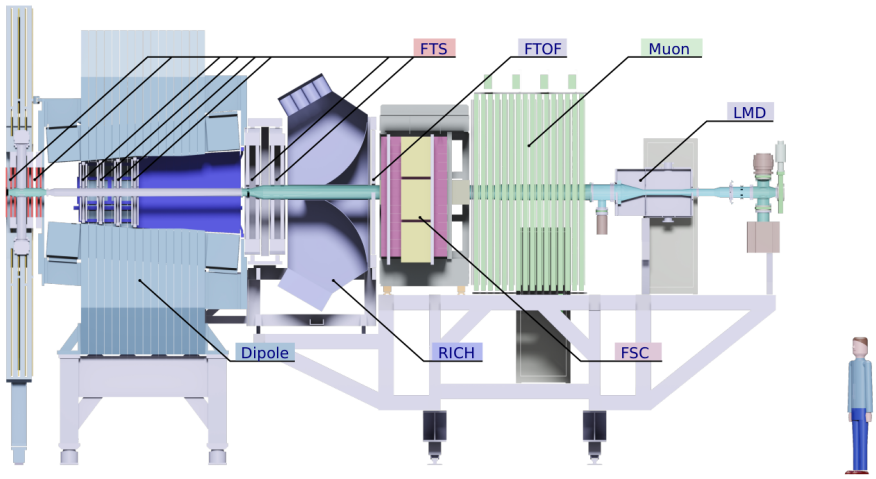

Figure 3.8: $\bar{\text{P}}$ANDA Forward Spectrometer (FS) with all sub-detectors. The antiproton beam approaches from the left. Figure is taken from Ref. [71].

The downstream part of the detector, the FS, is dedicated to the detection of particles emitted under laboratory angles below 5° and 10°, in vertical and horizontal directions, respectively. Charged particles will be analyzed with a 2 Tm dipole magnet. Neutral and fast particles will be detected in the forward calorimeters. The purpose of FS is to reconstruct high-energy, forward-boosted particles, resulting from the fixed-target kinematics of the experiment. For particle identification, three basic techniques are used: Time Of Flight (TOF), Cherenkov radiation detectors, Straw Tube Tracker (STT) with dE/dx and a large sampling muon system [54]. In the following, an overview of the most important detector sub-systems is presented, including the target and the sub-detectors categorized by their function. Fig. 3.9 shows the full $\bar{\text{P}}$ANDA setup. The $\bar{\text{P}}$ANDA hall will be available at phase one of FAIR and most of the detectors will be installed. There are several detectors that will be excluded from the start setup. In Fig. 3.9, the detectors which are indicated in black are foreseen for phase one and the red ones are foreseen for phase two. The $\bar{\text{P}}$ANDA will start working with a low luminosity at phase one. At phase two, the full setup will be ready for the installation and operation of $\bar{\text{P}}$ANDA high luminosity mode will be achieved.

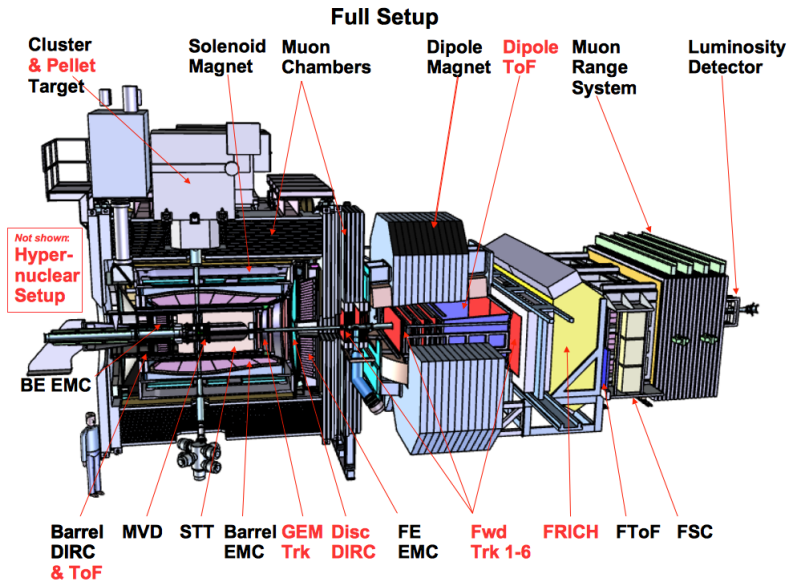

Figure 3.9: The $\bar{\text{P}}$ANDA setup. The detectors which are indicated in black are foreseen at phase one and the ones indicated in red are foreseen for phase two. The figure is taken from Ref. [97].

3.3.1 Target System

$\bar{\text{P}}$ANDA will use internal targets. The target inside a storage ring needs to be tuned in terms of size and thickness. Within the ultra-high vacuum of the storage ring, the target must be a very dilute and localized cluster of matter. Currently, two targets are being in development for $\bar{\text{P}}$ANDA, a pellet and cluster-jet target. The cluster-jet target comprises a well-known design and will be installed in the first period of $\bar{\text{P}}$ANDA experimental run (phase one). A second target, the pellet target, is being designed for runs with higher luminosities.

Cluster-jet Target

The cluster-jet target expands compressed, pre-cooled gas through a fine nozzle. During this process the gas adiabatically cools down and forms a supersonic stream of atoms or molecules which, under appropriate conditions, form a so-called cluster. The size of these clusters is strongly influenced by the experimental conditions such as the pressure or the temperature of the gas before entering the nozzle. A constant opening of the cluster-jet is provided by a skimmer and collimator in front of the vacuum. In comparison to the pellet target, this option provides a homogeneous target density and time structure

but no point-like interaction zone. The areal density of the clusters is 2 $\times 10^{15}$ atoms/cm^2, the spread of the cluster in transverse direction is 2 mm to 3 mm, its spread in the longitudinal directions is 15 mm [75]. Comparing $\bar{\text{P}}$ANDA target with targets in use in previous rings, the $\bar{\text{P}}$ANDA target will operate with higher pressures, while, for example, targets at CERN used hydrogen at pressures of 10 bar, $\bar{\text{P}}$ANDA target operates at approximately 25 bar. At the operational temperatures, hydrogen is in its liquid form, creating higher cluster densities, as needed for $\bar{\text{P}}$ANDA physics program.

Pellet Target

The second target, in development for $\bar{\text{P}}$ANDA, is a pellet target. Instead of a broad jet of target particles, the pellet target provides individual frozen droplets (pellets). The pellets are produced by injecting the desired material as a cryogenic jet into a triple-point chamber containing the same material or helium close to triple-point, the temperature and pressure conditions where gas, liquid, and solid phases coexist [9]. The triple-point chamber ensures that an extremely regular drop flow can be produced under optimal conditions without disturbances from evaporation. The drops then pass through a thin injection capillary into the vacuum. The passage cools the jet until it freezes into pellets of $\sim$20 μm diameter, which also get accelerated in the vacuum chamber due to the gas flow. This leads to an effective target areal density, compared to cluster-jet targets, a higher areal density of 5 $\times$ 10^{15} atoms/cm^2 is reached. Only with this can the high luminosities demanded by $\bar{\text{P}}$ANDA be achieved [75, 9].

3.3.2 Tracking Detectors

The task of the tracking detectors is to measure the trajectories of charged particles through the magnetic fields, leading to measurements of the particle's momenta. The high-resolution measurement of charged particle trajectories will be provided by the following sub-detectors: MVD, STT, GEM (which are located in the Target Spectrometer) and the FTS tracks particles in the Forward Spectrometer (as indicated in Fig. 3.10). In the following, $\bar{\text{P}}$ANDA tracking detectors are introduced.

Micro Vertex Detector (MVD)

In $\bar{\text{P}}$ANDA physics program, the measurement of charm and strange hadrons with a relatively long lifetime plays a key role. Thus, identifying those particles is a major task of the detector. A good vertex reconstruction can identify displaced vertices that stem from those hadrons. This is achieved by the Micro

Vertex Detector (MVD) which provides 3D hit information very close to the interaction point. The MVD is the innermost detector of the $\bar{\text{P}}$ANDA setup, directly surrounding the interaction point with a maximal radius of 15 cm and a length of 46 cm. A high resolution MVD is required in $\bar{\text{P}}$ANDA to measure the primary interaction vertex and the secondary decay vertices. Like all other detectors, the MVD has to cover nearly the complete range of polar angles (3° to 150°). Another main requirement is a high spatial resolution of less than 100 μm in the z direction and only a few tens of μm in the x-y direction, which is needed to resolve the decay vertices of D-mesons with a mean lifetime of only 123 μm for a D^0 [54]. A third requirement of the MVD setup is a low material budget to avoid an impact on the performance of the outer detectors. Especially for the EMC, it is very important to minimize photon conversions in active or passive parts of the MVD. In addition, multiple scattering of particles in the MVD will degrade the tracking performance of the complete detector. Due to these restrictions, the MVD has to consist of light and low-Z materials [76]. The setup that presently foreseen is depicted in Fig. 3.11. Since the MVD

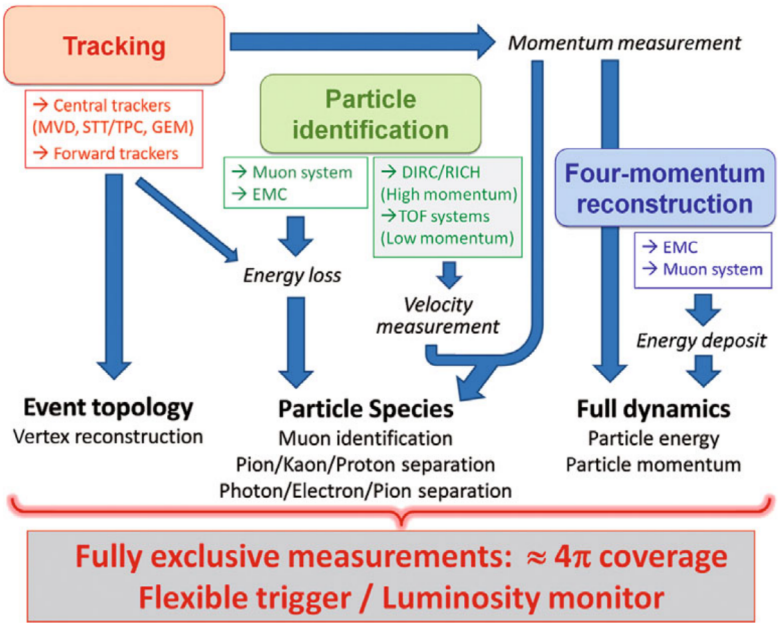

Figure 3.10: Basic data reconstruction concept of $\bar{\text{P}}$ANDA. Figure is taken from Ref. [72].

is the innermost detector, all components have to be highly radiation hard to ensure a long term operation. One silicon pixel sensor is built as a matrix of 116 × 110 cells, each square cell has a side length of 100 μm. One sensor incorporates an area of 1.3 cm^2. The pixel detectors are built as hybrid detectors: the sensor with the active silicon material, running as a reverse-bias diode, is

soldered head-to-head onto the accompanying Application-Specific-Integrated-Circuits (ASIC) read-out chip. The MVD uses three different forms of strip sensors. In the barrel part, square and rectangular shapes are employed, in the disk part, trapezoidal sensors are chosen. The latter sensors are shown; in Fig. 3.11(b). To properly measure two-dimensional hit points, all strip sensors are double-sided. The barrel sensors use a stereo angle of 90° between the two sides, the disk sensors an angle of 15°. The strip pitch, the distance between two adjacent strips, is chosen to be 130 μm in the barrel strip sensors and 90 μm in the disk strip sensors with an intermediate passive strip [9, 76].

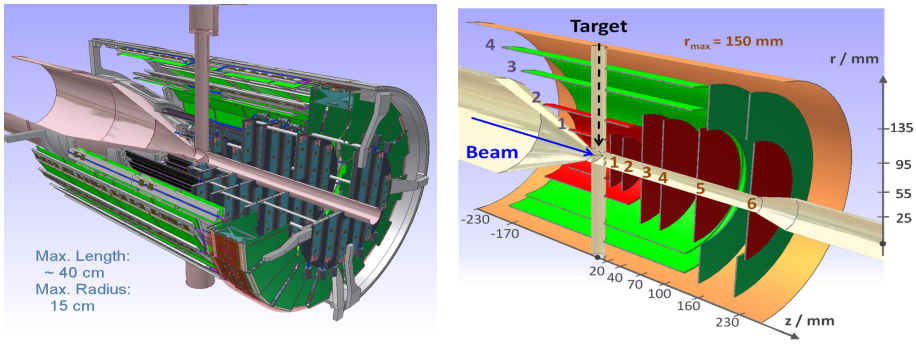

(a) **(b)**

Figure 3.11: The Micro-Vertex Detector (MVD) of the Target Spectrometer surrounding the beam and the target pipes viewed from downstream. (a) A look inside the MVD. (b) Positions of individual detectors. Red represents the pixel sensors, and green the strip sensors. Figure is taken from Ref. [72].

Straw Tube Tracker

The Straw Tube Tracker (STT) is $\bar{\text{P}}$ANDA's central tracking detector. It fills a volume of 1.26 m^3, 4224 straws enable hit point measurements with resolutions better than 150 μm in the x-y plane and a combination of tubes provides a resolution better than $\sim$ 3 mm in the z direction. The STT is illustrated in Fig. 3.12. The STT encloses the MVD (the inner tracking). It is followed in beam direction by a vertical setup of GEM disks for adding track points in the forward polar-angle range, as discussed in the next section. The STT covers a polar angle range from about 10° to 140°. The main task of the STT is the precise spatial reconstruction of the helical trajectories of charged particles in a broad momentum range from about a few 100 MeV/c up to 8 GeV/c. The particle momentum can be extracted from the reconstructed trajectory in the solenoidal magnetic field. Another important task for the STT is the measurement of the specific energy loss (dE/dx) for particle identification. The PID

information of the STT is needed in particular to separate protons, kaons and pions in the momentum region below 1 GeV/c [76].

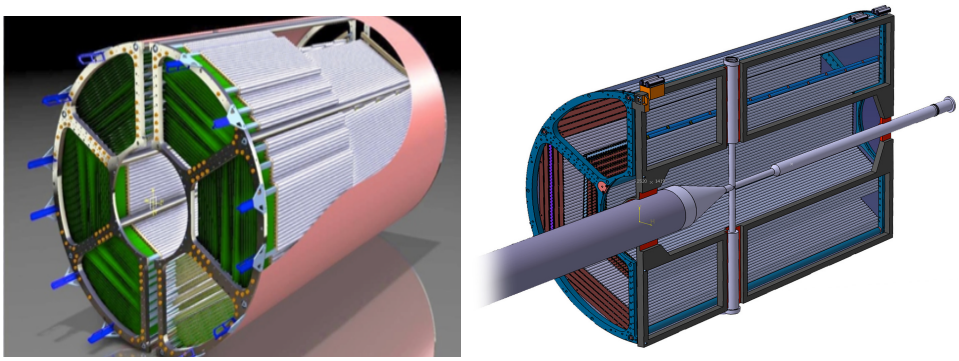

(a) **(b)**

Figure 3.12: (a) CAD drawing of the STT, including the low-weight holding structure. (b) Half view of STT. The intersection between the target pipe and beam pipe can be seen, the MVD, which surrounds the interaction point, is not shown. Figure is taken from Ref. [76].

The straw tubes that will be used for the $\bar{\text{P}}$ANDA detector have an active length of 140 cm. Each straw is a small drift tube with an inner diameter of 10 mm and a wall thickness of 27 μm. They are made of two layers of 12 μm aluminized mylar films by wrapping two long film strips around a rotating mandrel. The first layer of aluminization is used for electrical conduction and the second for shielding against external light [77]. A gold-plated tungsten-rhenium wire with 20 μm diameter is used as anode. The tubes are sealed at both ends. Cylindrical precision end plugs are made of ABS (Acrylonitrile-Butadiene-Styrene) thermoplastic with a wall thickness of 0.5 mm. They are glued to the mylar film leaving a small 1.5 mm film-overlap on both ends (see Fig. 3.13). A gold-plated copper-beryllium spring wire is inserted in order to provide the electric ground. The springs allow a 2 mm tube elongation with a typical spring force equivalent to 10 g. The end plugs have a central hole with a 3 mm thick cylindrical nose to insert and glue a crimp pin for the wire. A micro PVC (medical quality grade) tube is fed through another hole and glued in the end plugs to provide a gas flow through the tube. A light-weight, self-supporting structure is chosen for STT, because an external frame, will add to the tension and also increase the detector's material budget. The structure consists of two identical flanges, shaped and drilled individually, connected by

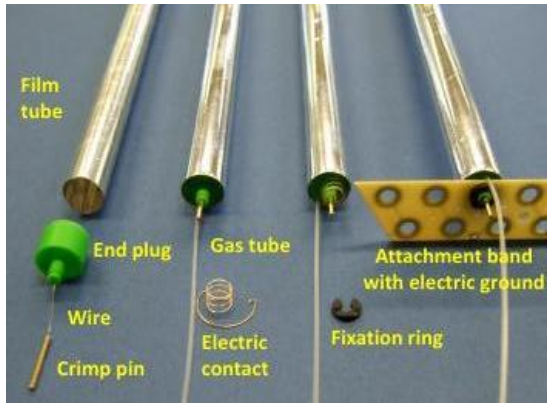

Figure 3.13: A photograph of all straw components and the straw assembly steps. Figure is taken from Ref. [76].

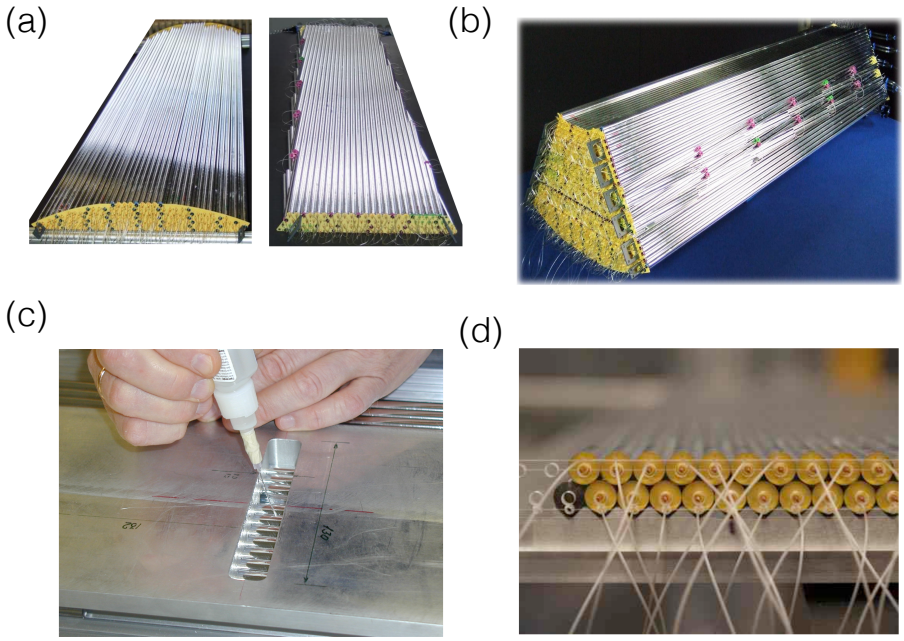

Figure 3.14: (a) Photograph of an axial straw layer module for the outer cylindrical shape and module with two double-layers with opposite skew angle. (b) Photograph of all straw modules of one STT hexagon sector. Two thermoplastic mounting brackets at both ends of a module are used for its support and positioning in the mechanical frame. (c) Gluing of straw tubes to multi-layers. (d) A straw tube double-layer on the reference plate. Figures taken from Ref. [76].

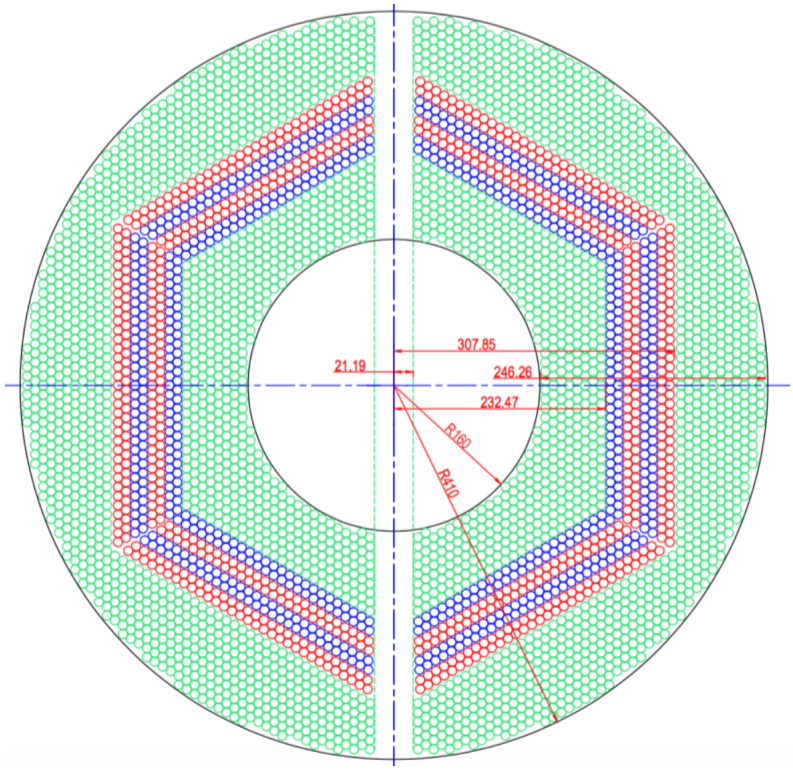

(a)

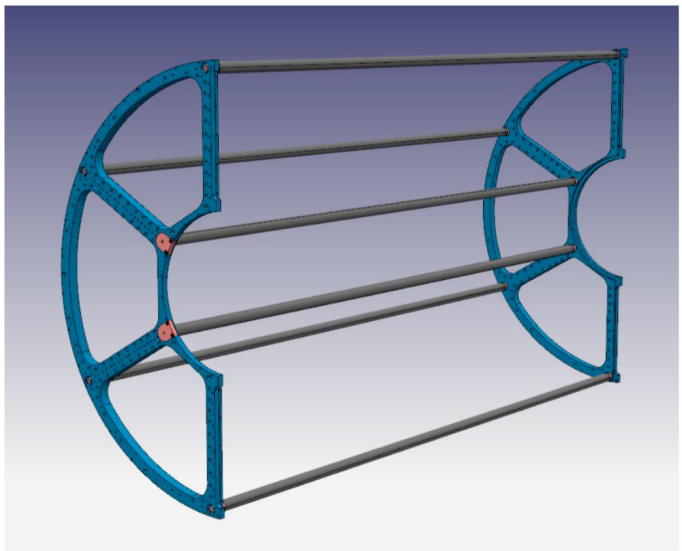

(b)

Figure 3.15: (a) Layout of the straw tubes in the STT in xy-view. The straws marked in green are parallel to the beam axis. The blue and red marked straw layers are skewed relative to the axially aligned straws in the same sector by angles of $+2.9°$ and $-2.9°$, respectively. (b) Pictorial drawing of one of the two frame structures of the STT. Figures are taken from Ref. [76].

screws to six precise tubular spacers (see Fig. 3.15(b)). The layers of a sector are grouped into multi-layer modules, consisting of four close-packed axial layers or two close-packed double-layers with opposite skew angle. The outermost module in a sector consists of seven close-packed axial layers with a varying number of straws per layer to reach an outer cylindrical shape (see Fig. 3.14(a)) [76]. For the innermost straw module, a few single straws are added in the corners to reach the inner cylindrical shape. Each of the two semi-cylindrical $\bar{\text{P}}$ANDA-STT volumes is filled by three sectors of straw tubes aligned in the z-direction and arranged in stacks of planar multilayer modules [76]. The straws are organized in 19 layers parallel to z (axial straws) and 8 layers skewed by a small angle of $+2.9°$ and $-2.9°$ with respect to the z-axis (skewed straws). The skewed straws are located skewed straws are located in a hexagonal array placed at an intermediate radius of the STT (see Fig. 3.15(a)) and enable measurements in the z-direction with a resolution of $\sim$3 mm. The straws are closely packed with a minimal space of 20 μm between each straw (see Fig. 3.15(a))[76].

The straw tubes are held at 1 bar over pressure, giving mechanical tension to the anode. A suitable gas mixture for the operation of straw tube detectors should satisfy different physics requirements and environmental concerns. The operating gas mixture should provide good spatial resolution, high-rate capability, long radiation length X_0 and low ageing. Ageing occurs due to the plasma-chemical processes in the detector during the gas amplification which deposit impurities on the electrodes. Ageing causes a gradual gas gain reduction, signal loss and finally detector breakdown. In the aging test of straw tubes at COSY for $(Ar/CO_2)(90 : 10)$ mixture, minimal ageing has been observed up to the accumulated charge of 0.72 C/cm [72, 73, 74]. The gas mixture (Ar + CO_2) has excellent drift properties by providing low longitudinal diffusion and small ageing effects.

Gas Electron Multiplier (GEM)

Particles emitted at the polar angles below 22°, which are not covered fully by STT will be tracked by three planar stations placed at approximately at 1.1 m, 1.4 m, and 1.9 m downstream from the target in the TS. Each station consists of double planes with two projections per plane. The chambers have to sustain a high counting rate of particles peaked at the most forward angles due to the relativistic boost of the reaction products as well as due to the peaking cross section at small angles of the $p\bar{p}$ elastic scattering. The maximum expected particle flux in the first chamber in the vicinity of the 5 cm radius opening for the beam pipe will be about 3×10^4 cm^2 s^{-1} [9, 54]. The stations will be equipped with gaseous-pattern detectors based on GEM foils as amplification

stages (see Fig 3.16(a)). A system of three stacked GEM foils amplifies electrons to measurable quantities. A foil is typically made from a plastic material and coated with a conducting surface. The GEM disc stations are drift volumes that contain thin Kapton foils with copper-coated sides. By applying a high voltage between the two sides, strong electric fields form a dense package of field lines in the holes which cause avalanche multiplication of the drifting electrons. Fig. 3.16(b) shows the hole pattern, the holes of 70 μm diameter, aligned with a pitch of 140 μm in the foils. The GEM detector measures hit points with a resolution better than 100 μm [9].

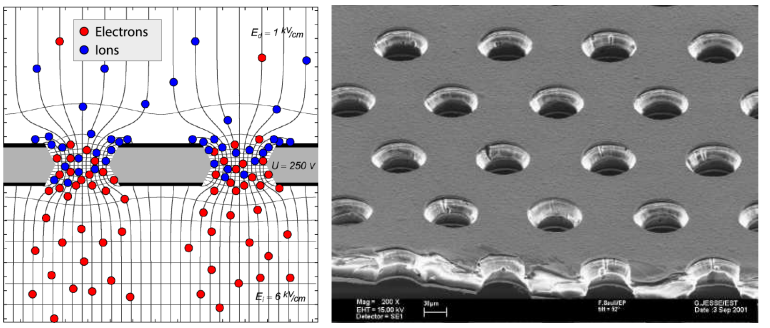

(a) **(b)**

Figure 3.16: (a) The working principle of the GEM: electron amplification occurs through small holes by applying a high voltage. (b) Electron microscope picture of the GEM hole pattern. Figures are taken from Refs. [9, 78, 79].

Forward Tracking System (FTS)

The Forward Tracking System (FTS) is designed to measure those particles with shallow polar angles of less than 5° in vertical and 10° in horizontal direction [80]. The FTS is dedicated to measuring tracks of particles boosted in the forward direction. In particular, the amount of deflection of a particle's trajectory due to the FS dipole is analyzed. The FTS consists of three pairs of planar tracking stations. The first two stations, dubbed FT1 and FT2, are located in front of the dipole and directly after the Target Spectrometer, the last two, FT5 and FT6, are located after the dipole and in front of the RICH detector. FT3 and FT4 are located inside the dipole magnet gap (see Fig. 3.8). This will allow to track particles with highest momenta as well as very low momentum particles where tracks will curl up inside the magnetic field. Each tracking station is equipped with four double layers of straw tubes. The first and the fourth one contain vertical straws (0°) and the two intermediate double-ayers, the second and the third one, contain straws inclined at +5° and -5°, respectively. FT1 and FT2 have 1024 straws, FT3 and FT4 have 1536

straws; FT5 has 3200 straws, and FT6 has 4736 straws. In total, over 13,000 straws instrument the FTS. The planned configuration of double-layers allows to reconstruct tracks in each pair of tracking detectors separately, especially in case of multi-track events. Due to the different magnetic field configuration, the maximum drift times are a bit lower than in the STT with values from 130 ns to 150 ns, depending on the dipole's field strength. The maximum drift times in the straws operated outside the dipole are 130 ns. Positions can be resolved with $\mathcal{O}(100\ \mu\text{m})$, leading to momentum resolutions expected better than 1% [9].

3.3.3 Particle Identification Detectors

Charged particle identification of hadrons and leptons over a large range of angles and momenta is an essential requirement to meet the physics objectives of $\bar{\text{P}}$ANDA. The $\bar{\text{P}}$ANDA detector is equipped with various particle identification systems providing the ability of classifying particle species over the whole kinematic range in addition to the energy-loss measurements from the tracking detectors and the EMC. The main part of the momentum spectrum above 1 GeV/c will be covered by Cherenkov detectors. Below the Cherenkov threshold of kaons several other processes will be employed for particle identification. Besides the contribution of energy-loss measurement from the tracking detectors, the time-of-flight barrel and forward wall can identify slow particles.

Detection of Internally Reflected Cherenkov light (DIRC)

Detectors employing Detection of Internally Reflected Cherenkov light (DIRC), detect Cherenkov light created in confined spaces. Charged particles in a medium with index of refraction n, propagating with $\beta c > 1/n$, emit radiation at the angle $\Theta_c = \arccos(1/\beta n)$. The light is transferred to photon detectors by means of total internal reflection, preserving the opening angle of the light cone, and thus information on the velocity of the creating particle. The combination of DIRC information of a particle's velocity with momentum information measured in the tracking detectors yields the particles mass, fully identifying the kind of particle [81]. Two DIRC sub-systems are going to be used, a barrel DIRC and a disc DIRC in the forward direction, see Fig. 3.17(a) and Fig. 3.17(b), respectively. The radiator bars of the barrel DIRC are located between the SciTil on the outside and the STT on the inside. It uses silica bars as Cherenkov radiators to provide a pion-kaon (and proton) separation for particle momenta up to $\sim$3.5 GeV/c at polar angles between 22°-140° and an azimuthal range of nearly 2π, leaving only a gap for the target pipe. The bars have the dimensions of 2400 mm $\times$ 17mm $\times$ 32 mm [9]. The scintillators are connected to filter optics and expansion volumes, guiding the light to

the photon sensors; see Fig. 3.17(a). The Barrel DIRC design is based on the BaBar DIRC [84] with several improvements, such as focusing optics and fast photon timing. To keep the material budget inside of the calorimeter as low as possible, the barrel DIRC is read out in the upstream direction. Mirrors are attached to the bar in the downstream direction to reflect the photons towards the readout at the opposite end, where they are coupled out and focused via lenses into an expansion volume. This volume (with a depth of 30 cm) is filled with mineral oil [82].

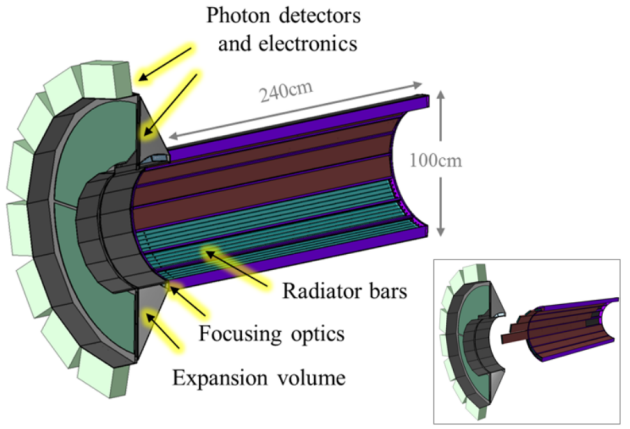

(a)

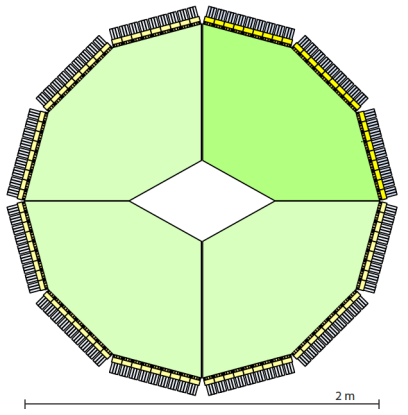

(b)

Figure 3.17: The DIRC detectors of $\bar{\text{P}}$ANDA. (a) The barrel DIRC system. The radiator bars (turquoise) are arranged in sets of five to form bar boxes (red). The expansion volume in the backward direction is colored in a dark shade of green, with the photon detection in lighter green. Figure is taken from Refs. [9, 82]. (b) The disc DIRC. The radiator is colored in green and segmented into four pieces. They are read out through the surrounding instrumented focal plane. One quarter section is highlighted. Figure is taken from Refs. [9, 82].

Micro-channel plate photo-multiplier tubes (MCP-PMTs) are used to convert the light into an electrical signal with a sum of around 15,000 channels. For the PID process two spatial coordinates and the time of the detected photon are measured. With these 3D-patterns, PID likelihoods for different particle hypothesise are calculated. The arrival time is measured with a precision of about 100 ps and the angular resolution is 8 mrad to 10 mrad. With the envisaged setup, pions and kaons can be separated with $> 3\sigma$ confidence level for a momentum range up to 4 GeV/c [85]. Another DIRC sub-system is disk-shape. This disc DIRC is placed in the forward endcap of the target spectrometer. The same measurement principle but with a disc-shaped configuration is used by the disc DIRC. Pions and kaons with momenta up to 4 GeV/c and with polar track angles below the acceptance of the barrel DIRC down to 10° in horizontal and 5° in vertical direction are identified here. Like the barrel part, the disc is made from fused silica. The disc has a diameter of 2200 mm and a thickness of 15 mm. Shaped like a regular dodecagon, the disc DIRC has four identical but optically separated sub-detectors. On each straight surface on the outside, a focusing light guide is glued to the silica, with a diachronic filter in the transmission region. Their focusing optics and light readout is placed on the outside [86]; see Fig. 3.17(b).

Ring Imaging Cherenkov Detector (RICH)

In the Forward Spectrometer, for separating the π/K and K/p at very high momenta, a Ring Imaging Cherenkov (RICH) detector will be installed. It will be located at approximately 6.5 m downstream of the interaction point with a coverage of angles $< 10°$ and $< 5°$ in horizontal and vertical directions, respectively. The favored design is a dual radiator RICH detector, using silica aerogel and freon (C_4F_{10}) gas. RICH provides π /K/p seperation, in a broad momentum range from 2 GeV/c to 15 GeV/c [87].

Time-Of-Flight System (TOF)

Very slow particles cannot be identified with the help of the DIRC system because they do not emit Cherenkov light in the radiators, so, another PID detector is placed directly adjacent to the barrel DIRC. A Time-Of-Flight system will be placed between the Barrel DIRC and the EMC and it will be used for the identification of slow charged particles at polar angles from 22° to 140°. This detector measures the time-of-flight of incident particles with a resolution of roughly 100 ps. The detector is based on scintillator tiles and it will be read out by two Silicon Photomultiplier (SiPMs) per tile. The tiles are made of a plastic scintillator, BC-408, and have a 28.5 mm × 28.5 mm surface area and 5 mm thickness. The material is chosen to have a good light yield and timing resolution: A minimum ionizing particle losing ∼1 MeV in the ∼5 mm thick-

ness of a tile, creates 10,000 photons, of which 120 photons can be measured. The timing achieved with this is $\mathcal{O}$(100 ps). The full system consists of 5760 tiles in the barrel part and can be augmented by approximately 1000 tiles in the forward direction, just in front of the endcap disc DIRC. Another TOF-detector is foreseen in the Forward Spectrometer, the Forward Time-Of-Flight (FTOF). It is a wall of slabs (140 cm height and 2.5 cm thickness), made of a plastic scintillator and read out on both ends by fast photo-tubes and it serves as a time-of-flight counter placed at about 7 m from the target. Like the SciTil (Scintillator Tile), it detects particles by fast-responding scintillators. The width of the scintillators depends on their proximity to the beam axis, with 10 cm for the far and 5 cm for the near modules. Similar detectors are also placed inside the dipole magnet in order to detect low momentum particles which do not exit the dipole magnet. The time resolution is expected to be in the order of 50 ps thus allowing a good π/K and K/p separation up to momenta of 2.8 GeV/c and 4.7 GeV/c, respectively [9, 88, 89].

Muon System

The main task of the muon system is the muon identification via pattern recognition and matching of the track segments to the tracks inside the magnet. Muons are identified at the outermost part of the detector as they pass the inner systems. The Range System (RS) technique was chosen in $\bar{\text{P}}$ANDA for muon registration in a laminated iron absorber. The RS structure is a well-known solution for the registration of muons when they are stopped by the absorber and when they cross the whole iron [90, 9]. The stopping power, dE/dx of iron is about 1.5 GeV per meter. The muon system is built as a range system, with detecting layers alternating with passive iron layers. The active sensors are Mini Drift Tubes (MDTs), operated in the proportional mode. Fig. 3.18 shows the layout of the muon system with the number of MDT detectors indicated for each particular subsystem. The muon system will be instrumented with 3751 MDTs. The $\bar{\text{P}}$ANDA system for muon detection is divided into four parts: three in the Target Spectrometer and one in the Forward Spectrometer, see Fig. 3.18. The barrel muon system surrounds the solenoid magnet cylindrically and functions as its return yoke. In the barrel, there are 13 sensitive layers, each 3 cm thick. To adjust to the higher momentum of forward boosted particles, the iron layers of the endcap are 6 cm thick. Downstream of the endcap, additional 4 alternating layers follow in the so called muon filter. Besides extending the endcap's muon detection it also enhances the magnetic shielding between the two magnetic fields. The forward muon system consists of 16 iron layers of 6 cm thickness alternating with detection layers. Downstream of the endcap, additional 4 alternating layers follow in the so-called muon filter [9, 90].

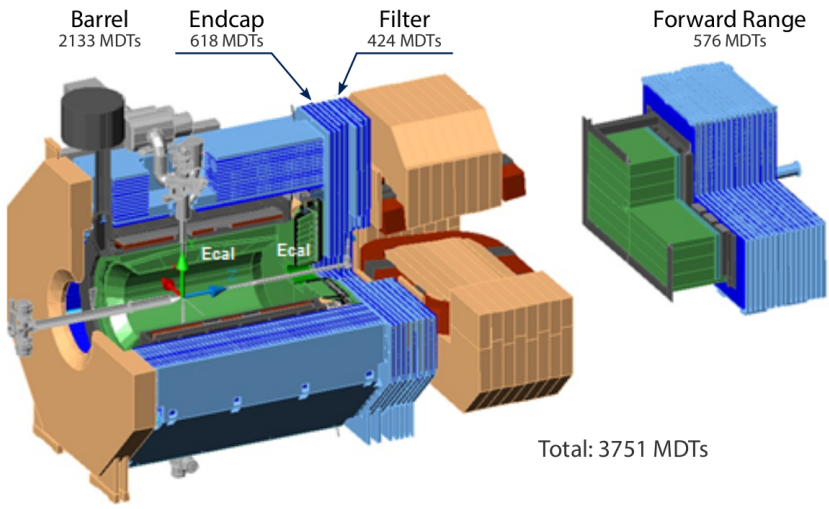

Figure 3.18: Overview of the muon system of $\bar{\text{P}}$ANDA. The four parts of the muon system, are colored in blue. The number of Mini Drift Tubes (MDT) is indicated for each subsystem. Figure is taken from Ref. [90].

3.3.4 Electromagnetic Calorimeters (EMC)

The main purpose of an electromagnetic calorimeter (EMC) is to precisely measure the energy of photons, electrons and positrons. In addition, an EMC can also measure the scattering angles of photons which are not accessible by the tracking detectors. To achieve this, the particle is stopped in a medium of high density, while at the same time a measurable signal is generated that allows to quantify the amount of energy that was deposited in the absorber medium. The EMC is equipped with about 15500 scintillating lead-tungstate ($PbWO_4$) crystals. These crystals are high density inorganic scintillators with sufficient energy and time resolution between 50 and 100 ps for photon, electron and hadron detection even at intermediate energies [91]. The Target Spectrometer EMC contains three parts: a backward endcap, a barrel part and forward endcap. Fig. 3.19(a) shows the barrel part and the forward endcap. The barrel calorimeter is located in the central region, inside of the solenoid and outside of the SciTil. It covers a length of 2.5 m, starting at an inner radial distance of 0.57 m and ends at 0.94 m. The polar range of 22° to 140° is covered, see Fig. 3.19(c). Each crystal has a length of 200 mm, equivalent to 22 time radiation length X_0 of $PbWO_4$ and a front surface area of approximately 20 mm $\times$ 20 mm. The exact dimension depends on the location of each crystal in the calorimeter.

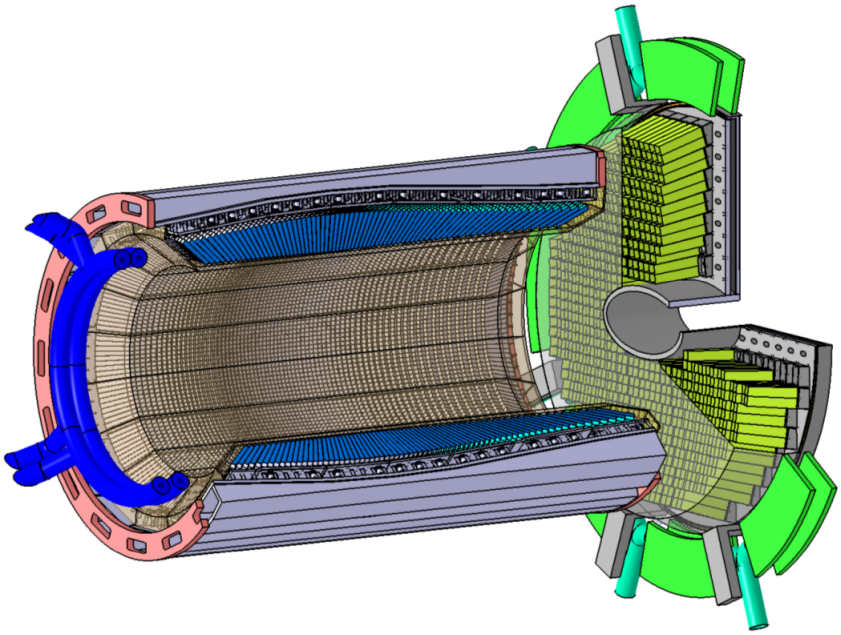

(a)

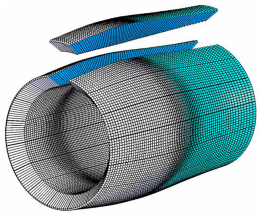

(b)

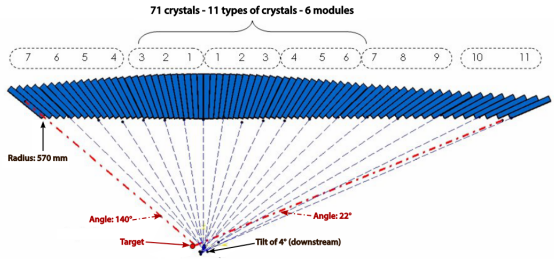

(c)

Figure 3.19: (a) The design of the EMC in the Target Spectrometer with crystals of the barrel part (blue) and forward endcap (green). (b) Distribution of crystals of the barrel calorimeter. The calorimeter is built with rotational symmetry around the beam axis; an exemplary slice in z direction is exposed from the system of crystals. (c) In total, seven different types of crystals are used for the barrel calorimeter. They are inclined towards the interaction point, with a slight skew to the downstream direction. Figures are taken from Ref. [91].

With an inner radius of 57 cm the barrel part of the calorimeter requires 11360 crystals. Fig. 3.19(b) shows the crystal arrangement of the EMC. The crystals are grouped into a pack of 4 $\times$ 10 leading to 16 sectors of 22.5° coverage in azimuthal angle each. The crystals are held by a carbon fiber holding structure and wrapped into highly reflective foil. The distance between two crystals is 600 μm. They are installed pointing to the direction of the target, with a slight offset of a few degrees to reduce the dead zone between the crystals for par-

ticles originating from the interaction point. Depending on the exact shape, each crystal weighs on average 0.98 kg. The forward endcap will have 3600 crystals and the backward endcap 592 crystals. The forward endcap closes the barrel in the downstream direction, the backward endcap upstream. The forward endcap is located 2.1 m downstream from the interaction point and has a diameter of 2 m, covering angles of 5° to 23.6° (vertically) and 10° to 23.6° (horizontally). The backward endcap is located at 1 m upstream from the interaction point, and has a diameter of 0.8 m. It covers polar angles from 151.4° to 169.7° [91]. The calorimeter has a low photon energy threshold of ∼10 MeV, with single crystals at 3 MeV. An energy resolution of $\sigma_E/E \leq 1\%$ is achievable. The spatial resolution, given in terms of the polar angle, is expected to be $\leq 0.5°$, $\leq 0.3°$, and $\leq 0.1°$, for the backward endcap, barrel, and the forward endcap, respectively. Moreover, it is worth mentioning that the $\bar{\text{P}}$ANDA EMC will be cooled to -25°C in order to get double the light output [93].

The Forward Shashlyk-type Calorimeter (FSC) is designed to cover the forward acceptance with high resolution. The detection is based on lead scintillator sandwiches read out with wave-length shifting fibers passing through the block and coupled to photo-multipliers. It is located in the Forward Spectrometer, after the last TOF wall and before the forward muon system starting 7.8 m downstream from the interaction point and spanning to 8.95 m. In total, the FSC has a mass of 3.7 t. Similar to the EMC, it has a low-energy threshold for photons of 10 MeV to 20 MeV and an energy resolution of $\sigma_E/E \leq 1\% \oplus$ (2-3)%/$\sqrt{E/\text{GeV}}$ [93].

3.3.5 Luminosity Detector

The exact measurement of the time integrated luminosity L for a time interval dt is an essential parameter for the determination of the cross section (σ) of a decay channel. According to $N = L \times \sigma$, it provides a direct correlation between the number of events N measured in an time interval dt and the cross section. The intention is an accurate determination of the absolute and relative integrated luminosity with precisions of 5% and 1%, respectively. The Luminosity Detector (LMD), the most downstream detector system of $\bar{\text{P}}$ANDA, is shown in Fig. 3.20(a). The cone walls are about 10 μm thin and keep the LMD's volume in vacuum. This detector will be placed behind the forward muon system, approximately 11 m away from the interaction point. It will be positioned directly around the beam pipe, covering the full azimuthal angle. For the detection of traversing particles, thin, silicon-based pixel sensors with integrated front-end electronics, High Voltage Monolythic Active Pixel Sensors

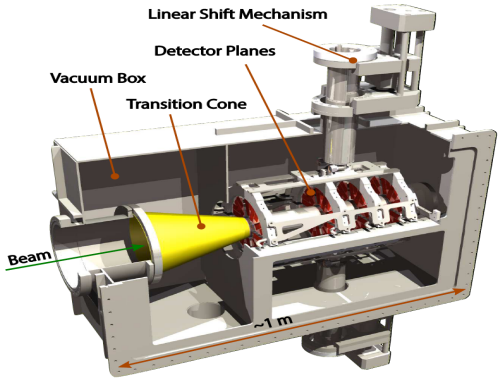

Figure 3.20: A CAD drawing of the LMD system. Figure is taken from [93].

(HV-MAPS), are used. The HV-MAPS are produced as 2 cm × 2 cm squares with 50 μm thickness and grouped into 10, partially, overlapping pieces to form a module [9, 93].

3.3.6 Magnets

The reconstruction of charged particles in $\bar{\text{P}}$ANDA is based on the curvature of their trajectories in a magnetic field. This bending is achieved by two magnet systems. A superconducting solenoid with magnetic field of 2 T will be located in Target Spectrometer and in the Forward Spectrometer. A dipole magnet with a field up to 1 T will be used for the Forward Spectrometer.

Solenoid magnet

In the Target Spectrometer region, a superconducting magnet creates a solenoid field with a strength of 2 T, with a homogeneity of better than 2% along the beam axis. The magnetic field is supplied over a length of 4 m in the central opening hole of the magnet of 1.9 m diameter. The NbTi coils of the magnet are placed outside the electromagnetic calorimeter in order to avoid dead material in front of it; see Fig. 3.21(b). Fig. 3.21(a) shows all sub-detectors of the Target Spectrometer that are housed inside the solenoid, excluding the muon chambers.

Dipole magnet

$\bar{\text{P}}$ANDA is a fixed target experiment and many particles will go forward due to momentum conservation. Therefore, good reconstruction capabilities of forward-boosted charged particles are essential. The magnetic field for the

charged-particle tracking in the forward direction is provided by a dipole magnet with a maximum bending power of 2 Tm. Fig. 3.22 visualizes the dipole magnet. The dipole has a one-meter gap and an aperture of 1 m × 3 m. The magnetic field of the dipole is shielded against the field of the solenoid by a field clamp. The magnet is ramped together with HESR, as its field influences also circulating particles in the beam. In the current planning, the magnet yoke will be 2.5 m long in beam direction starting at 3.0 m downstream of the target, and the overall height and width are 3.9 m and 5.3 m, respectively. The return yoke is made of steel and built in segments. This gives beneficial properties for ramping the magnet together with HESR and also simplifies assembly in the experimental hall. In total, the dipole weighs about 220 t [9, 94].

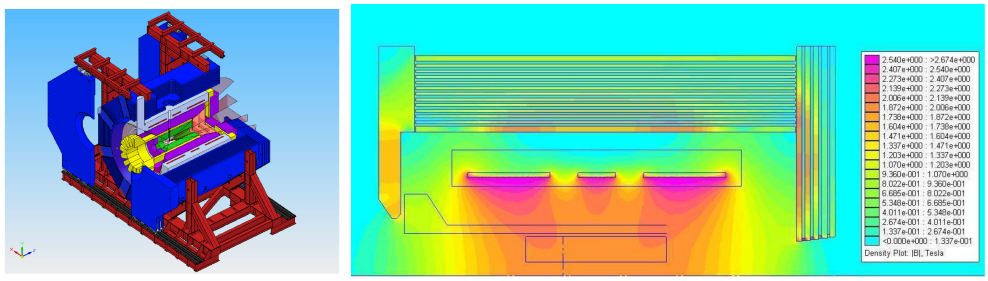

(a) **(b)**

Figure 3.21: Illustrations for the solenoid magnet: (a) CAD drawing. The return yoke is colored in blue, the sub-coils in red, surrounded by the accompanying coil system (cryostat, coil former) in light blue. (b) A simulation of the magnetic flux density of the solenoid magnet. The antiproton beam enters from the bottom left corner of the image. Figures taken from Refs. [9, 94].

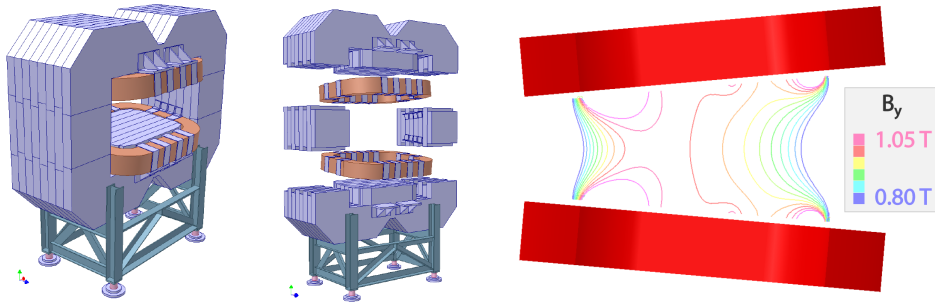

(a) **(b)** **(c)**

Figure 3.22: Visualizations of the dipole magnet: (a) CAD drawing of the closed magnet, looking from the downstream direction. (b) CAD drawing of an exploded view. (c) Strength of the y component of the magnetic field in the z - y plane. Figures are taken from Refs. [9, 94].

3.4 Data Acquisition

$\bar{\text{P}}$ANDA will run with a quite diverse physics program. The different physics channels investigated have different signatures, which are not easy to distinguish from the huge background. Additionally, sufficient statistics is needed in order to perform high-precision measurements. This requires a high interaction rate. So, employing a novel scheme for acquisition and processing of detector is needed. The Data Acquisition (DAQ) system of $\bar{\text{P}}$ANDA has to deal with high data rates of up to 200 GB/s at an average interaction rate of 20 MHz [54].

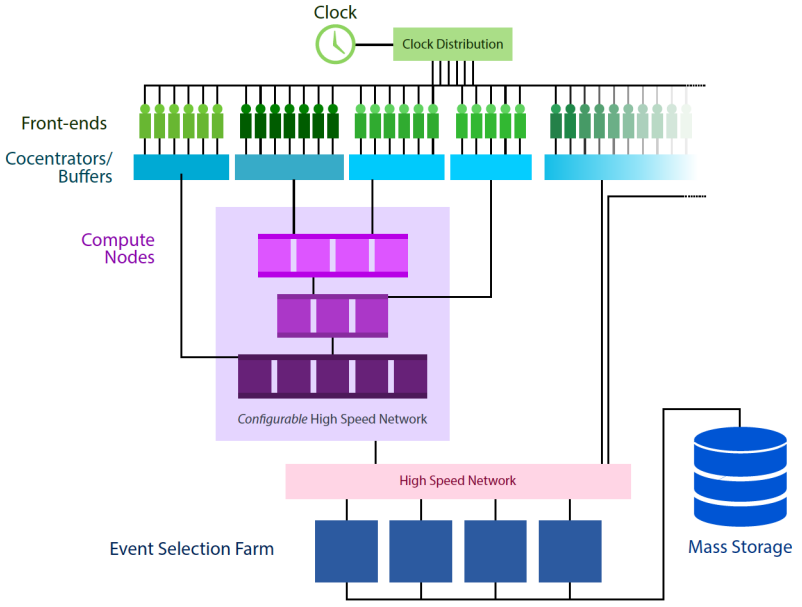

Figure 3.23: $\bar{\text{P}}$ANDA DAQ scheme, divided into the different devices responsible for data processing. Figure is taken from Ref. [95].

To reduce the amount of data being written to disk, the data have to be filtered for interesting events which are defined by the physics goals. At the same time, the DAQ has to allow for a very flexible trigger generation since signal and background events will be very similar in terms of track multiplicity, kinematic distribution, and event shape. Because of this, $\bar{\text{P}}$ANDA does not use a global hardware trigger. Instead every detector front end employs feature extraction algorithms to select relevant data from its free running front-end electronics. The pre-processed data of several front-ends are collected in data concentrators and sent to an event-building network which consists of two stages. Compute nodes reconstruct the event on the fly in order to form a trigger decision. In-

teresting events are then written to disk. Fig. 3.23 illustrates the DAQ scheme of P̄ANDA. Field Programmable Gate Array (FPGA) boards are mainly used to compute the nodes. To synchronize the DAQ system between the different sub-detectors the Synchronization of Data Acquisition (SODA) protocol will be used. The system is an optical network which provides a common reference time better than 20 ps RMS (Root Mean Square) to fulfill this task. It is also able to synchronize the events which come from different sub-detectors as some readout systems are slower than the anticipated event rate of 20 MHz in the HL mode. These global time-stamps are used to sort and combine sub-events from the individual detectors [54, 95].

3.5 P̄ANDA Analysis Software Framework

A powerful software toolkit is available during the preperations of P̄ANDA. This software framework is still under development and presently used to simulate the response of physics reactions, thereby, to evaluate P̄ANDA physics potential. It contains three major components of code: external packages, FairRoot and PandaRoot. The code design [95] is shown in Fig. 3.24. This section presents the most important features and components of the framework and the analysis tools which are used during the course of a typical simulation data run in this thesis; see chapter 4.

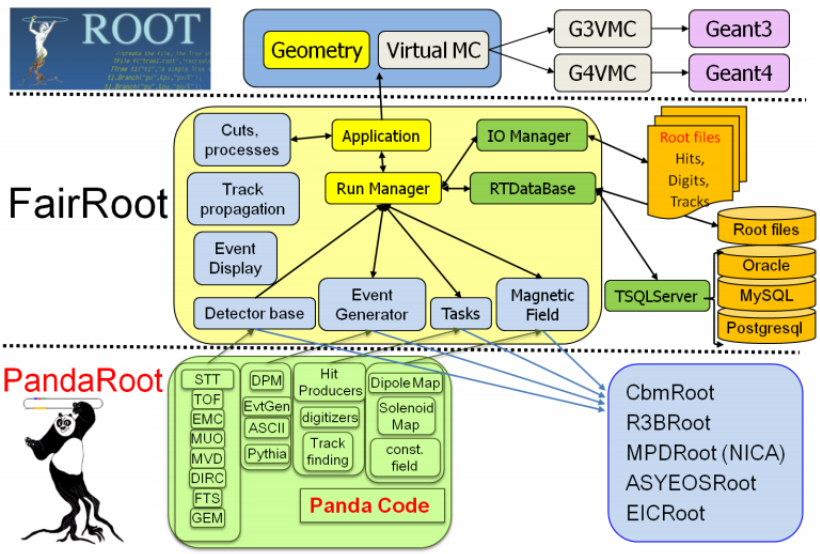

Figure 3.24: Code design of the P̄ANDA analysis framework. Figure is taken from Ref. [96].

3.5.1 FairRoot and External Packages

The first and major layer of the software toolkit is referred to as external packages. External packages are collection of software, specified as a part of FairSoft, for the experiments at the future FAIR facility. They commonly use packages such as GEANT3 and GEANT4 (for propagation of particles through matter written in Fortran [102] and C++ [103]), VMC (Virtual Monte Carlo [104]), ROOT [105], Pythia [106] and auxiliary tools. On the lowest level, PandaRoot builds upon ROOT [99, 100] package, CERN's data analysis framework. ROOT was first presented in 1997 [101] and is now commonly used in high energy physics community. ROOT provides a large set of functionalities; it offers infrastructure for processing, displaying, and storing physics related data. It is written in C/C++ and offers the ability to run programs (macros) in an interpreted, uncompiled mode, enabling swift implementations of data analysis. To extend ROOT for the needs of the FAIR experiments, the next framework layer, FairRoot is developed [107]. It extends ROOT by computing tasks common for particle physics experiments and was originally developed for FAIR experiments CBM, $\bar{\text{P}}$ANDA and R3B. As shown in Fig. 3.24, it provides a task-based structure by handling the input and output files, interfaces and infrastructure. The task is to provide all steps of the data processing up to the physics analysis stage. Data are stored in ROOT files, which contain ROOT objects such as chains, trees, and branches. The framework delivers base classes for detector handling, magnetic field definition and event generators for simulation. Additionally, it provides buffer and tasks needed for the time-based simulation [96].

3.5.2 PandaRoot

PandaRoot is the offline analysis and simulation framework of $\bar{\text{P}}$ANDA. It introduces the individual detector descriptions and algorithms specifically optimized for the properties of $\bar{\text{P}}$ANDA data output [108]. PandaRoot is programmed in C/C++. PandaRoot is intended to be used for simulated data as well as experimentally obtained data, when $\bar{\text{P}}$ANDA starts its experimental running program. The complete detector geometry, including all sub-detectors geometries, HESR beam pipe, target and maps of magnetic fields, as presented in section 3.3, is reconstructed digitally using the appropriate materials and dimensions. The $\bar{\text{P}}$ANDA specific digitization and reconstruction algorithms are also incorporated into the framework. Fig. 3.25 illustrates the work-flow within the framework of PandaRoot both simulated and experimental data. The following will focus on the work-flow regarding simulated data.

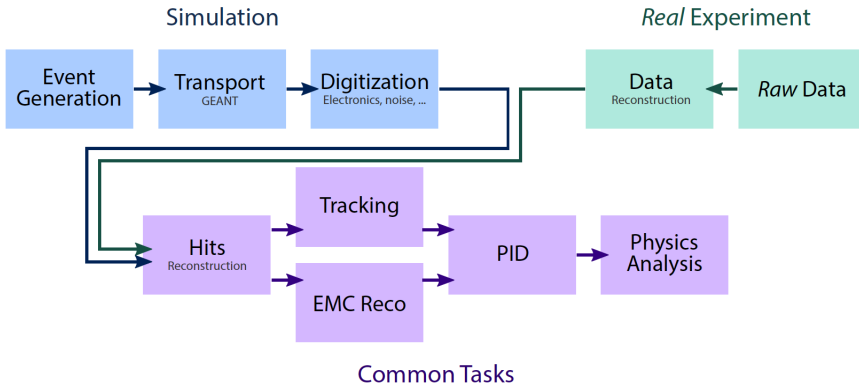

Figure 3.25: Workflow of the data analysis in PandaRoot. The framework can be used for both simulated and actual experimental data. Figure is taken from Ref. [98].

Event Generation

The first step of the simulation is the event generation. Within PandaRoot, a set of generators are available such as EvtGen, DPM, FTF, Pythia and UrQMD. Moreover, there are generators developed by the collaborations for specific physics studies such as for the electromagnetic form factor studies, Drell-Yan processes, and hypernuclei program. Event generators produce reactions in beam-target and beam-beam interactions in accordance to measured or theoretically predicted models. They consider the masses of particles, momenta and energies, quantum numbers, decay lengths and decay widths. The generated events are primary particles and input for the next stage of particle propagation. For the work presented in this thesis, two generators were used. These generators, EvtGen and DPM, are employed for the analysis that is described in Chapter 4.

EvtGen package has been developed in the late 1990s to simulate events of B decays. It originates from the electron-positron collider experiments BaBar and CLEO. EvtGen is used for producing signal events of the channel which is indicated by an input decay file. In a decay file, the user can specify the type of the decay, the constituting particles, the decay widths and model, and each decay channel can be reproduced by a decay model. EvtGen uses the decay amplitudes to calculate each node of the entire decay chain, including all angular and time-dependent correlations [109]. More than 150 decay models are defined for well-known particle decays. Decay amplitudes and particle parameters are stored in text-based databases, which can be extended easily.

DPM is another event generator, and it is based on the Dual Parton Model (DPM). It is generally used to describe high-energy collisions between two hadrons, two nuclei, or a hadron and a nucleus [110]. DPM in $\bar{\text{P}}$ANDA is used to describe inelastic and elastic hadronic processes as well as Coulomb elastic scattering processes. This generator is commonly used for background studies in $\bar{\text{P}}$ANDA.

Particle Transport and Digitization

Once particles and their decays are simulated, they need to be propagated through the detector and its magnetic field. The two propagators, GEANT3 and GEANT4 are available for this purpose. These are developed by groups involved in CERN experiments. Both have the same functionality, but they differ in performance and results because of their respective underlying models. The Virtual Monte Carlo interface (VMC) allows to switch between the different GEANT-versions as well as to introduce other packages. The propagators use a step-wise approach to simulate the particle's passage through detectors and interaction with materials. Each time, it evaluates the probabilities for bremsstrahlung, multiple scattering, particle decay, and so on. The information about the interaction of the particle with the detector material such as position and energy loss is saved for each event and the output of this step is called MCHits and it is accessible via the Root file.

The last step in simulating the detector's behavior is the digitization. All Monte Carlo data are processed to model the detector and electronic responses. The threshold, efficiency and amplification can be adjusted according to the measurements of real detector response. The goal is to make the simulated data as similar as possible to the real hits coming from an actual experiment. These output data are called DigiHits and are used as input information for the reconstruction of the events.

Reconstruction

The reconstruction step is the first common stage for simulated and experimental data from $\bar{\text{P}}$ANDA. In this step the digitized data is subject to a local reconstruction procedure which converts (DigiHits), the individual hits of each sub-detector to a physical meaning, like a 3D space point (x, y, z coordinates), deposited energy or a Cherenkov angle. After that, the computed trajectories of the particles are associated to particle types in the PID, recreating the full information of the particle.

Track reconstruction The track object provides information about a charged particle path through space. It contains a collection of hits in the individual tracking sub-detectors (MVD, STT, GEM and FTS). Generally, tracking can be separated into two tasks: track finding and track fitting. Track finding searches for hits created from one common particle. $\bar{\text{P}}$ANDA has four main sub-detectors dedicated to track reconstruction, the MVD, the STT, the GEM and the FTS. The next step in track reconstruction is track fitting. Track fitting performs the best-fitting track through a given set of hit points by using the package Genfit [112]. Genfit uses a Kalman filter [112, 113] for precise track fitting by considering magnetic field, detector material and the geometrical effects. Neutral candidates, which are invisible for the tracking detectors, are reconstructed by analyzing the EMC hit clusters.

Particle identification (PID) Good particle identification for charged leptons and hadrons plays an essential role for $\bar{\text{P}}$ANDA and it must cover a large momentum range from 200 MeV/c up to approximately 10 GeV/c. In the particle identification step, different subdetector information are combined, like dE/dx values from the MVD and STT, the Cherenkov angle from the DIRCs, or the energy deposit in the EMC. In the first stage, the recognition is done for each detector individually. A charged particle is tested to determine how likely is one of the possible particles hypotheses (e, μ, π, K and p) [9]. For every sub-detector, a particle is assigned a PID number, a set of probabilities for it to be one of the five particle hypotheses. The probabilities are normalized uniquely by assuming same fluxes for each particle species. In the second stage, the global PID combines this information by applying a standard likelihood method, and a global probability is calculated.

Physics Analysis Tools

By applying the previous steps, track reconstruction and PID, the tracks are found and the particles are identified. PandaRoot offers functionality to analyze the particles and events reconstructed in the previous chain on a high level. The analysis is enabled by means of tools and the analysis user has the choice to reconstruct decay trees, perform geometrical and kinematic fits and so on, provided by the analysis software. The main tools are briefly introduced in the following.

Rho package The Rho package is an analysis tool kit which is optimised for interactive work and performance [114]. Rho is included into PandaRoot and extended by specific functionalities. It offers methods for combining the particles to composite particles and takes care of combining daughter particles to reconstruct the decay tree without double counting by indexing the can-

didates. Particles are structured in candidate lists (RhoCandList). Different fitting methods are also included into Rho. Rho can apply selection criteria and run fitters on combined candidates sequentially and store the output in ROOT's TTree structure. It is very helpful and enables swift and interactive evaluation of the analysed events.

Vertex fit One of the important tasks in data analysis is finding a signal in a vast amount of background. Different kinds of fitters (vertex, momentum, energy and mass constraints) can be used, depending on the particular analysis under consideration. A very common situation is that the reconstructed particles originate from a common point in space-time. The spatial component is called the vertex. The vertex fitter constrains the trajectory of charged particles to come from a common vertex. It varies the measured track parameters of daughter particles within their measurement uncertainties, so the track comes as close as possible to the hypothetical vertex [113].

Mass constraint fit A mass constraint fitter checks the kinematics of composite candidates to reject background combinations. It fixes the mass of a composite candidate to the PDG value by varying the other kinematic variables accordingly. It is suitable for resonances or particles with a width that is negligible compared to the detector's mass resolution. Usually, the fitted mass is located in a spike at the nominal mass, so the mass resolution of the reconstructed candidates cannot be evaluated after applying this fitting.

4-Vector constraints kinematic fit This fitter performs a so-called four-constraint fit. In the case of an exclusive event reconstruction, it makes use of the component wise energy and momentum conservation of the initial four momentum of the beam and target. The sums of the three momenta and energies of all final-state particles will be matched to their initial values [115]. This constraint usually results in a significant background suppression as well as improved resolution for intermediate states.

Chapter 4

Simulation and Reconstruction Studies of the $\Lambda_c\bar{\Lambda}_c$ Channel

The $\bar{\text{P}}$ANDA experiment will study a large variety of physics topics. A detailed overview of these topics is presented in chapter 3. Of interest to this work, the experimental capabilities in the field of heavy baryons were discussed in section 3.2. There is a strong interest in the cross-section of charmed hadron production in the proton-antiproton collisions to be measured by the future $\bar{\text{P}}$ANDA experiment. In this chapter, the reaction $p\bar{p} \to \Lambda_c\bar{\Lambda}_c$ will be analyzed to understand the potential performance of the setup with such a short-lived heavy baryon. Different theoretical models have predicted cross sections of $p\bar{p} \to \Lambda_c\bar{\Lambda}_c$. Depending on the model assumptions, cross section values in the range from a few nb to a few μb have been estimated [116, 117, 118]. For the planning of the experiment, it is necessary to study the cross section sensitivity for this channel. This chapter describes the results of a Monte Carlo study that addresses this aspect. Prior to presenting the results, we start with a motivation and give a concise overview of the theoretical predictions for the channel of interest.

4.1 Motivation

The first charmed-baryon states were detected in 1975 in neutrino interactions [119]. Since then, many new excited charmed-baryon states have been discovered at the CLEO [120], BABAR [121], and Belle [122] facilities. However, the production and spectroscopy of the charmed-baryons have not been explored

in the same detail as the charmonium states, although they can provide similar information about the quark confinement mechanism. In fact, due to the presence of three quarks (two light and one heavy), such a system contains more information than a two-quark configuration. Most of the current experimental information about the properties of the ground state charmed-baryon, $\Lambda_c(udc)$, has been derived from electron-positron annihilation experiments. In the near future, charmed-baryons will be studied via their production in proton-antiproton annihilations with $\bar{\text{P}}$ANDA at FAIR. The Λ_c is the lightest charmed-baryon with a mass of 2.286 GeV/c^2. Heavier charmed-baryons often decay via a Λ_c, which makes the Λ_c reconstruction a necessity for charmed-baryon spectroscopy.

In this analysis, the feasibility of the Λ_c reconstruction is studied by looking at the decay channel $p\bar{p} \to \Lambda_c\bar{\Lambda}_c \to p^+K^-\pi^+\bar{p}K^+\pi^-$. The final state products of the studied reaction chain are all charged particles. Additionally, with a branching ratio of (6.35±0.33)%, it is one of the most favorable modes of decay [125]. The production threshold for the reaction $p\bar{p} \to \Lambda_c\bar{\Lambda}_c$ lies at an antiproton beam momentum of 10.162 GeV/c. The beam energy of antiprotons can be chosen such that it is well above the threshold. In this thesis, the high beam momentum of 14 GeV/c, available at $\bar{\text{P}}$ANDA has been selected. A high incident beam momentum has been chosen because it has been predicted that the production cross section for the channel of interest increases with momentum.

4.2 Cross Section Predictions

Providing a reliable estimate of the charm production cross section in $p\bar{p}$ collisions, appears to be very difficult. Several models of charm production can be found in the literature [117, 118, 123, 124], which their predictions differ by several orders of magnitude. Models described in [123] and [124] predict $p\bar{p} \to \Lambda_c\bar{\Lambda}_c$ cross sections, $\sigma_{p\bar{p}\to\Lambda_c\bar{\Lambda}_c}$, in the order of up to a few μb, as can be seen in Fig. 4.1(b)(c). The cross section predictions from Ref. [117] are expected to be on the order of several nb, or at most a quarter μb; see Fig. 4.1(a). For the calculations presented in Fig. 4.1(a), the production of charmed-baryons and mesons is considered in the proton-antiproton binary reactions at the energies of the future $\bar{\text{P}}$ANDA experiment. To describe these processes in terms of hadronic interaction models, one needs the values of the strong couplings of the initial nucleons with the intermediate and final-state charmed hadrons. In this method, described by A. Khodjamirian [117], finite

masses of charm quarks are taken into account. The strong couplings have been calculated by employing the Kaidalovs quark-gluon string (QGS) model with Regge poles and adjusting the normalization of the amplitudes [126]. In the QGS model, the amplitudes of binary reactions, such as $p\bar{p} \to \Lambda_c\bar{\Lambda}_c$ or $p\bar{p} \to D^0\bar{D}^0$ are described by quark line diagrams depicted in Fig. 4.2. These diagrams have a dual interpretation. From the s-channel point of view, the annihilation of the slow $u\bar{u}$ or $d\bar{d}$-pair from the initial proton and antiproton is followed by a creation of the $c\bar{c}$ pair. The spectator quarks and antiquarks from the initial proton and antiproton coalesce with the created quark and antiquark to form the final-state charmed hadrons. The intermediate state in s-channel represents a sort of a diquark-antidiquark or quark-antiquark string shown in Fig. 4.2(a) and (b), respectively. In this model, the estimated production cross section for $p\bar{p} \to \Lambda_c\bar{\Lambda}_c$ can reach several tens of nb at the beam momentum of 15 GeV/c [117].

Fig. 4.1(b) represents another calculation of the charm-production reactions $p\bar{p} \to \Lambda_c\bar{\Lambda}_c$, done by the Jülich group [123]. This approach is based on the Jülich meson-baryon model that was employed earlier to investigate the $p\bar{p} \to \Lambda\bar{\Lambda}$ reaction and the model is extended to the charm sector within a similar strategy. In this model, these reactions are considered within a coupled-channels framework. The elementary charm production process is described by either baryon/meson exchange or by quark/gluon dynamics, and the effects of the interactions in the initial and final-states are taken into account, whereas most other approaches do not consider these interactions. The predictions for $\sigma_{p\bar{p}\to\Lambda_c\bar{\Lambda}_c}$ are in the order of 1 to 7 μb, close to the production threshold. They are 100 to 1000 times larger than predictions of other model calculations given in the literature [123].

Finally, Fig. 4.1(c) depicts the cross-section predictions described by R. Shyam and H. Lenske [124]. In this model the charmed-baryon production reaction $p\bar{p} \to \Lambda_c\bar{\Lambda}_c$ is investigated within a single-channel effective Lagrangian model. In this approach the reaction is described by using the t-channel D^0 and D^{*0} meson-exchange diagrams within an effective Lagrangian model, involving the physical hadron masses and the coupling constants determined from SU(4) flavor symmetry. The predicted $\Lambda_c\bar{\Lambda}_c$ production cross sections is in the range of 1 to 30 μb for antiproton beam momenta up to 20 GeV/c [124].

Comparing the predictions of the various models shows that the cross section is very sensitive to the degrees-of-freedom that play a role in the production if charmed-baryons. Therefore, a cross section measurement will provide valuable insights in the dynamics in such a process. The question is what the sensitivity is of $\bar{\text{P}}$ANDA to measure such a quantity at the various stages of data taking. This aspect will be addressed in the next sections.

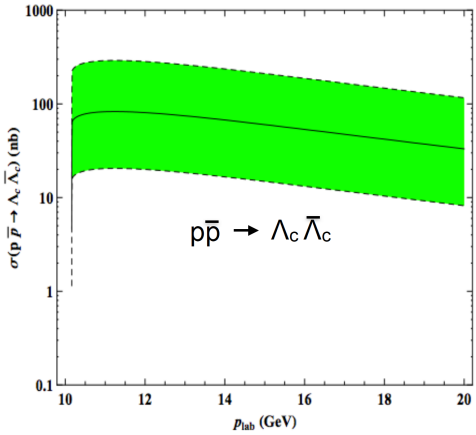

(a)

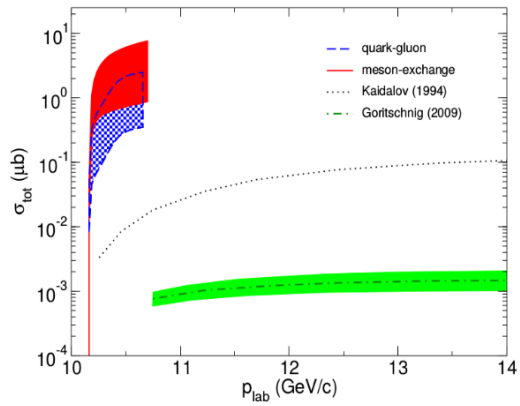

(b)

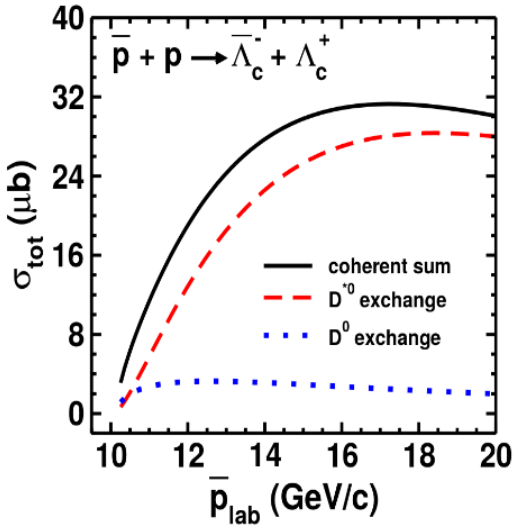

(c)

Figure 4.1: (a) The total cross-sections of charmed-baryon pair production in $p\bar{p}$ collisions in the QGS model. The green band indicates the uncertainties [117]. (b) Total reaction cross sections, represented in red shaded band and blue grid, for $p\bar{p} \to \Lambda_c\bar{\Lambda}_c$ as a function of p_{lab} and according to the Jülich model [127]. The dotted curve represents the study reported in the paper published by A.B. Kaidalov and P.E. Volkovitsky [118]. In this study, a quark-gluon string model together with Regge asymptotics for hadron amplitudes has been used. The green bands represent another study reported in the paper published by A.T. Goritschnig [116]. In this study, the $p\bar{p} \to \Lambda_c\bar{\Lambda}_c$ reaction has been described within a handbag approach where the amplitude is calculated by convolutions of hard sub-process kernels (representing the process $u\bar{u} \to c\bar{c}$) and the generalized parton distributions. (c) Total cross section for the reaction $p\bar{p} \to \Lambda_c\bar{\Lambda}_c$ as a function of the antiproton beam momentum. The contributions of the D^0 and D^{*0} exchange processes are shown by dotted and dashed lines, respectively [124]. Figures are taken from Refs. [117, 127, 124].

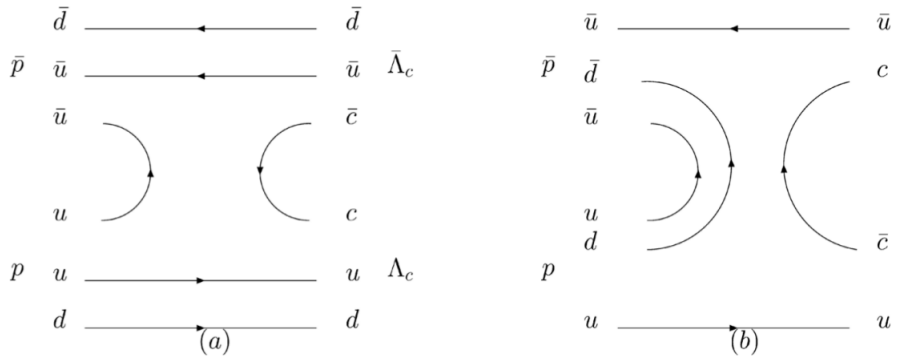

Figure 4.2: Quark line diagram of the production of a charmed-baryon (a) and meson (b), in $p\bar{p}$ collisions. Figure is taken from Ref. [117].

4.3 Simulation and Reconstruction of the Decay Channel with PandaRoot

The work presented in this chapter makes extensive use of the simulation and reconstruction chain provided by PandaRoot. The following summarizes the default parameters of the software setup used for the Monte Carlo (MC) production of signal and background events, their propagation through the various materials and modelling the responses of the readout electronics, track finding and fitting, and finally the Particle Identification (PID) (see section 3.5.2). The GEANT4 transport model has been used via the Virtual Monte Carlo interface [104]. The beam momentum is set 14.0 GeV/c. The corresponding masses of all particles which participate in the reaction chain are: $M_{\Lambda_c,\bar{\Lambda}_c} = 2.28646$ GeV/c^2, $M_{p,\bar{p}} = 0.93827$ GeV/c^2, $M_{K^+,K^-} = 0.49368$ GeV/c^2, $M_{\pi^+,\pi^-} = 0.13957$ GeV/c^2 [125]. A total of 10^5 signal events and 2.243×10^7 background (DPM) events have been generated. For the identification of the final-state particles, the implemented algorithm retrieves information from the following sub-detectors, MVD, STT, EMC, DISK, DIRC, RICH and TOF. The final probability is calculated by the normalized multiplication of probabilities of each sub-detector. For the current analysis, Feb17 release of PandaRoot has been used, which combines with FairSoft and FairRoot external packages of version may16p1 and v-17.10b, respectively. Within the PandaRoot simulation framework, the different substructures of the $\bar{\text{P}}$ANDA detector, as described in section 3.3, can be included in or excluded to the simulation process.

In this study, the complete setup was used. The simulation included the following components:

- The beam and target pipes.
- The superconducting solenoid in the TS and the dipole in the FS, with the full field map.
- The Micro Vertex Detector (MVD).
- The Straw Tube Tracker (STT).
- All three Gas Electron Multipliers (GEM) stations.
- The barrel Time-Of-Flight (TOF) and forward TOF.
- The barrel and disk DIRC.
- The complete muon system.
- The Forward Tracking System (FTS).
- The Ring Imaging CHerenkov Detector (RICH).
- The Electro Magnetic Calorimeters (EMC).

4.4 Event Generation

The Monte Carlo input for the feasibility study is produced with the EvtGenDirect event generator. The tool was introduced in section 3.5.2. Here, first the production of the charged Λ_c charmed-baryon pairs is outlined, then their decay to $p^{\pm}K^{\pm}\pi^{\pm}$ will be analyzed. Fig. 4.3(a) shows the sketch of the decay chain. The first task in the Monte Carlo simulation is to define the decay models used to simulate the signal events. For the processes, $p\bar{p} \to \Lambda_c\bar{\Lambda}_c$, $\Lambda_c \to p^+K^-\pi^+$ and $\bar{\Lambda}_c \to \pi^+\bar{p}K^+\pi^-$, the PHase SPace (PHSP) decay model is used. PHSP provides a generic decay of particles according to a phase space distribution, where the spin of all particles in the initial and final-states are averaged [128]. Λ_c charmed-baryon pairs are produced using a custom decay file in EvtGen to create only particles of the signal channel. A total of 10^5 signal events has been generated. After the generation, the particles are propagated through the full detector setup; see section 4.3.2, and digitized according to the readout characteristics. The following reconstruction consists of track finding, particle identification, and event analysis.

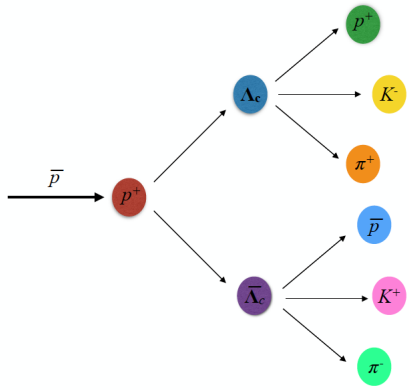

(a)

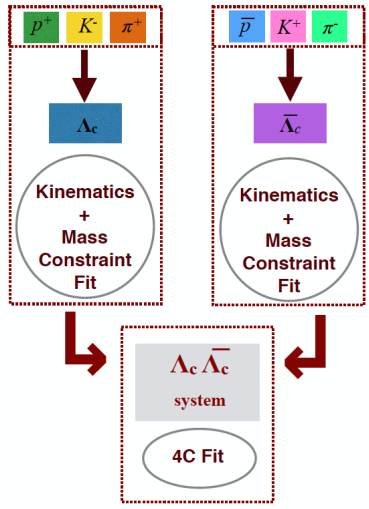

(b)

Figure 4.3: (a) Sketch of the reaction chain. (b) Sketch of the strategy used for the reconstruction of the Λ_c $\bar{\Lambda}_c$ system.

Fig. 4.3(b) shows the reconstruction strategy used for the reconstruction of the $\Lambda_c\bar{\Lambda}_c$ system. At a beam momentum of 14 GeV/c, the distribution of the transverse versus longitudinal momentum is constrained to an ellipse for this two-body intermediate state $\Lambda_c\bar{\Lambda}_c$, as shown in Fig. 4.4(a). Longitudinally, a uniformly distributed momentum spectrum is observed. Fig. 4.4(b), shows that Λ_c and $\bar{\Lambda}_c$ are produced at small angles ($< 13^\circ$) with respect to the beam axis. The selected decay pattern for the Λ_c, and $\bar{\Lambda}_c$ foresees three daughter

particles, $\Lambda_c \to p^+K^-\pi^+$ and $\bar{\Lambda}_c \to \bar{p}K^+\pi^-$. The kinematics of these tracks is much less restricted than in the case of the mother particle. Fig. 4.5 shows the transverse versus longitudinal momentum distributions of the final-state particles from the $\Lambda_c \to p^+K^-\pi^+$ and $\bar{\Lambda}_c \to \bar{p}K^+\pi^-$. In contrast to the distributions of Λ_c and $\bar{\Lambda}_c$ which have a precisely defined ellipse, the ellipse shaped distributions of their decay products are broader. The spread in the distributions has two sources; it is not a two-body decay and the momentum of the mother particle varies from event-to-event. Fig. 4.6 shows the distributions of the scattering angle versus longitudinal momentum of the six final-state particles. The pions reach larger polar angles than the protons and kaons because of their lighter mass.

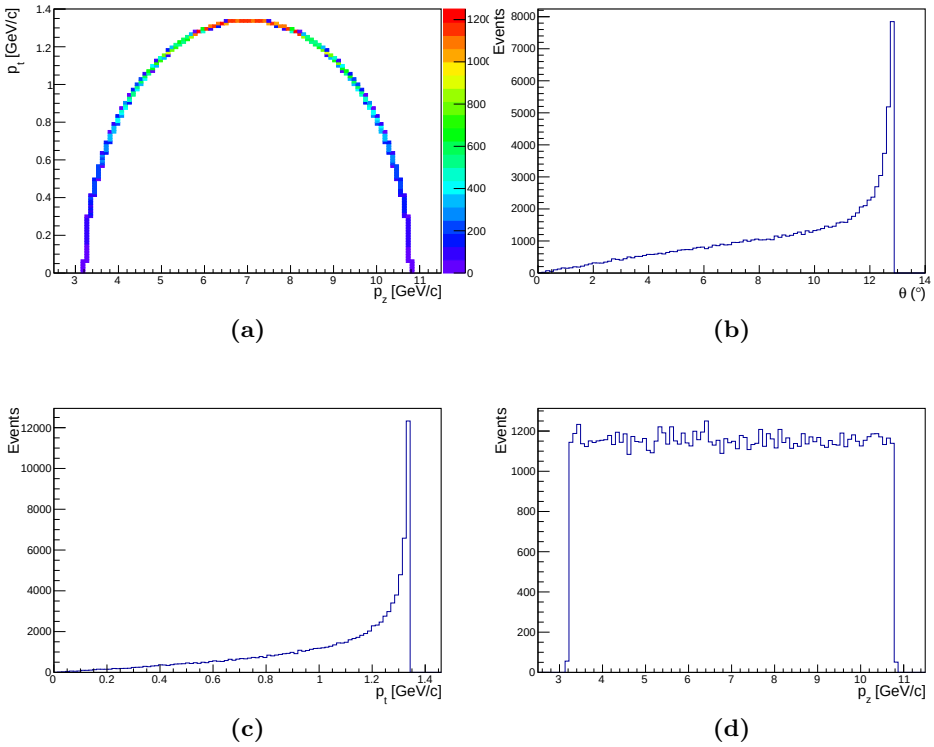

Figure 4.4: (a) Correlation between transverse momentum and longitudinal momentum for the generated Λ_c, (b) Λ_c angular distribution, (c) transverse momentum distribution (p_t) for Λ_c, and (d) longitudinal momentum distribution (p_z) for Λ_c.

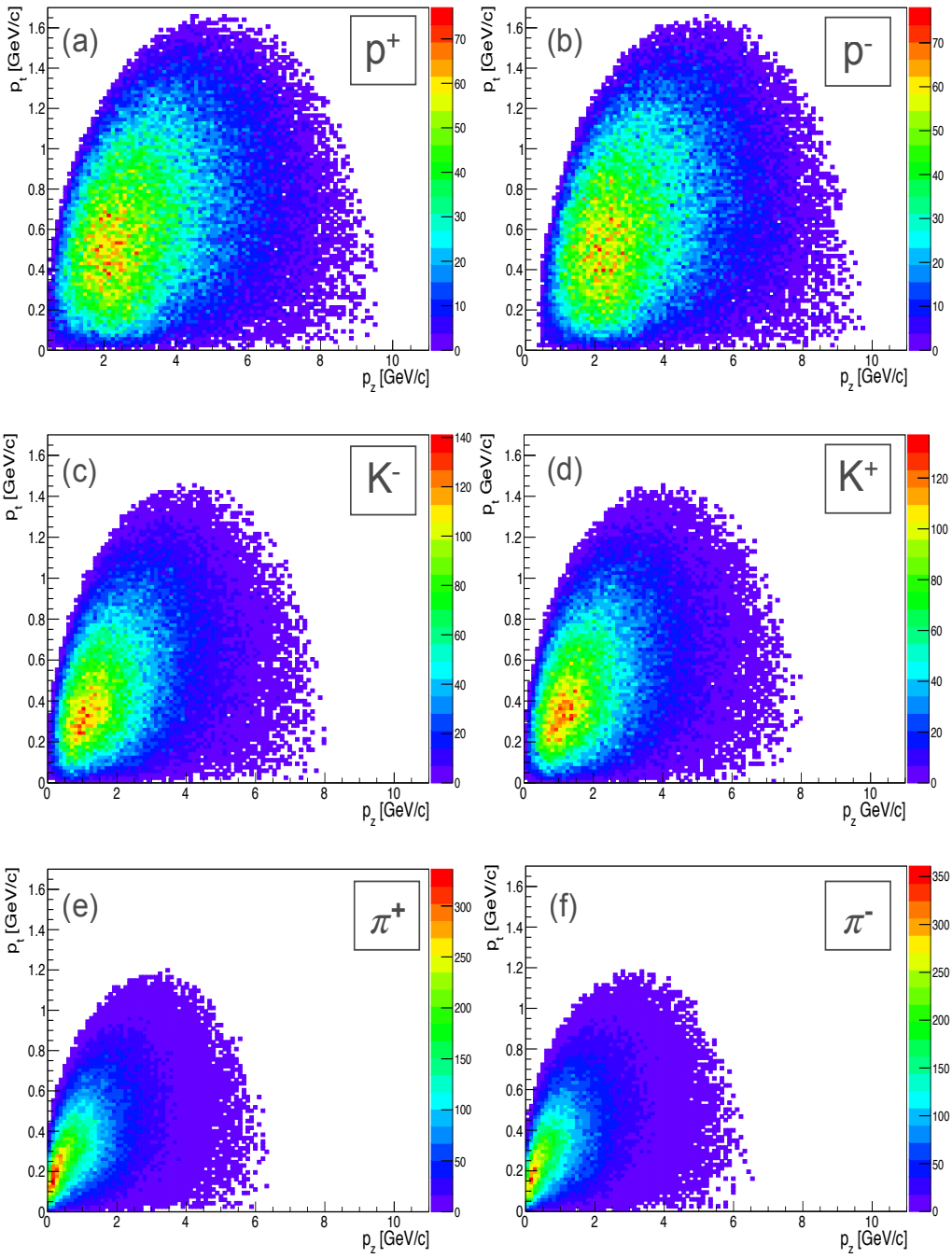

Figure 4.5: Generated p_t vs. p_z distributions for (a) proton, (b) antiproton, (c) K^-, (d) K^+, (e) π^+, and (f) π^-.

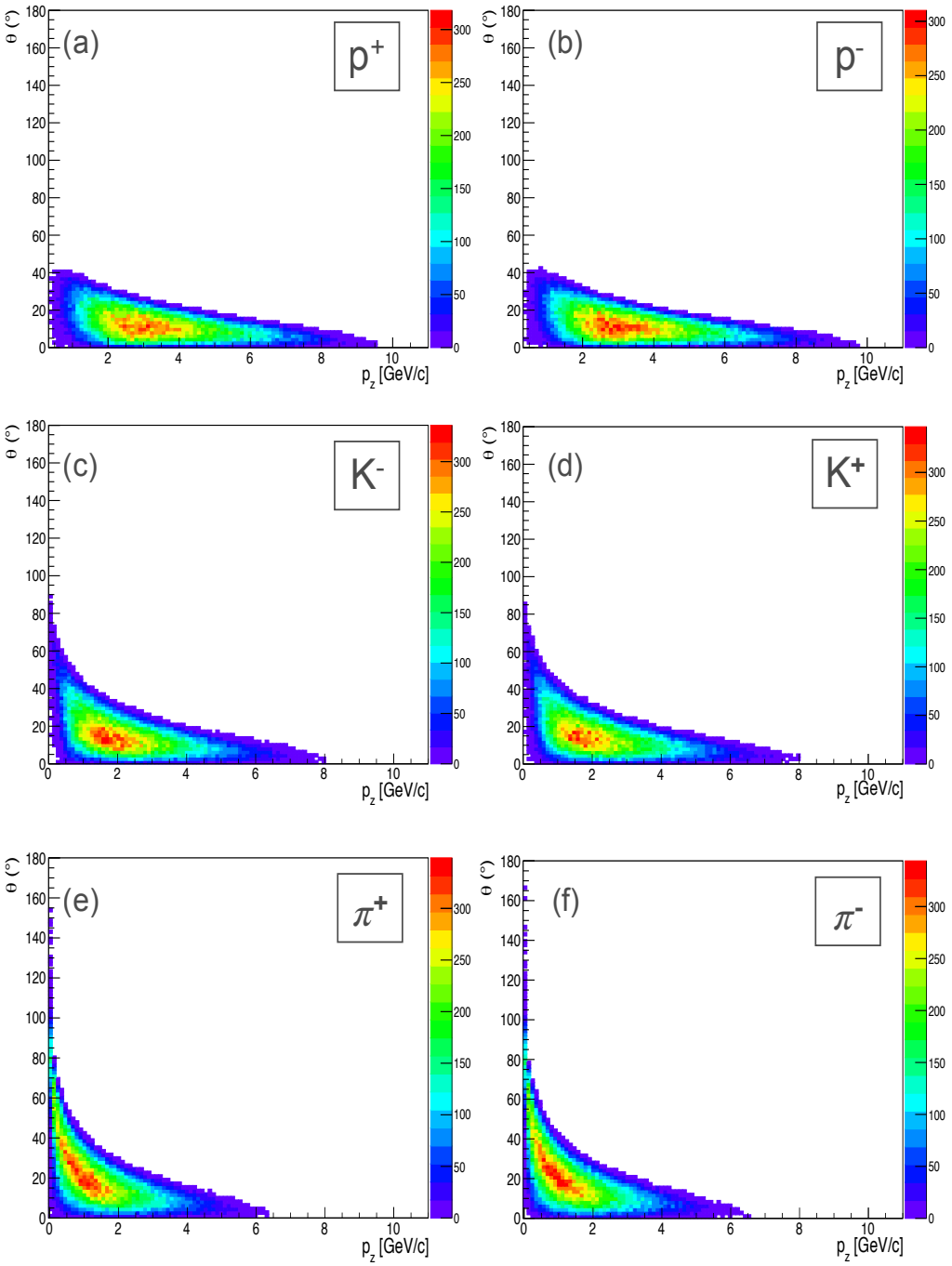

Figure 4.6: Scattering angle versus longitudinal momentum distributions for (a) proton, (b) antiproton, (c) K^-, (d) K^+, (e)π^+, and (f) π^-.

4.5 Event Reconstruction and Particle Identification

$\bar{\text{P}}$ANDA has four main sub-detectors dedicated to track reconstruction: the MVD, the STT, the GEM and the FTS. As explained in the previous sections, the Λ_c baryon pairs decay into charged particles, which create hits in the sub-detectors. To investigate the number of hits associated to each of the charged tracks, the multiplicity distribution of two sub-detectors, STT and MVD, are presented in this section. Fig. 4.7 shows the distributions of the number of STT hits associated to each of the final-state particle species.

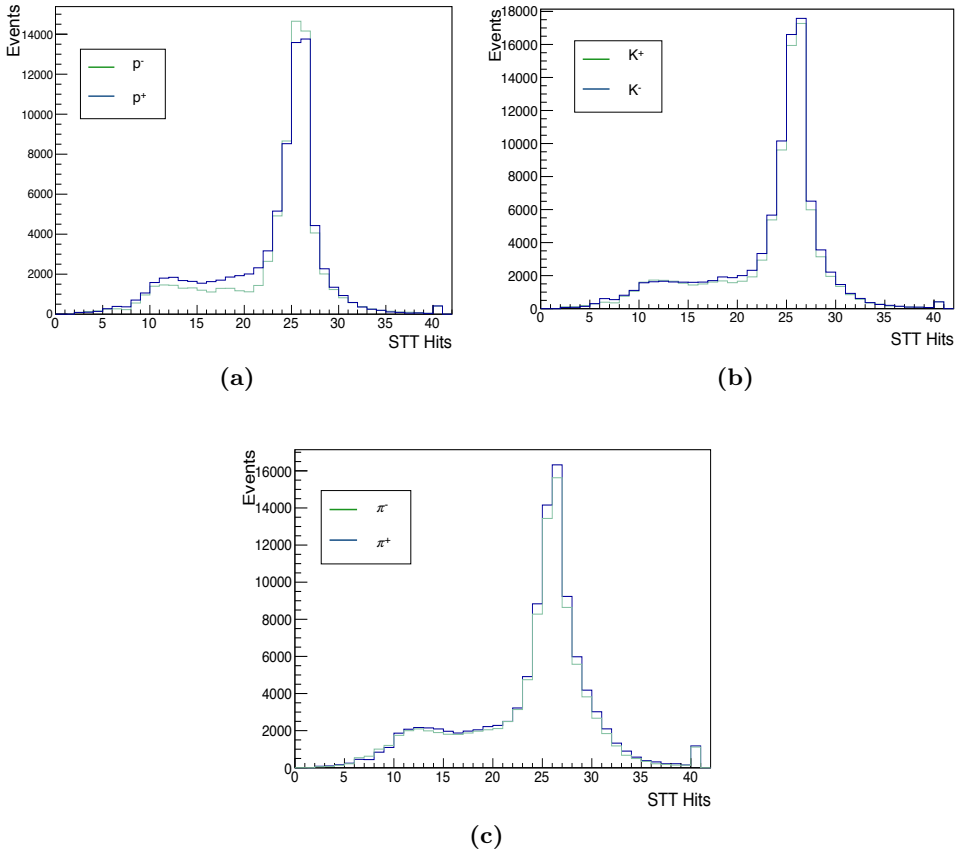

Figure 4.7: Hit multiplicity distribution in the STT detector for (a) protons and anti-protons, (b) kaons, and (c) pions.

The distributions show a peak at around 25 hits per particle track which then decreases towards higher hit numbers, which is expected for these particle types and the momentum region (see section 3.3.2). The low number of hits

corresponds to the particles scattered at small angles ($< 20°$). Fig. 4.8 shows the hit multiplicity distribution of the MVD for the reconstructed tracks. More than 65% of the daughter particles (protons, kaons and pions) leave 4±1 hits in the MVD. The low fraction of the daughter particles with no hits in the MVD is notable ($< 6\%$), underlining the importance of the MVD for particle reconstruction.

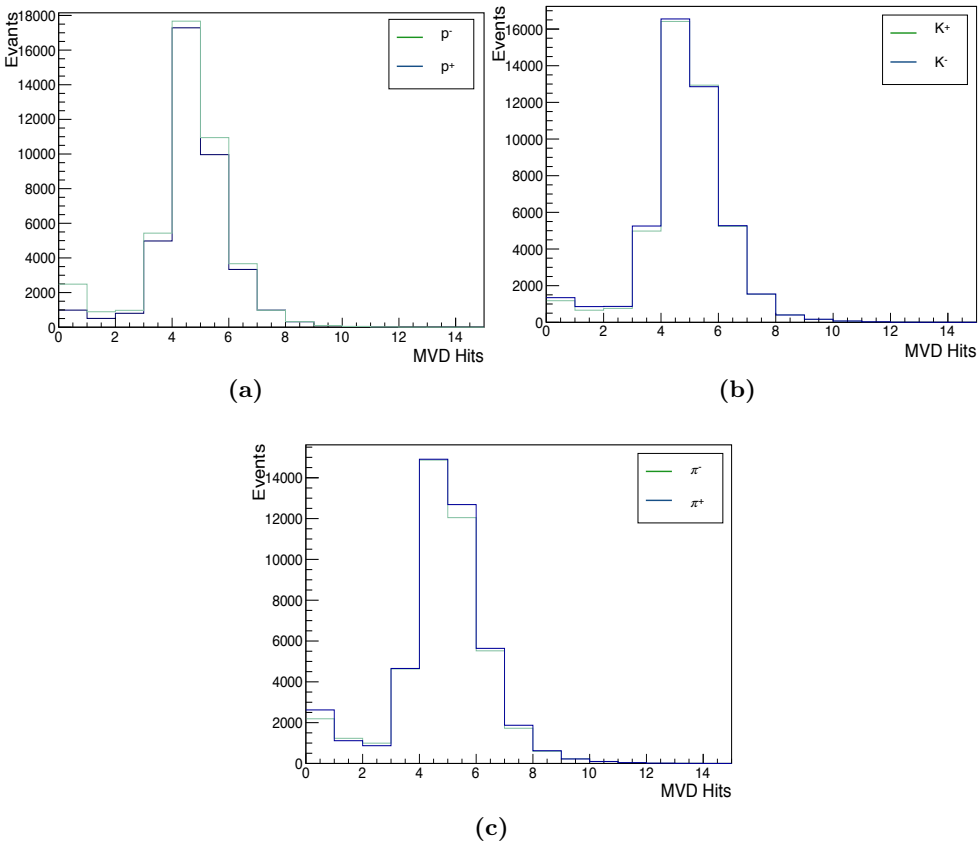

Figure 4.8: Hit multiplicity distribution in the MVD detector for (a) protons and anti-protons, (b) kaons, and (c) pions.

To further analyze the charged particle tracks, an investigation is performed to show the contribution of the PID detectors. To achieve this goal, the multiplicity distributions of the reconstructed tracks, identified as protons, kaons, and pions for different combinations of PID detectors were analyzed. Since one part of this thesis is devoted to an in-beam test measurement of the STT prototype, the role and contribution of the STT in the particle identification is highlighted in this section. Fig. 4.9 shows the multiplicity distributions

of the reconstructed tracks of the three charged particles, using different PID algorithms. The multiplicity distributions look the same for the charge conjugates. As shown in Fig. 4.9, the blue histograms show the contribution of all PID detectors, the red and green histograms represent the contribution of the

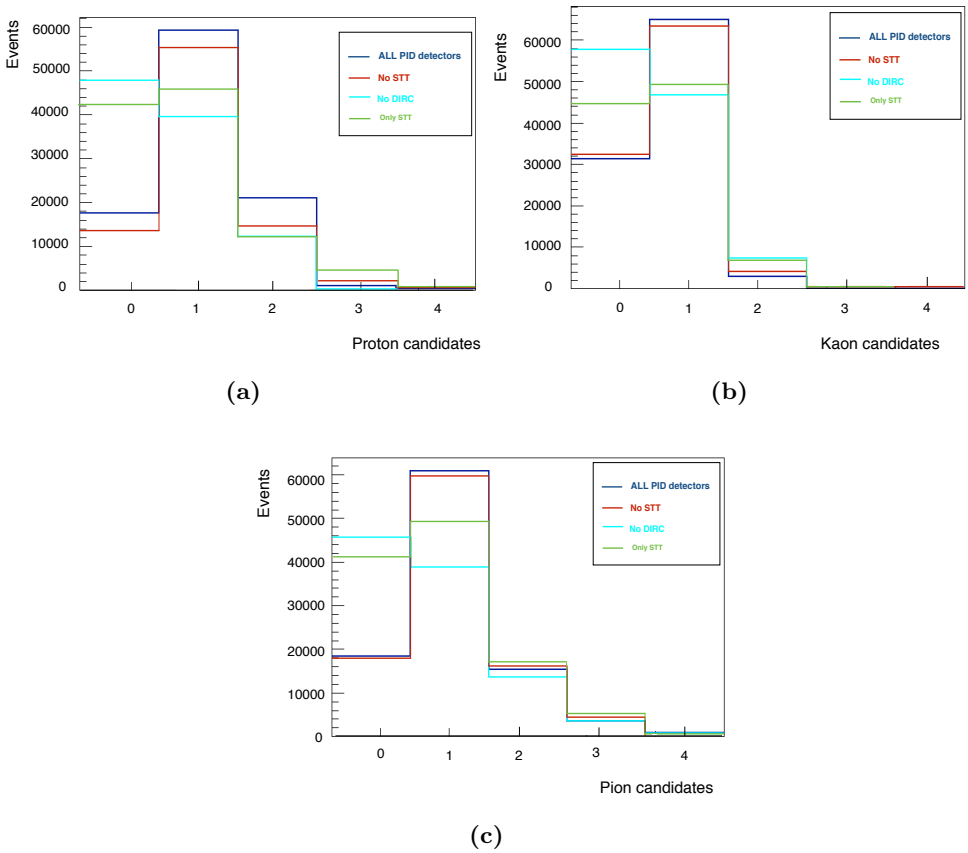

Figure 4.9: Multiplicity distribution for the reconstructed decay particles for different PIDs for (a) proton, (b) K^- and (c) π^+.

STT detector, with no STT detector and with only STT detector including in the PID, respectively. The cyan histograms show the multiplicity distribution when the DIRC detector does not contribute for the PID. For our studied decay channel, many particles have high momentum and the DIRC detector performs the PID in the high momentum region. For this reason, the contribution of the DIRC is also studied in addition. The multiplicity of zero candidates imply that the reconstruction did not succeed. For our channel of interest, the STT has a marginal contribution to the PID performance. A large fraction of the final-state particles has relativistic velocities, therefore, the energy loss dE/dx

reaches that of minimum ionizing particles for most cases. This is illustrated in Fig. 4.10. Below momenta of about 1 GeV/c, one observes that the STT has sufficient resolving power to separate the different particle species. However, above this momentum, dE/dx has no added value for PID. Most of the particles in our decay channel have momenta that fall into this high momentum range. The STT will play an important role in the particle identification for decay channels, for which the daughter particles are in the momentum region below 1 GeV/c.

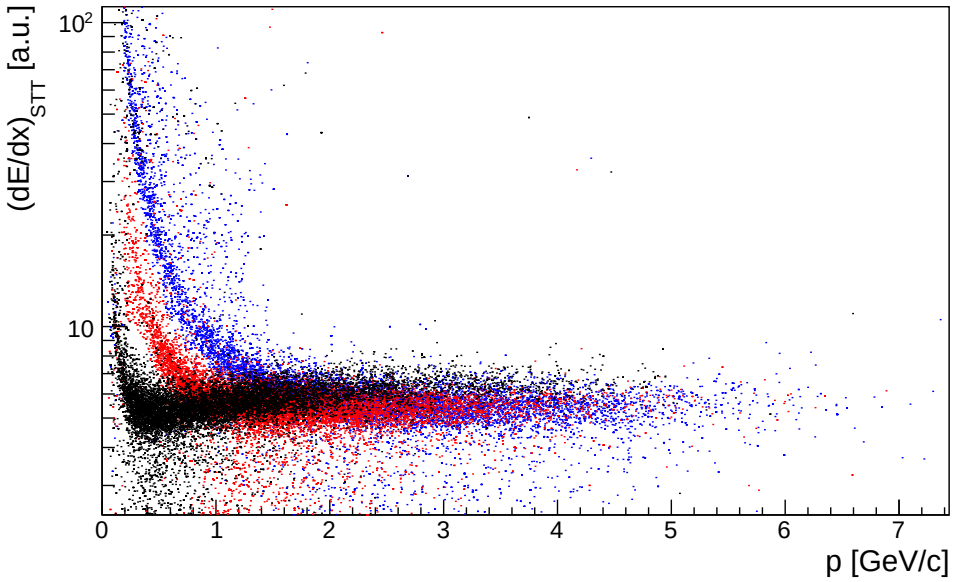

Figure 4.10: The energy loss (dE/dx) of the STT as a function of momentum (p) for protons (blue), kaon (red), and pions (black) originating from the decay $\Lambda_c \to p^+K^-\pi^+$.

We have combined the information of the pion, kaon, and (anti)proton candidates to reconstruct the four momentum of the Λ_c and $\bar{\Lambda}_c$ candidates. First, we discuss the reconstruction performances for each single final-state particle. After this, we analyzed the reconstruction performance for the combined Λ_c baryon candidates. For this higher-level analysis, we made use of the PID information of all detectors and Rho package that is part of the PandaRoot framework and described in section 4.3. Fig. 4.12 shows the multiplicity distributions of each final-state particle candidate similar to Fig. 4.9, however, for both particles and antiparticles and using all the PID detectors. We observe that in 57% (53%) of all events at least one antiproton (proton) candidate could be reconstructed. Similar efficiencies, 55% and 53%, have been observed for the K^+ and K^-, respectively. The highest efficiency of 64% and 61% is

found for the π^+ and π^- candidates, respectively. We also observe that for all six final state particles there are many events which are not properly reconstructed, and there is a systematic difference in the multiplicity spectra between the positive and negative particle candidates. The consequence will be that also the number of reconstructed Λ_c and $\bar{\Lambda}_c$ candidates will differ as demonstrated in Fig. 4.11. The four-momentum of the Λ_c can be obtained via its decay products, if at least one proton, one K^- and one π^+ are reconstructed. The multiplicity distribution is shown in Fig. 4.12. There are some events with more than one proton or antiproton, K^- or K^+, and π^+ or π^-. This leads to the reconstruction of more than one Λ_c or $\bar{\Lambda}_c$ per event which causes a combinatorial background. It is worth mentioning that we have made use of the reconstructed events which have a true MC counterpart (MC-truth matched). It means that only the events that have been matched with the generated ones are used. We did not considered the events which have zero Λ_c or $\bar{\Lambda}_c$ candidates (see Fig. 4.11). To compare the momentum and angular distributions of the reconstructed particles with the corresponding distributions of the generated particles, we investigate the reconstruction of the Λ_c and the $\bar{\Lambda}_c$ decays. It implies that six charged tracks, namely proton, antiproton, K^-, K^+, π^+ and π^- candidates have been detected. Fig. 4.12 shows the longitudinal momentum vs angular distribution of the daughter particles ($p^+K^-\pi^+$), and ($\bar{p}K^+\pi^-$), of assembled Λ_c and $\bar{\Lambda}_c$ baryons.

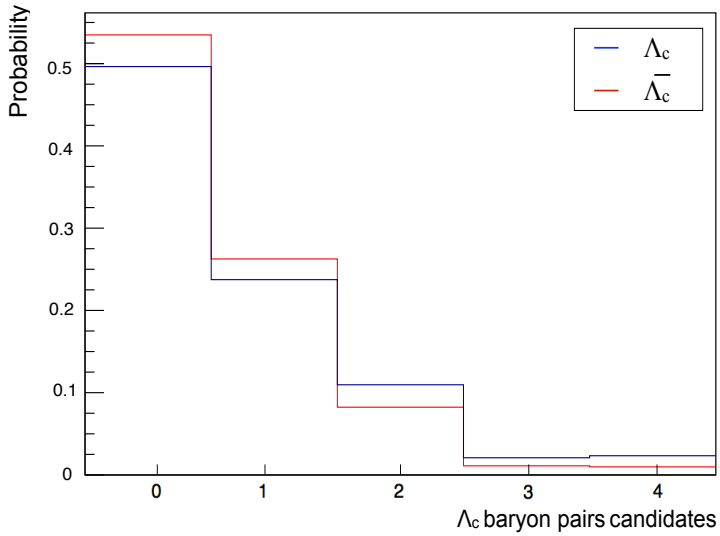

Figure 4.11: Relative multiplicity distribution for the reconstructed Λ_c and $\bar{\Lambda}_c$.

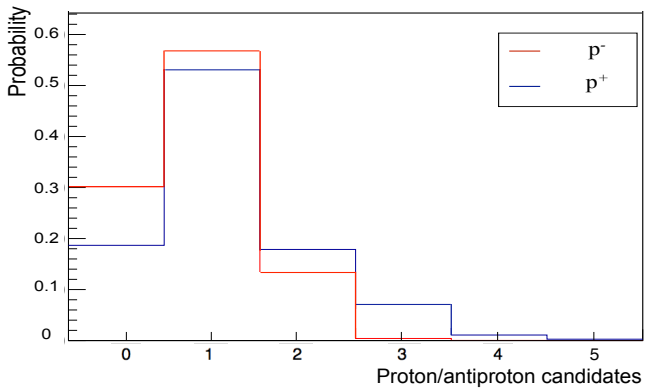

(a)

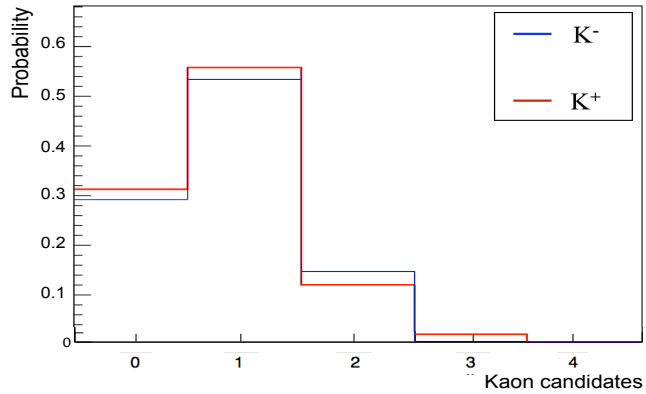

(b)

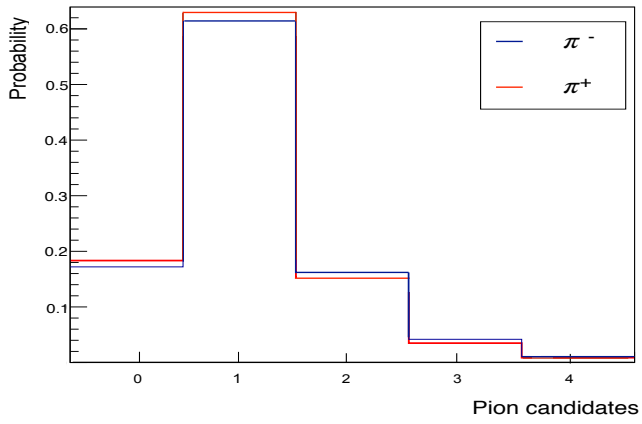

(c)

Figure 4.12: Relative multiplicity distribution for the reconstructed particles of the decay chain; (a) proton and antiproton, (b) K^-, K^+, and (c) π^+, π^-.

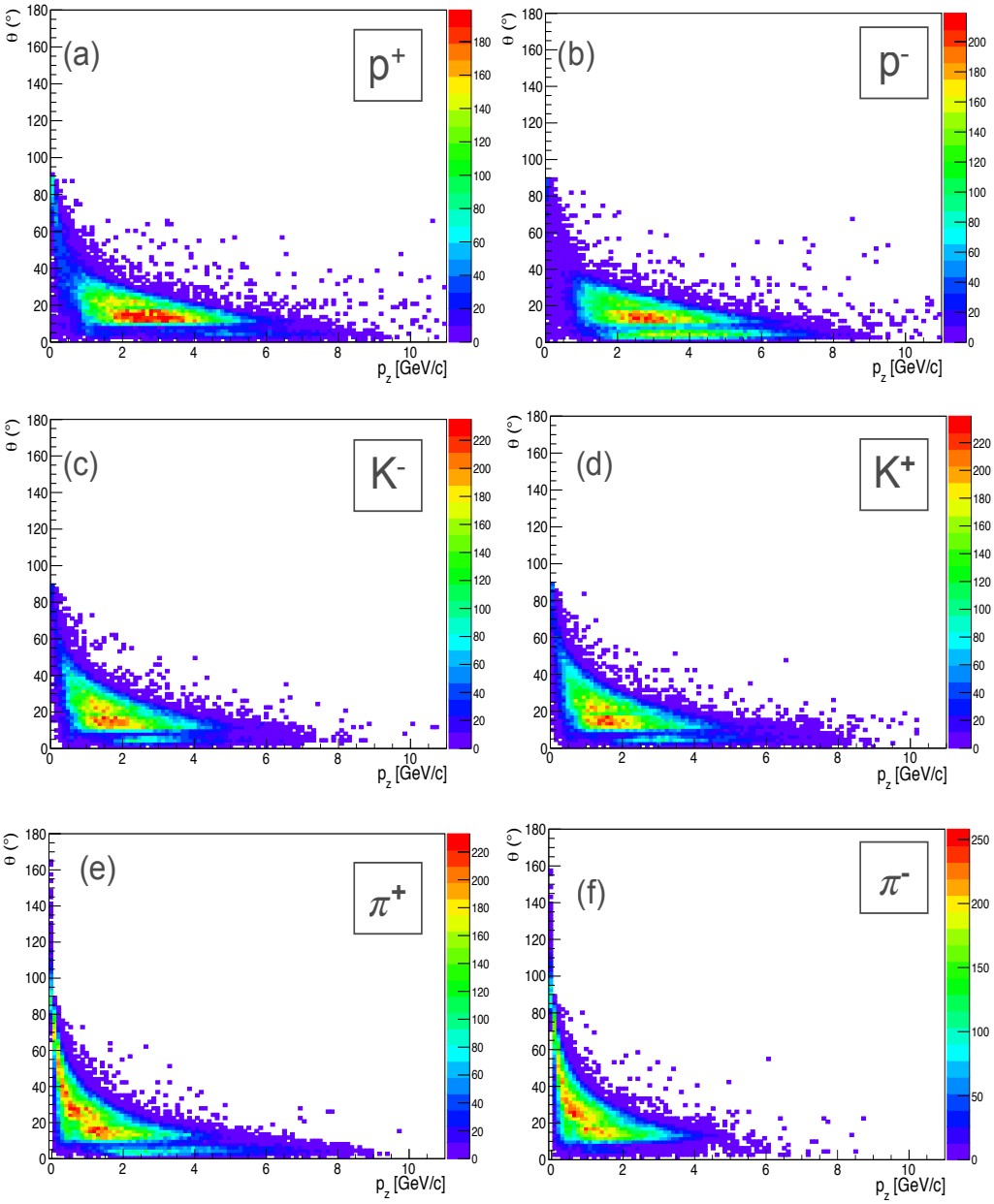

Figure 4.12: Longitudinal momentum vs angular distribution for the reconstructed (a) proton, (b) antiproton, (c) K^-, (d) K^+, (e) π^-, and (f) π^+.

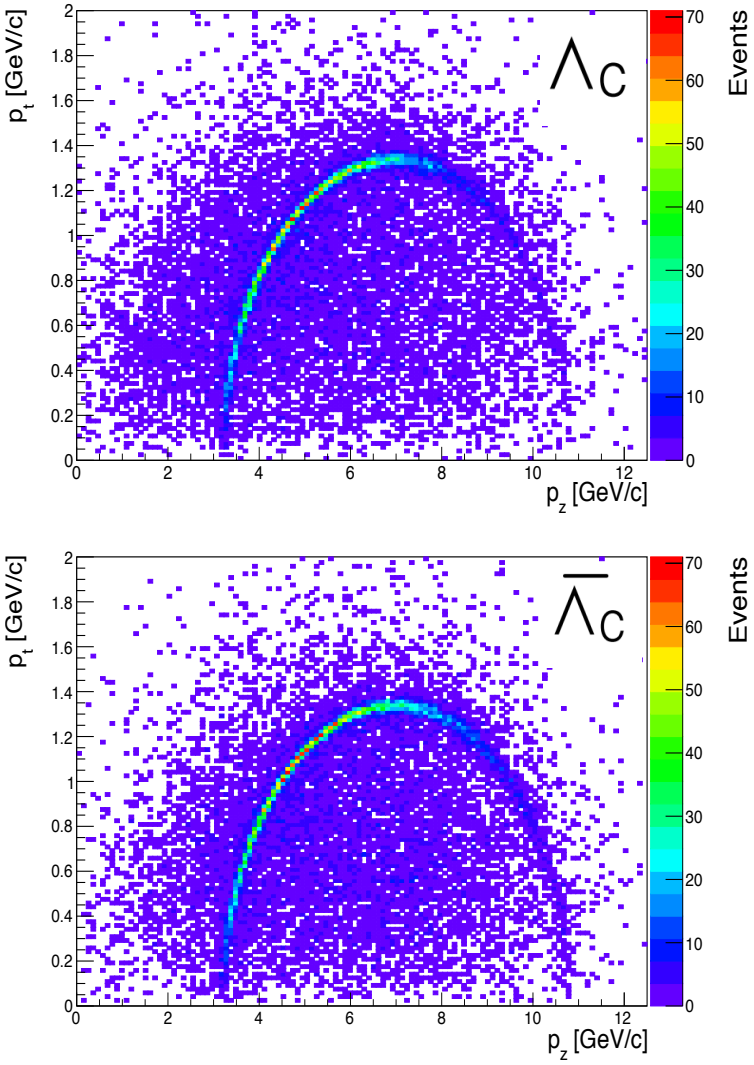

Figure 4.13: Correlation of transverse momentum versus longitudinal momentum for the reconstructed Λ_c (top) and $\bar{\Lambda}_c$ candidates (bottom).

The correlation depicted in Fig. 4.12 is very similar in its basic features as what was presented before for the generated information (see Fig. 4.6). It can be clearly seen in the Fig. 4.12 that daughter particles of both Λ_c and $\bar{\Lambda}_c$, show a drop at the polar angles $< 10°$. This behavior is due to the lack of acceptance in the FS, which leads to a reduction in the detection efficiency. We can also observe events that fall out of the kinematically allowed region which must be related to background or false reconstructed events. Fig. 4.13

shows the momentum distributions (transverse momentum versus longitudinal momentum) for both Λ_c and $\bar{\Lambda}_c$ reconstructed candidates. Also here, there are events that fall out of the allowed kinematics region. The distributions are not symmetric and it implies the efficiency losses for large longitudinal momenta, which influences the angular acceptance.

4.6 Event Analysis with Background Considerations

In this section, the physics channel $p\bar{p} \to \Lambda_c\bar{\Lambda}_c \to p^+K^-\pi^+\ \bar{p}K^+\pi^-$ is studied by performing both inclusive (single Λ_c baryon) and exclusive analysis (Λ_c baryon pair) reconstruction of the final state. Fig. 4.3(b) shows the strategy used for two different ways of the reconstruction. For the event analysis the Rhopackge available in PandaRoot is used by implementing the assumptions and parameters, summarized in section 4.3. During the analysis the basic kinematic cuts and two mass fits are applied. In the following, the results of the signal and background events are presented. To study the reconstruction performance of the decay channel under realistic conditions, the DPM background at the beam momentum that was used to populate our signal process needs to be considered. The total hadronic background has a much larger production cross section, making an effective background suppression necessary. Using the PndDpmDirect generator included in PandaRoot, 2.243×10^7 DPM events have been generated. The goal of this analysis is to reveal the capability of $\bar{\text{P}}$ANDA to detect the Λ_c baryons and to separate the signal and background events. In order to make a quantitative statement about the production of the Λ_c baryon pairs, we use the statistical significance as a figure-of-merit (FOM) that needs to be optimized. This FOM is obtained by the following expression:

$$FOM = \frac{N_{sig}}{\sqrt{N_{sig} + N_{bkg}}}. \tag{4.1}$$

In Eq. 4.1, N_{sig} is the number of signal events and N_{bkg} represents the number of background events. The number of signal events is given by

$$N_{sig} = L \times t \times \sigma_{sig} \times Bf \times \epsilon, \tag{4.2}$$

N_{bkg} is obtained from Eq. 4.3. In Eq. 4.2, where L is the luminosity of $\bar{\text{P}}$ANDA (2×10^{30} to 2×10^{32} $\text{cm}^{-2}\,\text{s}^{-1}$), t is the time of the data taking, σ_{sig} is the cross section of the signal, Bf is the branching fraction of the analysis decay,

which differs for the inclusive and the exclusive reconstruction. The branching fraction of our channel of interest is, $Bf_{\Lambda_c \to p^+K^-\pi^+} = (6.35 \pm 0.33)\%$. For the inclusive analysis Bf is $2\times$ 6.35% and for the exclusive analysis Bf equals 6.35% $\times$ 6.35%. In Eq. 4.2, ϵ is the efficiency which includes the reconstruction efficiency and the detector acceptance.

$$N_{bkg} = \frac{L \times t \times \sigma_{bkg}}{f_{supp}}. \tag{4.3}$$

In Eq. 4.2, σ_{bkg} is the cross section of the background which is about 42.2 mb [125] and f_{supp} is the suppression factor, obtained from the analysis of background events. In this section, the results obtained from both inclusive and exclusive reconstructions are presented. Each step of the analysis is explained. Moreover, we note that the cuts applied for both methods are the same for signal and background data.

Kinematic Cuts

We discuss the cuts applied to the kinematics of our decay channel in this section. The first cut is applied to the center-of-mass energy of Λ_c baryons, together with the second cut on the momentum and emission angle of the Λ_c baryons. The histograms presented here are for the Λ_c baryons, but the corresponding histograms for the $\bar{\Lambda}_c$ baryons are similar. Fig. 4.15 shows center-of-mass (CM) energy distributions of the Λ_c candidates for the signal and background events. In this figure, the chosen cut regions are indicated by the area between the two dashed lines. In addition to the CM energy, the second cut on the momentum and angular distribution can be used to reduce the background events even further. Fig. 4.16 show the correlation between the scattering angle and momentum distribution of Λ_c candidates for the signal and background events. It can be clearly seen that the background events have a different distribution. In Fig. 4.15, the cut region in both signal and background distributions is represented. A huge number of background events (> 75 %) lie out of this cut region, which is an effective suppression of the background. The cut regions were selected by optimizing the significance as given in Eq. 4.1.

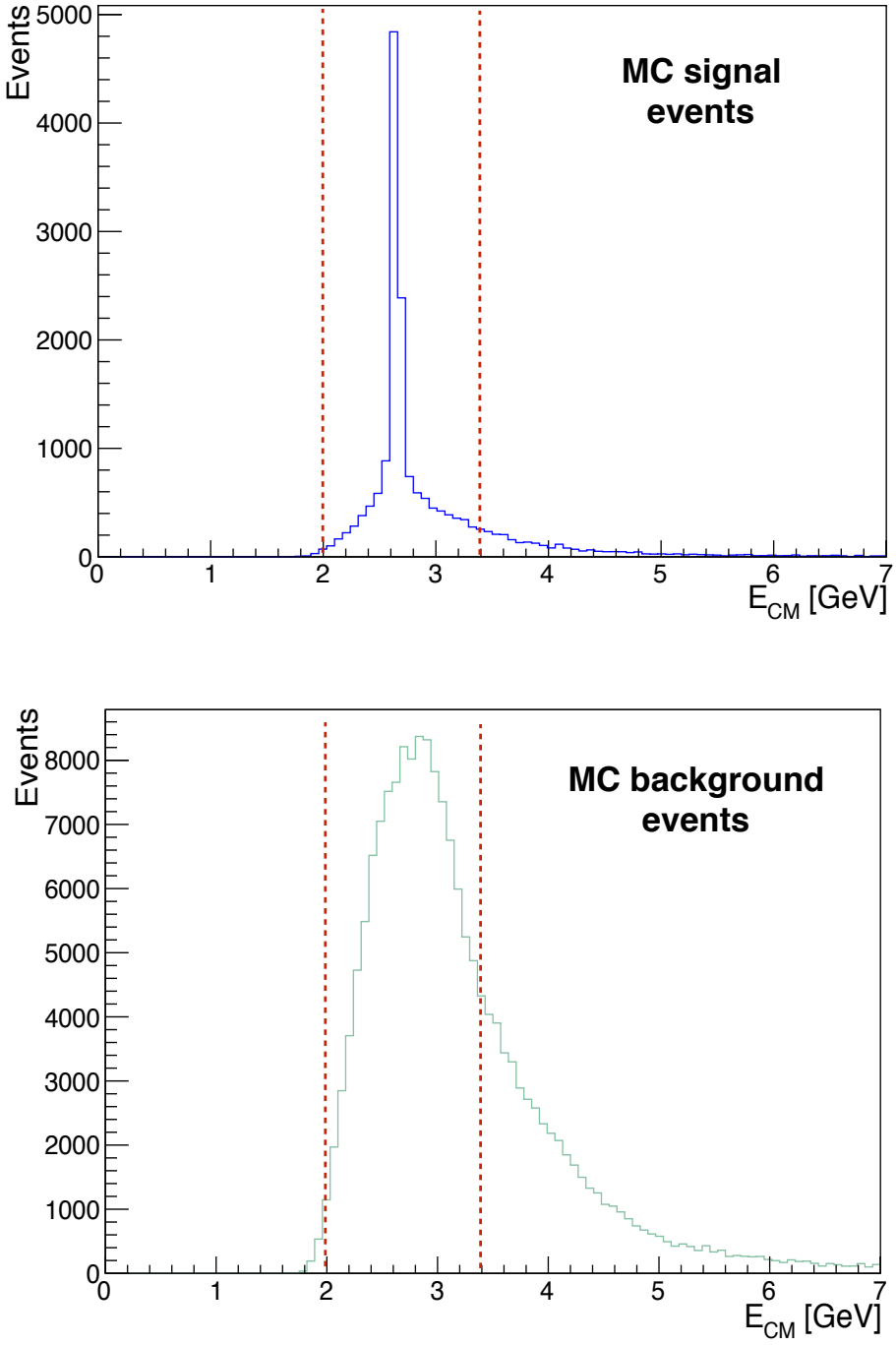

Figure 4.15: Center-of-mass energy distributions of Λ_c candidates from the signal data set (blue), and the background data set (green). The chosen cut is indicated by the area between the two dashed lines.

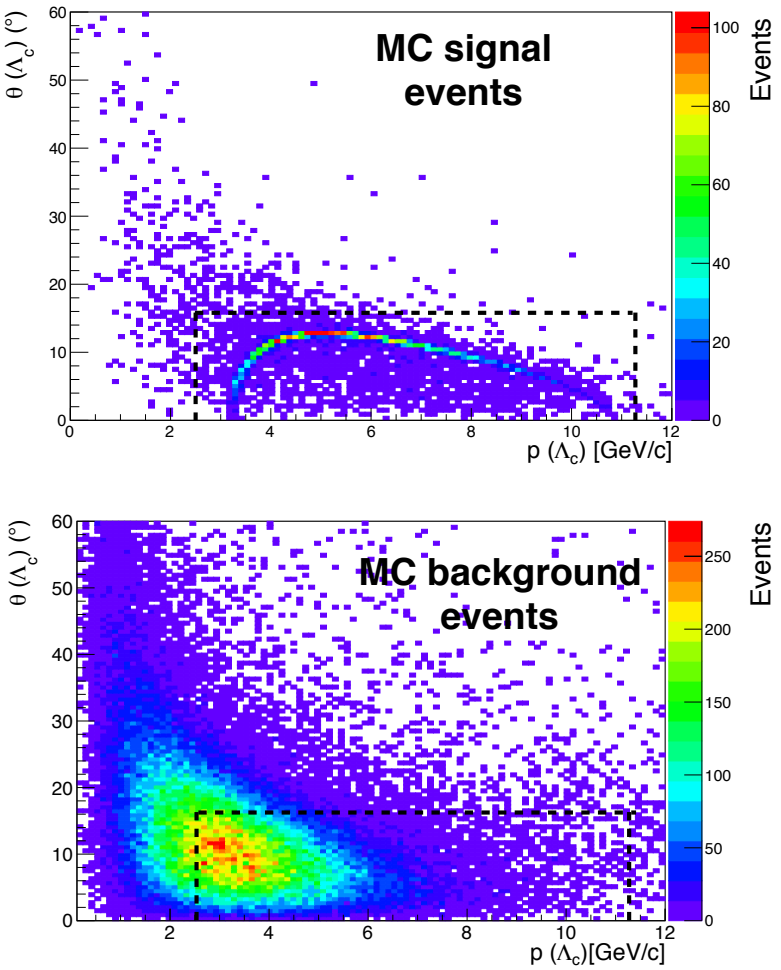

Figure 4.16: Correlation between the momentum and the angular distribution of Λ_c candidates for the signal events (top) and background events (bottom), by indicating the cut region.

4.6.1 Effects of event selection

The results of the previously described cuts and their impact on the recoil-mass distributions of the Λ_c candidates for both inclusive and exclusive reconstruction methods, for signal and background events, are presented in this section.

Inclusive Analysis

One method in our analysis is the reconstruction of only single Λ_c baryons. A Λ_c can be assembled, if at least one proton, one K^- and one π^+reconstructed. A mass constraint fit is applied to those events coming from the Λ_c baryons. The PndKinFitter class of PandaRoot is used to fit the four-vectors of the Λ_c candidate to the nominal mass of $m_{\Lambda_c} = 2.286$ GeV/c^2. The mass fit constrains the invariant mass of the candidate to the nominal Λ_c. Fig. 4.17 shows the probability distributions for both signal and background events. A cut on the probability function is applied for both signal and background and optimized for maximum signal to background ratio. The red dashed line in Fig. 4.17 indicates the applied cut. We only accepted the Λ_c candidates with $cut_{massfit}$ = $Prob(\chi^2) > 0.04$, and the candidates with a probability value below the cut are excluded from the analysis. Fig. 4.18 and Fig. 4.19 represent the recoil mass distributions of the $p^+K^-\pi^+$, for the inclusive reconstruction and for the signal and background events, respectively. The effects of the kinematic and mass cuts on the signal and background events can be clearly seen in these figures.

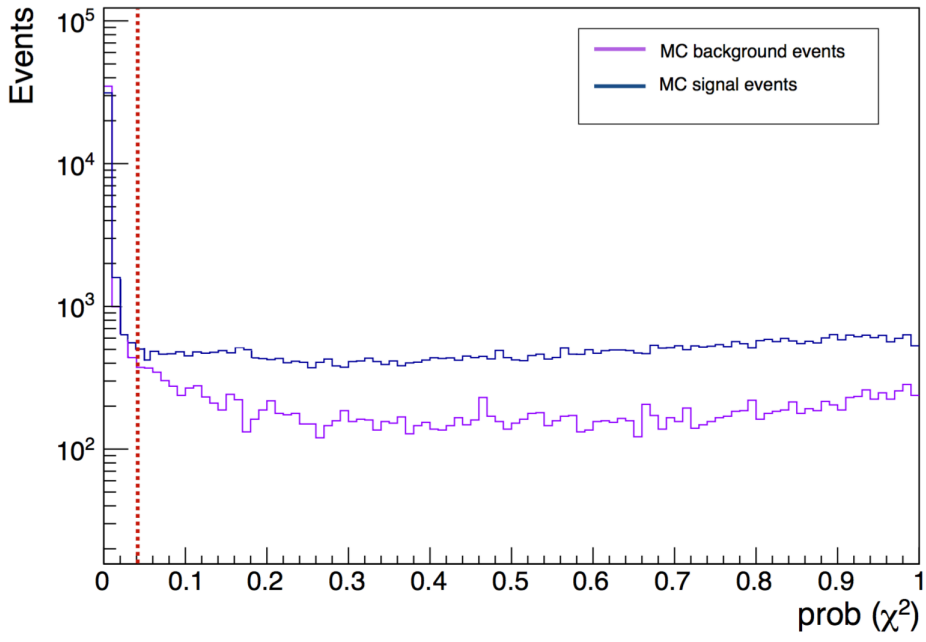

Figure 4.17: Probability distribution of the mass constraint fit applied to the mass of the Λ_c for signal events (blue) and background events (violet). The red dashed line indicates the cut applied.

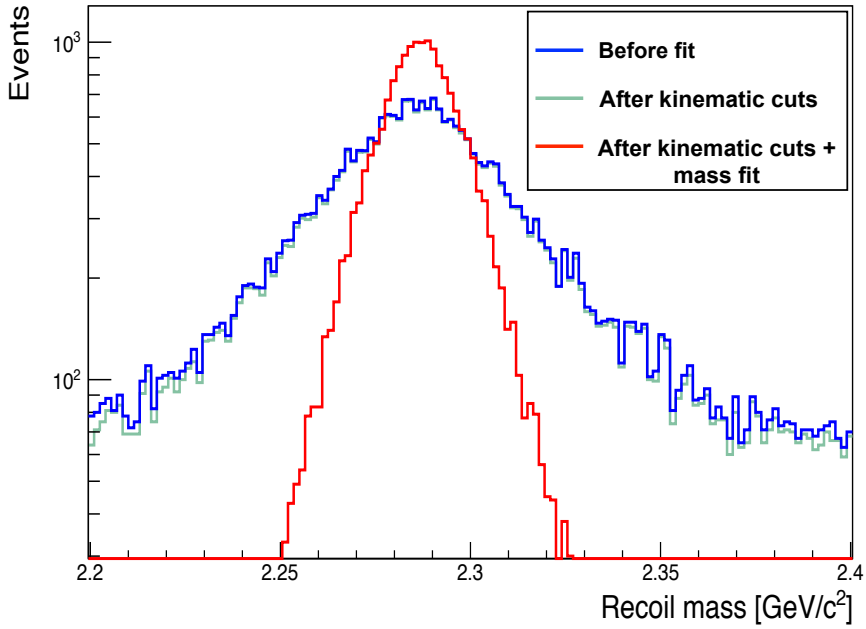

Figure 4.18: Reconstructed recoil mass of the $p^+K^-\pi^+$ system for the signal events for the inclusive analysis. The effects of the kinematic and mass constraint fits are indicated.

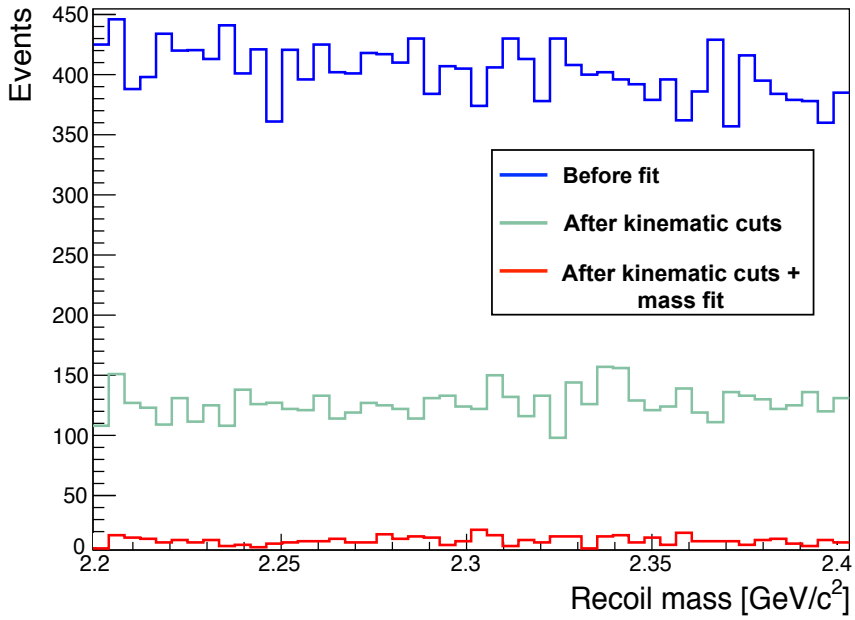

Figure 4.19: Reconstructed recoil mass of the $p^+K^-\pi^+$ system for the background events for the inclusive analysis. The effects of the kinematic and mass constraint fits are indicated.

Exclusive Analysis

Reconstruction of the total four-momentum of the $\Lambda_c\bar{\Lambda}_c$ system, the case in which all the final-state particles of both charmed hyperons are measured, is referred to as the exclusive analysis. The Pnd4CFitter class of PandaRoot is used to apply a four-constraint fit, modifying the four momenta in the Λ_c $\bar{\Lambda}_c$ system to conserve energy and momentum of the initial $p\bar{p}$ system.

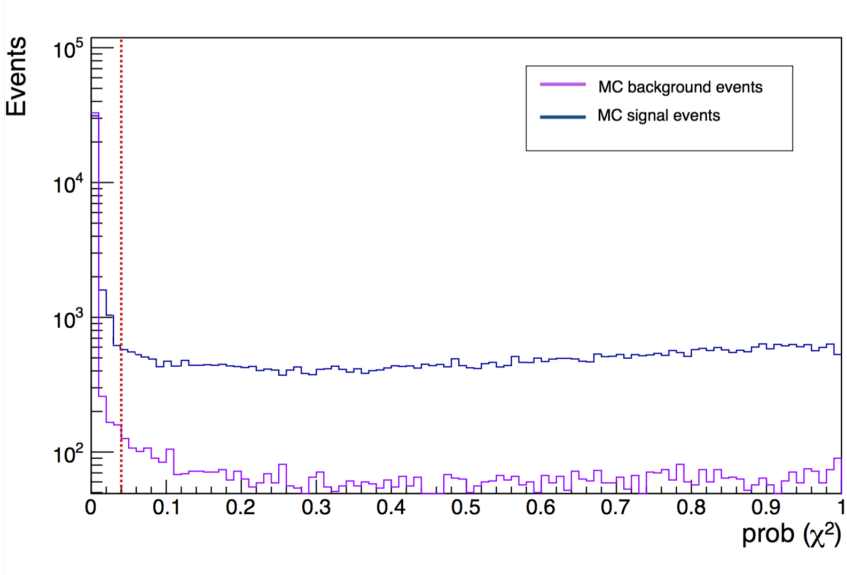

Figure 4.20: Probability distribution of the 4C fit applied to the mass of the Λ_c for signal events (blue) and background events (violet). The red dashed line indicates the cut applied. The red dashed arrow indicates the cut applied.

Fig. 4.20 shows the probability distributions for both signal and background events. A cut on the probability function is applied for both signal and background to remove events for which the fit quality was very poor. The cut is optimized to maximize signal to background ratio. The red dashed line in Fig. 4.20 indicates the applied cut. We only accepted the candidates with $cut_{4Cfit} = Prob(\chi^2) > 0.04$, and the candidates with a probability value below the cut are excluded from the analysis. The effect of the previous kinematic cuts and the 4C fit on the recoil mass distributions of the Λ_c baryons is presented here. Fig. 4.21 and Fig. 4.22 present the recoil mass distributions of the $p^+K^-\pi^+$, for the inclusive reconstruction, for the signal and background events, respectively.

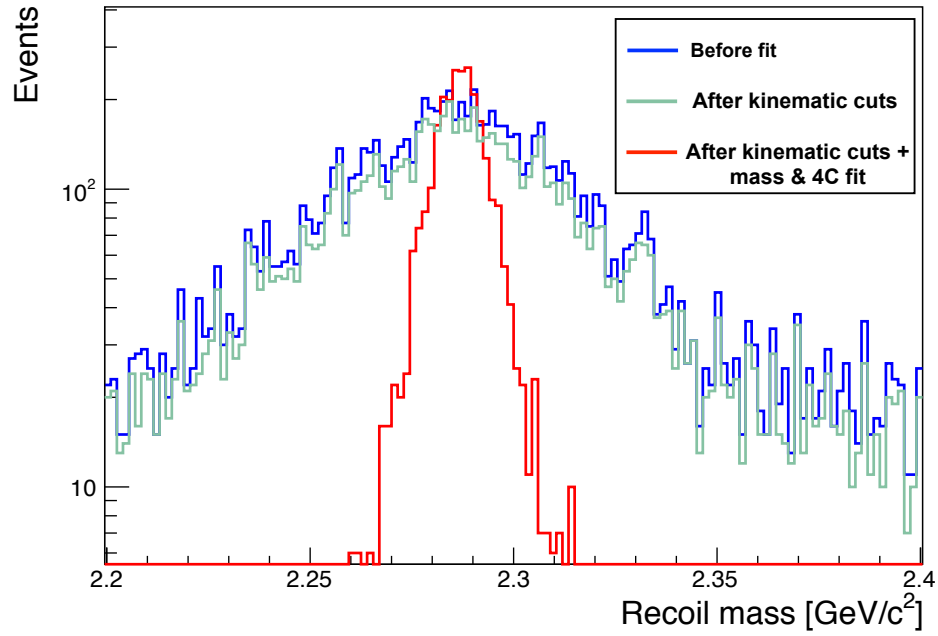

Figure 4.21: Reconstructed recoil mass of the $p^+K^-\pi^+$ system for the signal events for the exclusive analysis. The effects of the kinematic and mass constraint fits are indicated.

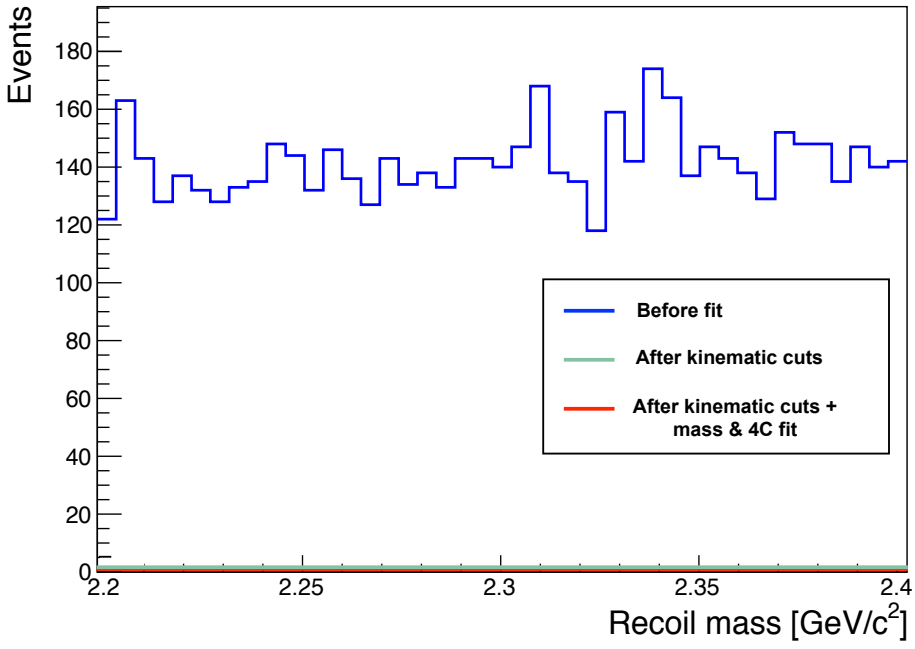

Figure 4.22: Reconstructed recoil mass of the $p^+K^-\pi^+$ system for the background events for the exclusive analysis. The effects of the kinematic and mass constraint fits are indicated.

Table 4.5: Overview of the reconstruction efficiencies and resolutions in different stages of the analysis, before and after fits and kinematic cuts, for Λ_c and $\bar{\Lambda}_c$ candidates. The resolutions of mass (σ_m), and momentum (σ_p), are taken from Gauss fits to the distributions.

	Λ_c			$\bar{\Lambda}_c$		
	N %	σ_p [MeV/c]	σ_m [MeV/c^2]	N %	σ_p [MeV/c]	σ_m [MeV/c^2]
Inclusive Analysis						
Before fit	17.9	68.4	37.5	17.8	68.5	37.5
After kinematic cuts	17.1	68.0	37.1	17.2	68.0	37.2
After kinematic cuts +mass fit	14.3	44.0	15.8	14.2	44.1	15.8
Exclusive Analysis						
Before cuts	5.6	48.2	14.5	5.5	48.3	14.6
After kinematic cuts	5.2	47.8	13.9	5.2	47.8	13.9
After kinematic cuts+4C fit	4.5	19.6	6.8	4.4	19.7	6.9

For the inclusive reconstruction, for a mass range of $\pm 3\sigma$ of the mass resolution obtained, of the 2.243×10^7 simulated DPM background-like events, 84 contain Λ_c candidates, passing the mass fit cut and all kinematics cuts. This means that the background is suppressed by a factor of 3×10^5 for the inclusive reconstruction. For the exclusive reconstruction, after applying all cuts which are the combinations of kinematics cut, mass and 4C fits, no events survived. Here, more DPM background data are needed to make statistically sustainable statements. This is very challenging, as already the produced 22 million events can be realized only with very high computational and storage efforts. One can conclude that suppression factor for the exclusive reconstruction is at least 2.2×10^7. The momentum and mass resolutions for both inclusive and exclusive reconstructions, together with the percentages of events passing the different cuts, are summarized in Table 4.5.

To study the sensitivity for $\bar{\text{P}}$ANDA to measure certain cross sections for our decay channel, the statistical significance is calculated, by using the Eq. 4.1. For the calculation of the FOM, a measurement of 30 days is assumed with varying luminosities in the range of the designed luminosities for $\bar{\text{P}}$ANDA (2×10^{30} to 2×10^{32} cm^{-2} s^{-1}). In this formula the Bf which is the branching fraction of the analysis decay is calculated differently, for inclusive and exclusive reconstruction. The branching fraction of the studied decay channel is $Bf_{\Lambda_c \to p^+K^-\pi^+} = (6.35 \pm 0.33)\%$ [8]. For the inclusive analysis, Bf is $2 \times 6.35\%$

and for the exclusive analysis, Bf equals 6.35% $\times$ 6.35%. Fig. 4.23 shows the results obtained for the FOM. We have taken a cross section of $\sim$15 nb as a guidance in this study. For the luminosity corresponding to phase-one of $\bar{\text{P}}$ANDA, we will be able to achieve a 5σ statistical significance in the inclusive reconstruction case. The chosen cross section value is not unreasonable since it is in the range of what theoretical models predict (see section 4.2). For the exclusive reconstruction, the blue line in Fig. 4.23, represents as a lower limit therefore, we are not able to make any hard conclusions on the sensitivity in the case of the exclusive reconstruction.

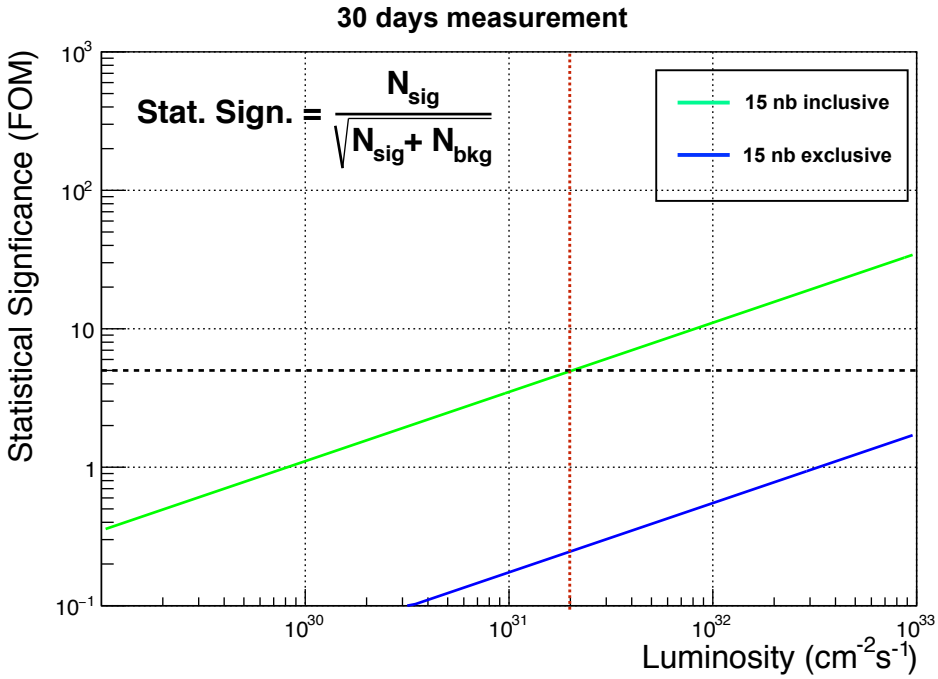

Figure 4.23: The calculated statistical significance (FOM) for the inclusive and exclusive reconstructions. The data taking time is 30 days. The horizontal black dashed line indicates the statistical significance of *sigma* and the red dashed line indicates the phase-one luminosity of $\bar{\text{P}}$ANDA.

4.7 Summary and Discussion

In this chapter, the MC simulation of the decay channel $p\bar{p} \rightarrow \Lambda_c\bar{\Lambda}_c \rightarrow p^+K^-\pi^+\bar{p}K^+\pi^-$ was investigated extensively. For the reconstruction, the realistic track reconstruction algorithms are used which reconstruct the PID

information from the following detectors, which are MVD, STT, EMC, DISK, DIRC, RICH and TOF. First, the particles of the final state were analyzed. The multiplicities of hits from protons, antiprotons, kaons and pions in two tracking sub-detectors, namely, MVD and STT was studied in section 4.4, in order to show the event topology and detector performance.

Moreover, the event reconstruction was studied by reconstruction of the final-state particles, followed by performing both inclusive (single Λ_c baryon reconstruction) and exclusive analysis (Λ_c baryon pair reconstruction). Finally, the physics background is benchmarked in section 4.6. The background of the beam momentum was studied using the DPM generator. For optimal background suppression, kinematic cuts and mass fits are applied. The final results of the efficiencies, momentum and mass resolutions in different stages of the analysis; before and after mass fits and kinematic cuts, for Λ_c and $\bar{\Lambda}_c$ candidates are presented in Table 4.5. For the inclusive reconstruction, we obtained a missing-mass resolution of 15.8 MeV/c^2 with a reconstruction efficiency of 14.3%. For the exclusive method, the invariant-mass resolution improves and a value of 6.8 MeV/c^2 has been obtained with a reduction in efficiency of 4.5%. The efficiencies were smaller than naively expected. The reason for this has been traced back to the performance of the PID algorithm. We expect that there is still room for improvement by optimizing the PID framework in PandaRoot, which is outside the scope of this thesis.

The feasibility to measure the Λ_c baryon pairs production with $\bar{\text{P}}$ANDA and to reveal the capability of $\bar{\text{P}}$ANDA to detect the Λ_c baryons and to separate the signal and background events, is the goal of this study. In order to make a strong statement about the production of the Λ_c baryon pair, an evaluation is obtained by the Figure of Merit (FOM). For the inclusive reconstruction, the minimum signal cross section that would detectable with the 5σ statistical significance for the phase-one luminosity of $\bar{\text{P}}$ANDA is 15 nb. For the exclusive mode, the background suppression factor is much higher and more DPM background data are needed, to make statistically sustainable statements. Only an upper limit on the sensitivity is obtained.

The contribution of the STT detector to particle identification was also studied. For our studied channel, the STT has a small contribution to the particle identification, because many particles have high momenta. The STT has good separation power for low momentum particle (< 1 GeV/c) for protons, kaons and pions. In contrast, the DIRC detectors are the most effective PID detectors for the channel of interest. The STT will play an important role in the particle identification for decay channels, in which the daughter particles are in the low momentum region (< 1 GeV/c).

Chapter 5

In-Beam Test Measurements with the STT Prototype at COSY

The Straw Tube Tracker (STT) is the main tracking detector for charged particles and it is part of the $\bar{\text{P}}$ANDA target spectrometer. For a detailed description of the $\bar{\text{P}}$ANDA STT, see section 3.3. The tasks of the STT are to determine the momenta of charged particles, via a precise spatial reconstruction of particle tracks in combination with a solenoid magnetic field, and to perform particle identification (PID) by a measurement of the specific energy loss (dE/dx). The PID information of the STT is necessary to separate protons, kaons and pions in the momentum region below 1 GeV/c. The development of the electronic readout of the STT is guided by optimizing its spatial and energy resolutions. Two electronic readout systems have been proposed for STT, a system based on **F**lash **A**nalog to **D**igital **C**onverters (FADC) and one based on **A**pplication **S**pecific **I**ntegrated **C**ircuit (ASIC) [130]. Since the $\bar{\text{P}}$ANDA detector is still under construction, the tracking performance of the straw tube detector is studied with data taken with proton and deuteron beams provided by the COSY accelerator (see section 5.2). This chapter focuses on the beam test of the STT prototype with the FADC read out and it describes the analysis of the data from measurements with proton and deuteron beams. The data were obtained at the COSY accelerator in Jülich Research Center, Germany.

5.1 Working Principle of a Straw Tube

The $\bar{\text{P}}$ANDA straw tube tracker has been described in chapter 3. This section presents a brief physics description, that governs the functioning of straw tubes. Straw tubes are gas-filled cylindrical tubes, with a conductive inner layer and a wire stretched along the tube axis. The operation of a gas-filled detector is based on the ionization of gas atoms or molecules by radiation, followed by collecting of the ion pairs as charge or current with the application of a voltage between two electrodes. The measured charge or current is proportional to the applied voltage and the amount of the energy of radiation, and it depends on the type and pressure of the gas. By applying an electric field between the wire and the tube, the electrons and ions drift through the gas. The wire is usually on positive voltage of about a few kV and collects the electrons, while the ions drift toward the tube wall as the cathode. The strength of the electric field near the thin wires, with a diameter of a few tens of μm, is high enough to produce secondary ionization. This process is called avalanche gas amplification. Due to the avalanche amplification, the charge collecting on the anode can be several orders of magnitude higher than the initial primary ionization. The amplifications depend on the high voltage and the gas characteristics. Typical amplifications of the primary charge is about 10^4 - 10^5, which is large enough to be recorded by the readout electronics [131, 132, 133]. Charged particles that traverse the straw tubes are tracked by measuring the drift time information of the ionization electrons to the anode wire. By measuring the drift time of earliest arriving electrons, one obtains the information that can be related to the minimum particle track distance from the wire. The corresponding isochrone contains all space points belonging to the same electron drift time and describes a cylinder around the wire axis. The particle track is reconstructed by a best fit to the isochrones measured in a series of several straw tubes with the same orientation. For a full stereo view of the particle trajectory additional skewed straws will be used.

5.2 Experimental Setup at COSY

The test setup consists of 128 $\bar{\text{P}}$ANDA type straw tubes which are arranged in eight layers of 16 straws each (see Fig. 5.1 and Fig. 5.3(a)). The tubes, with an aluminized Mylar wall of 27 μm thickness, are 140 cm long and have an inner diameter of 10 mm. Two scintillators are placed in front and after the STT setup in the proton and deuteron beams, are used to trigger on a coincident event and start the data acquisition. In addition, a drift chamber and a hybrid drift chamber with a GEM amplification stage were included for the beam diagnostics. A sketch of the setup is shown in Fig. 5.2.

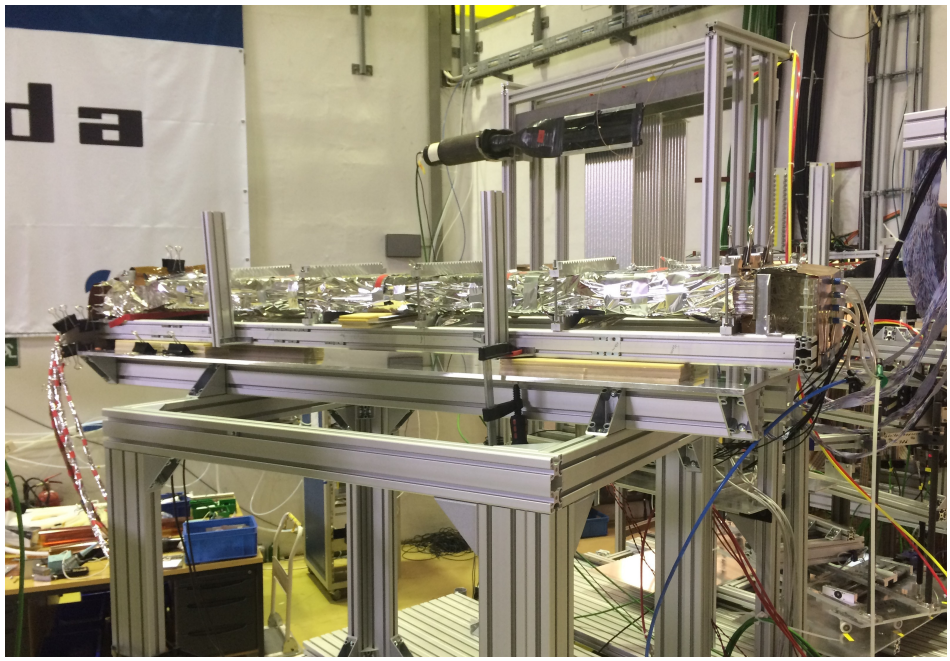

Figure 5.1: Straw tube prototype used at the COSY-TOF area. The straw tube prototype are connected to the preamplifiers with coaxial high voltage cables and Flash ADCs.

The electronic readout of the straw signals consists of the trans-resistance amplifers and FADCs. The FADCs sample the analog signal amplitude with a frequency of 240 MHz. FPGAs (**F**ield **P**rogrammable **G**ate **A**rray) control the readout of an FADC module and are programmed to record single spectra. The configuration of the straw prototype detector during the tests with the proton or deuteron beams is sketched in Fig. 5.3. The straw tubes are directly connected by 12 m coaxial high voltage cables to the electronics placed outside of the detector prototype, in the experimental area. The raw signals from the straw tubes are transmitted via cables to remotely placed analog and digital electronics which will give enormous advantages in future, for the topology of the whole detector system (the $\bar{\text{P}}$ANDA STT). The space reserved for electronics inside $\bar{\text{P}}$ANDA is only about 15 cm along the axis of the STT. Electronics attached directly to the STT are required to have very little heat dissipation and it must be radiation hard because of high luminosity of $\bar{\text{P}}$ANDA and the short distance from the interaction point. Placing electronics outside the detector solves radiation hardness and heat problems. Since space near the STT is then needed only for connectors and cables, these can be conveniently accommodated. The approach of connecting straw tubes with electronics placed

several meters away was already successfully used in the WASA detector at COSY Jülich [135]. During the measurements the prototype detector was oriented perpendicular to the beam axis to have the protons or deuterons impinging at 90° with respect to the straw axis. In vertical direction the straw tracker was positioned allowing the beam to pass parallel to the layer structure or with an angle of 5° in order to increase the number of crossed straw tubes (see Fig. 5.3(b)). All these measurements were done with the beam hitting the straw in the middle region along the tubes.

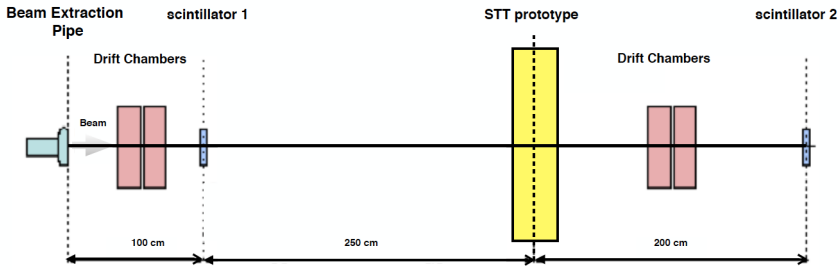

Figure 5.2: Schematic of the setup used at the COSY. The beam enters from the left.

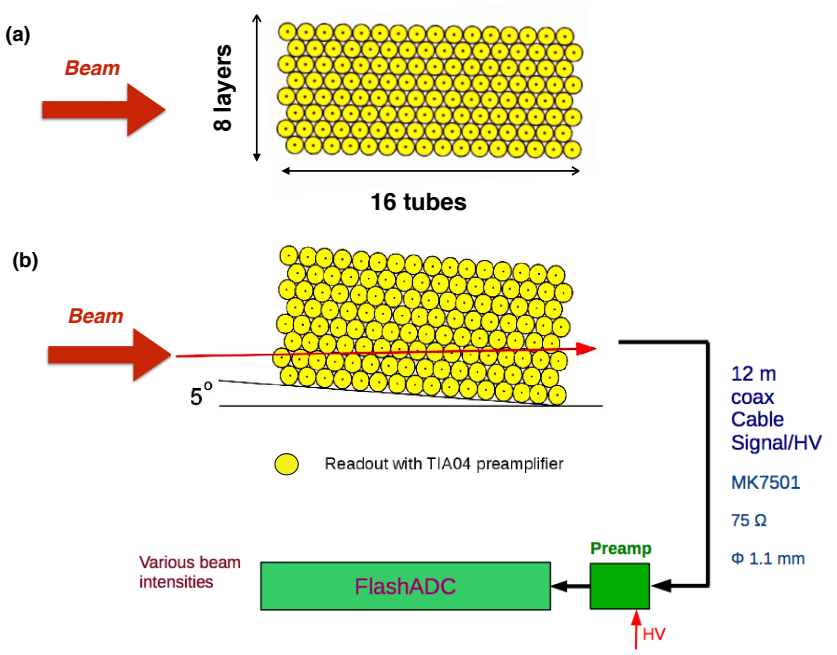

Figure 5.3: (a) Schematic side view of the STT prototype. (b) Configuration of STT prototype detector during the tests with the proton or deuteron beams: the beam enters from the left. The prototype is rotated by 5°. The STT prototype are connected to the preamplifiers with 12 meters coaxial high voltage cables and FADCs. The red arrows indicate the beam direction. The beam enters from the left and exits from the right. A part of the figure is taken from [134].

5.2.1 Test Beam Conditions

The COSY accelerator facility is a **CO**oler **SY**nchrotron and storage ring located at the Jülich Research Center in Germany. COSY delivers high precision beams with up to 3×10^{10} protons and covers the momentum range from 300 MeV/c to upper limit of 3000 MeV/c for the external target locations such as COSY-TOF and 3300 MeV/c for the three internal experiments ANKE, PAX and WASA-at-COSY; see Fig. 5.4. All detection systems are operated by large international collaborations. COSY can accelerate both unpolarized and polarized proton and deuteron beams.

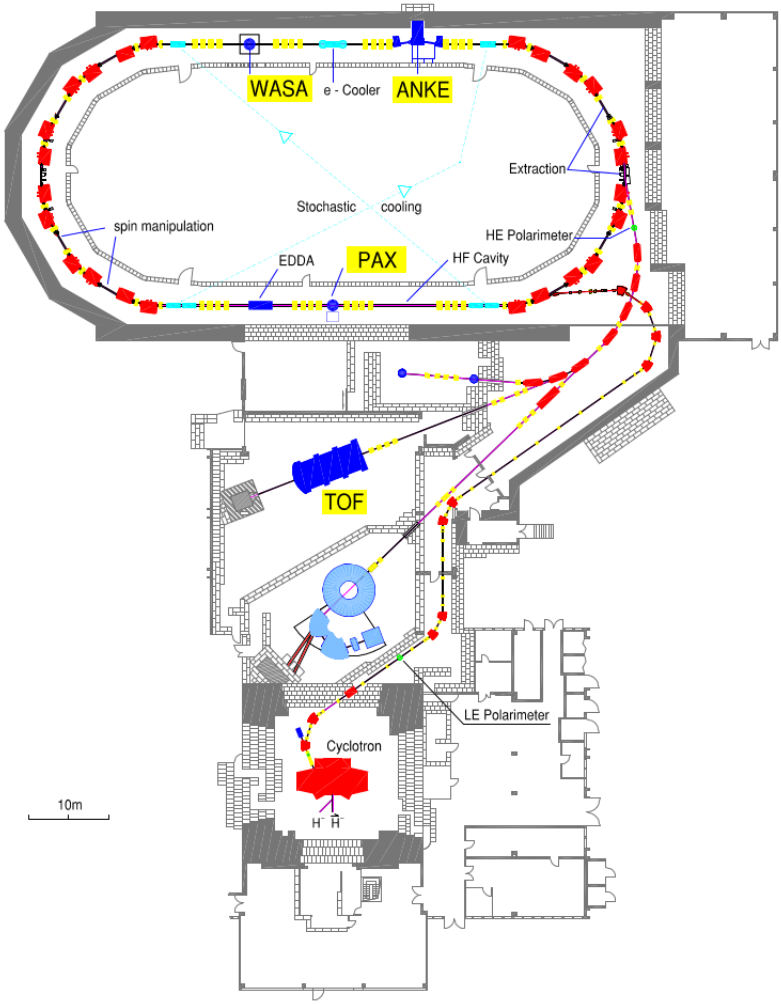

Figure 5.4: Layout of the COSY and beam areas [136, 137]. For the STT prototype beam test, the TOF detector is replaced by the STT prototype setup.

The beam particles are pre-accelerated by the Jülich Light Ion Cyclotron (JULIC) and transported to COSY. It has been conceived to deliver high precision beams for hadron physics experiments, e.g. WASA and TOF; with either circulating beam or extracted beam. Beam extraction is accomplished by the conventional resonant extraction mechanism as well as with the stochastic extraction method. Proton and deutron beams are delivered routinely to three internal and three external experimental areas [136, 137]. The STT prototype test was carried out with an external beam from COSY. In this test, the proton and deuteron beams in the momentum range 0.50 GeV/c to 2.95 GeV/c were used. Fig. 5.4 shows the layout of the COSY and the beam areas. In April 2016, the first test was carried out in the COSY-TOF beam area. A proton beam with four different momenta (0.550 GeV/c, 0.750 GeV/c 1.00 GeV/c and 2.95 GeV/c) was used. Fig. 5.1 shows the straw tube prototype setup in the beam area. In November 2016, the second test was carried out in the beam area with a deuteron beam with three different momenta (0.60 GeV/c, 0.75 GeV/c and 1.5 GeV/c). In both tests, several data runs were taken for each momentum and for a wide range of operational settings such high voltages and intensities.

5.3 Event Samples

The Straw Tube Tracker of the $\bar{\text{P}}$ANDA experiment will be operated by using a 90:10 mixture of (Ar + CO_2), at an over-pressure of 1 bar, and with a high voltage of 1.8 kV. The data sets that were obtained with the prototype were obtained using the same gas conditions, but at three different high voltages, namely (1.75 kV, 1.80 kV and 1.85 kV). The different high voltages have been chosen to be 0.05 kV below and above the $\bar{\text{P}}$ANDA working high voltage (1.8 kV) to observe the difference in resolution for the lower and higher voltages. One important task of the STT is to do precise spatial reconstruction of charged particles in a broad momentum range and the measurement of the specific energy loss (dE/dx) for particle identification. To achieve this goal the tests were performed with proton and deuteron beams with different momenta, in a wide momentum range of 0.5 GeV/c to 2.95 GeV/c. The data have been mainly recorded in equal data samples. The results will be presented in detail, for data collected at 1.8 kV; then, they will be compared with the results obtained at 1.75 kV and 1.85 kV.

5.4 Data Analysis

5.4.1 Feature Extraction from Signal Shapes

The signals are sampled and recorded with the 240 MHz FADCs. An example of a recorded signal is shown in Fig. 5.5. Using sampling FADCs gives full control over all relevant features of the tracking detector. Raw sampled signals can be monitored online so that the status of each straw tube including the whole electronics chain is visible at any time. The data from the prototype measurements were recorded in the raw mode in order to have full freedom for the off-line application of the analysis tools. The implemented algorithms extract the time information from discriminators and information about position and shape of the found pulses. To reduce the influence of the varying start position and length of the signal, the so-called pulse search method was implemented using the complete signal shape information. The amplitude and the time information of the pulse minimum and maximum are extracted for each pulse which is found by the pulse search algorithm [141].

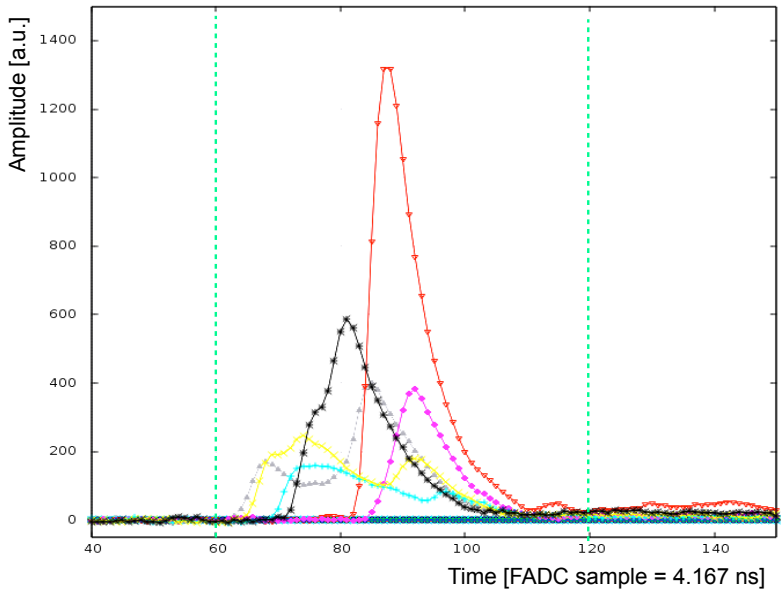

Figure 5.5: Analog signals from the straw tubes, obtained from one data file. The analog signals are recorded by the 240 MHz FADCs and range used to integrate the signals for the specific energy loss determination, the green dashed lines show the sampling integration range.

In this thesis, the implemented discriminator algorithm uses the Zero-Crossing (ZC) technique. In this case, as the first step, the time corresponding to half of

the signal maximum is found. Then the straight line which passes through the two sample points with the signal value above and below the half maximum is calculated. From this straight line, the linear extrapolation is made to find the time when the function corresponding to the straight line has the value of zero [141]. The ZC timings are available for all pulses and allow to discriminate pileup pulses exploiting these data. Another main task of the STT is to measure the specific energy-loss of the charged particles for the identification of the particle species. In particular, an efficient separation of pions, kaons and protons in the momentum region below 1 GeV/c is needed [134]. Charged particle identification with drift chambers of comparable size and channel numbers to the $\bar{\text{P}}$ANDA STT has been performed in experiments like BABAR [143], BESIII [144] and HADES [145], but it has not done for straws. The particle identification technique is based on specific energy loss (dE/dx), which requires the knowledge of the deposited energy and the path length. A resolution of about 10% of the energy deposited in a particle track is needed to realize the physics ambitions of $\bar{\text{P}}$ANDA [54]. The energy loss can be deduced from the integrated charge of the output signal or from any other other parameter which is linear or related through another known function to the collected charge. Two methods have been evaluated within the $\bar{\text{P}}$ANDA collaboration. In the first method, the area of the pulses from the FADC output is extracted and used as a measure of the energy loss. The second method, using the ASIC readout information, determines the time-over-threshold (TOT) of the signal providing a measure of the pulse width, and, thereby, of the energy loss [134]. This thesis is devoted to do the reconstruction of the pulse area with the FADC information.

5.4.2 Calibration Procedure

To do a precise track reconstruction, the STT has to be carefully calibrated. The calibration of the STT includes the determination of the position in space of the straw wires and the characteristic relation between the measured drift time and the isochrone radius. This section explains the calibration method.

Drift Time Spectra

The drift time information of the ionization electrons is stored in FADC channels. Fig. 5.7 shows an example of a measured time spectrum for an illuminated straw tube. This spectrum is obtained by extracting ZC of the pulses of each straw, converting its value to units of ns, and eventually fill this into a histogram as depicted in Fig. 5.7. In the analysis of the time distributions of individual straws, the minimum and the maximum drift times, t_0 and t_{max}, correspond to a track traversing the tube close to the wire and close to the

cathode wall, respectively.

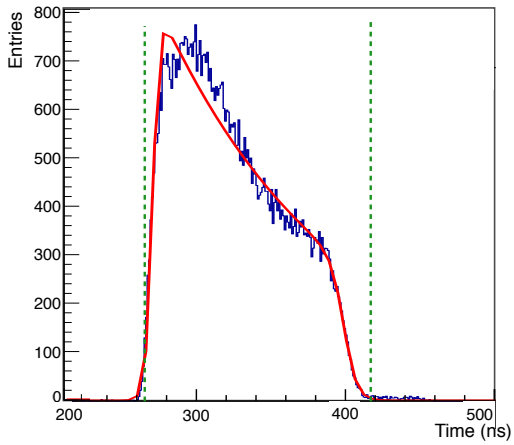

Figure 5.7: Example of a fitted time spectrum. The red line is the fit of the distribution; the green vertical lines correspond to the t_0 and t_{max} values determined by the fit.

For each tube, the parameters of the drift time distribution are derived from a fit performed with the following empirical function [138, 139]:

$$\frac{dn}{dt} = P_1 + \frac{P_2[1 + P_3\exp((P_5 - t)/P_4)]}{[1 + \exp((P_5 - t)/P_7)][1 + \exp((t - P_6)/P_8)]}. \tag{5.1}$$

where P_1 is the noise level, P_2 is a normalization factor, P_3 and P_4 are related to the central part of the distribution, respectively. P_5 and P_6 are the values of t_0 and t_{max}, respectively. P_7 and P_8 describe the slope of the leading and trailing edge of the distribution, respectively [134]. The red line in Fig. 5.7 shows the result of the fit. The value of t_0 depends on the high voltage setting and discriminator threshold. The drift time $\Delta t = t_{max}$ - t_0 depends only on the drift properties of the tubes. The time spectra of all tubes must be calibrated to have approximately the same shape and the same drift time, Δt. To achieve this goal the quality of the fit is checked and only the tubes which satisfy the following conditions, 262 ns $\leq t_0 \leq$ 270 ns and 420 ns $\leq t_{max} \leq$ 434 ns are considered. The distributions of the parameters of the fit which describe t_0 and t_{max} and noise level are shown in Fig. 5.8. After fitting the time spectra of each tube, we corrected for the offset t_0 and subtracted the noise level. Then, they are added into a sum spectrum, each in its Δt range. It is worth to mention that five broken channels are excluded for this analysis. Fig. 5.9 represents the hitmap of the straw tubes, obtained from the data taken with the 0.550 GeV/c

proton beam. The white rectangular boxes represent the broken channels. Fig. 5.10 shows the drift time spectrum of the straws, obtained from the data taken with the 0.550 GeV/c proton beam.

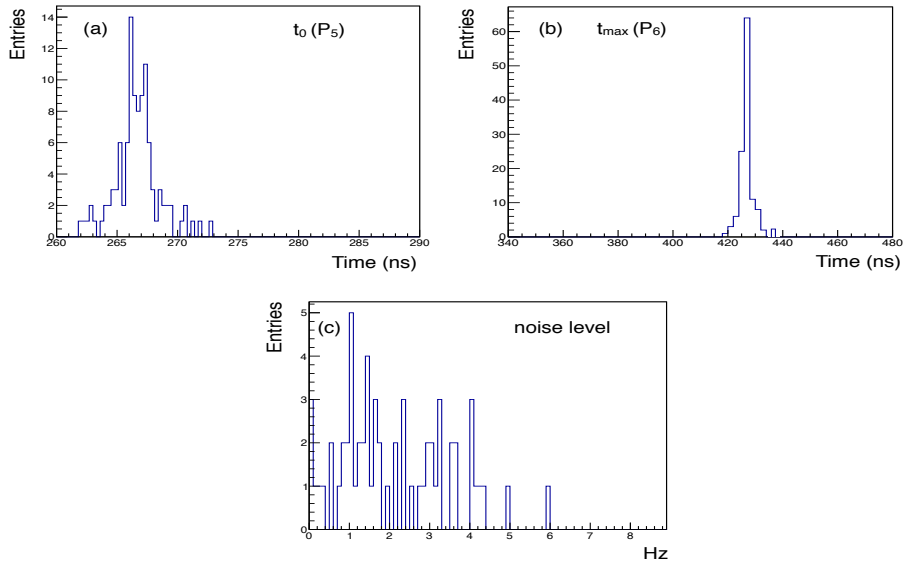

Figure 5.8: Parameters obtained from the fit of the drift time spectra: (a) $t_0 = P_5$, (b) $t_{max} = P_6$, (c) and P_1 which is the noise level.

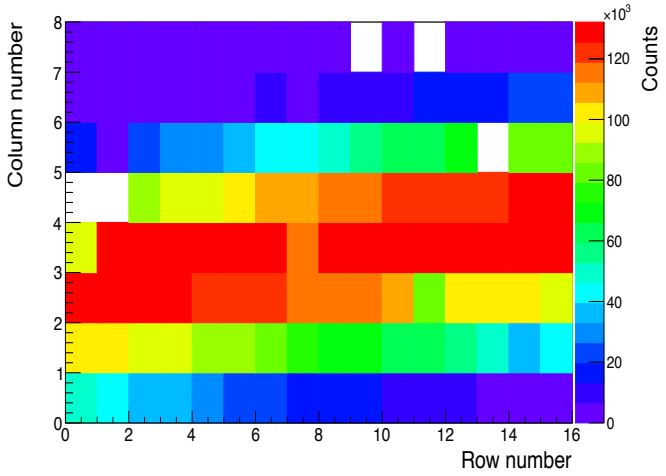

Figure 5.9: Hit map of one data file. Each rectangular box represents a tube. The white rectangular boxes represent the broken channels. The beam enters from the left and exits from the right.

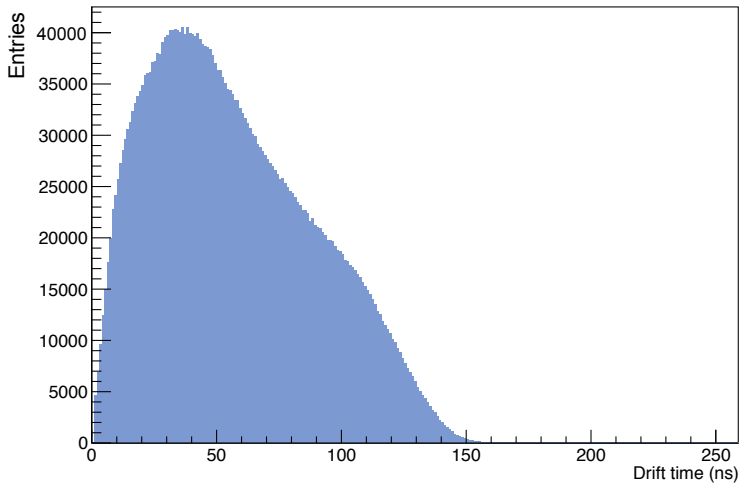

Figure 5.10: Drift time spectrum of the straws, obtained from the data taken with the 0.550 GeV/c proton beam.

After the calibration of the time, the next step is the extraction of the isochrone radius $r(t)$ from the drift time t. Under the hypothesis of a uniform illumination of the tube and a constant efficiency over the tube volume, the isochrone radius drift time relation ($r(t)$ relation) can be obtained by the following equation:

$$r(t) = \frac{R_{tube}}{N_{tot}} \int_0^t \frac{dn}{dt'} dt', \tag{5.2}$$

where n is the number of tracks, N_{tot} is the total number of tracks and R_{tube} the tube radius. The time resolution (bin size) is finite so that Eq. 5.2 becomes:

$$r(t_i) = \frac{\sum_{i=1}^{i_t} N_i}{N_{tot}} (R_{tube} - R_{wire}) + R_{aval}. \tag{5.3}$$

R_{wire} is the wire radius, N_{tot} is the sum of all bin entries N_i, and R_{aval} is the avalanche radius. R_{aval} is the radius of the avalanche circle, the area which is considered around the anode wire. In our analysis, this radius is considered to be in the order of 100 μm. The obtained spacetime relation $r(t)$ is shown in Fig. 5.11. An isochrone radius defines a circle of the smallest distance of a particle track to the straw wire. The isochrone contains all space points belonging to the same electron drift time and describes a cylinder around the wire axis. It has been parametrized using a polynomial of fifth-order. Once the spacetime relation is known, the isochrone radius of a given hit is calculated from the measured drift time.

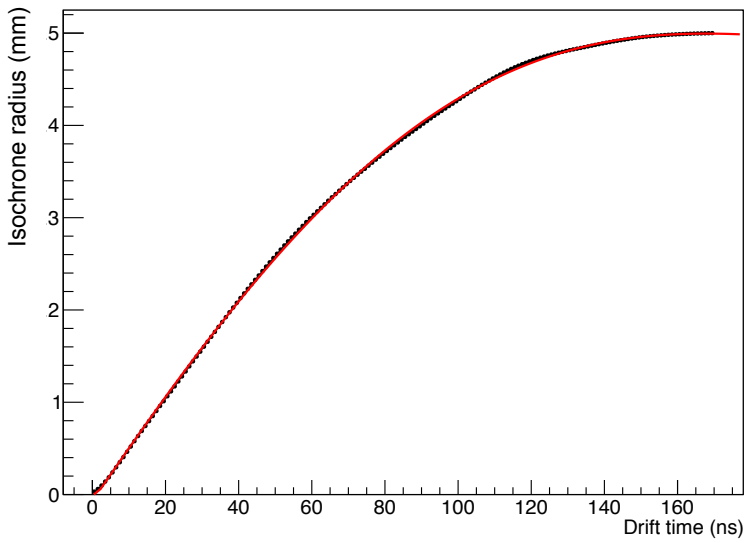

Figure 5.11: Isochrones radius-drift time relation (r(t)), obtained from the data taken with the 0.550 GeV/c proton beam. The red line indicates a 5^{th}-order polynomial that has been fit to the data to obtain the parameters of the $r(t)$ relation. A tube radius of 5 mm, wire radius of 20 μm and an avalanche radius of 100 μm were used.

5.5 Track Reconstruction

The STT provides the isochrone radius of the firing wires (the shortest distance to the wire of the particle traversing the tube). The tracking algorithm uses the hit information from the STT. Since the coordinates of the firing wires and the drift times are the only measured observable, the hit coordinates need to be extracted from this information, by performing a track-fitting procedure. This procedure is summarized following:

- The first step of the track reconstruction is a pre-fitting procedure. The pre-fit minimizes the perpendicular distance of the centers of the firing tubes from the best line fit [140]. After the pre-fit, the distances of each hit to the pre-fit line is calculated and if this distance is larger than 5 mm, the hit in the event is identified as noise and is rejected.
- The resolution that we obtain from the pre-fit is not optimum yet, and there is room for improvement by taking into account a proper weighting. To achieve this goal we applied a minimization procedure using TMinuit,

which is part of the ROOT framework [142]. TMinuit finds the minimum by the iteration procedure. The pre-fit parameters, the slope and intercept of a track together with the isochrone-radii information will be used for the initialization of the TMinuit minimizer.

- The new minimized track is fitted and if the distance between the new track and the calculated isochrone is larger than 1 mm, the hit is rejected and the fit is repeated without that spurious hit. Fig. 5.12 shows an schematic view of the fitting procedure, the red circles are the isochrones circles, the purple and the green lines represent the pre-fit and fit, respectively.

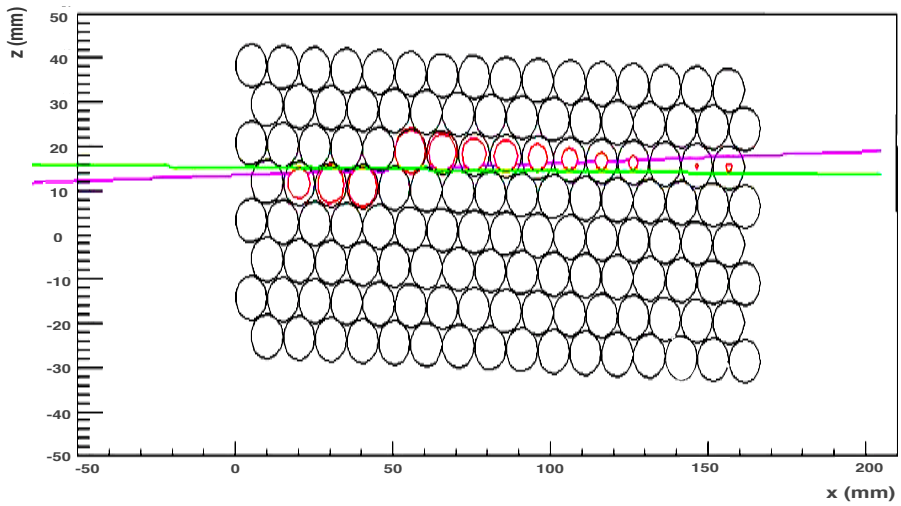

Figure 5.12: Schematic view of the fitting procedure, the purple and the green lines represent the pre-fit and fit, respectively. The red circles are the isochrone radii.

- With the new tracks (which passed the previous steps), the residuals (distance of the track to the calculated isochrone) for each hit is calculated and if this distance is larger than $\sim$ 3 times of the error of the isochrones, the hit is rejected. The error of the isochrones is calculated with the parameters derived from a six-order polynomial fit to the experimental data. And finally, the minimization function is applied for the last time to find the best track.

It is worth mentioning that the values of applied cuts are optimized to have an efficiency of at least 80%. The steps described above have to be repeated several times until the mean value of the residuals comes close to zero. To investigate the stability of the convergence of the method, the root mean square deviation is used as the figure of merit. Fig. 5.14 shows that it has converged

to the value of 16 μm. In all step of the analysis, tracks with at least 5 hits are considered for reconstruction. Since the prototype consists of eight layers with 16 tubes each, the maximum possible number of hits generated by a single track is 32, in the case of a horizontal track hitting all the tubes of two adjacent layers. Events with more than 32 hits have, therefore, been rejected. Fig. 5.13 shows the number of hits per track before and after applying cuts. The violet distribution shows the number of hits before reconstruction. It can be seen that a few events have a larger number of hits per track (>32) which indicates the presence of a second track. The $r(t)$ curve is used for the track reconstruction to find the most probable correlation between the drift time and the track-to-wire distance. After that, the track-to-wire distances are calculated for all hits of the track. Fig. 5.15 shows the distances of the track to the wire versus the measured drift times for the reconstructed tracks. The two arms of this figure are related to tracks that are either above or below the anode wire. The distance distribution shows an almost symmetric behavior above and below the anode wire, as expected. Fig. 5.16 shows the distribution of the residuals as a function of the drift time.

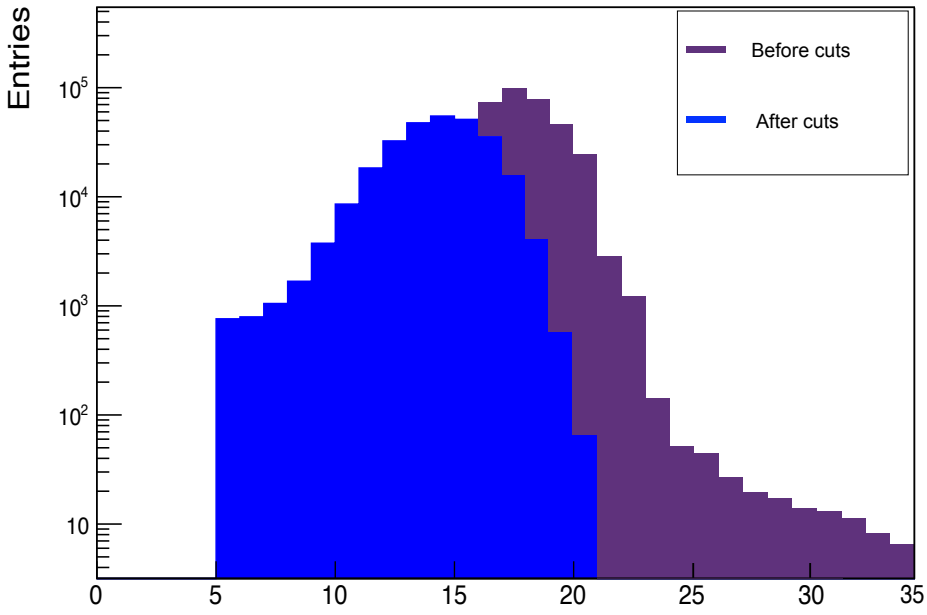

Figure 5.13: The number of hits per track before and after applying cuts. The violet distribution shows the number of hits before applying cuts. The violate spectrum shows the number of hits before applying cuts. A few events have a larger number of hits per track (32) which indicates the presence of a second track.

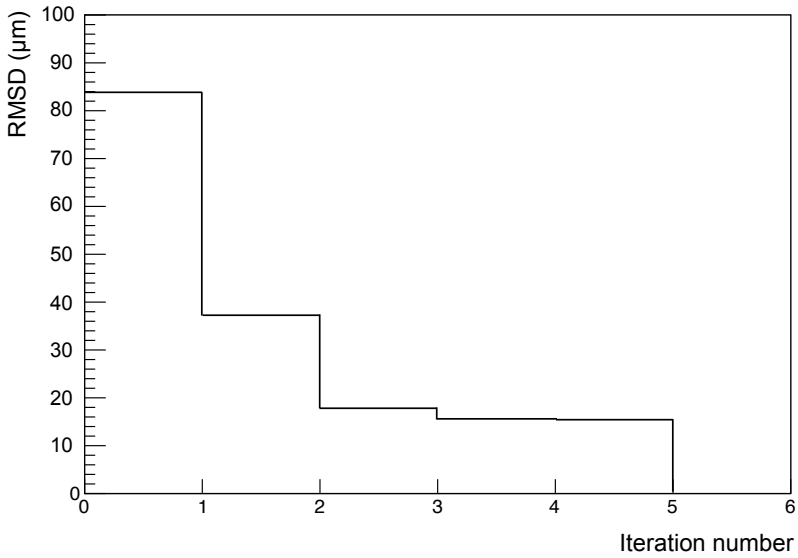

Figure 5.14: Root mean square deviation as a function of the iteration numbers.

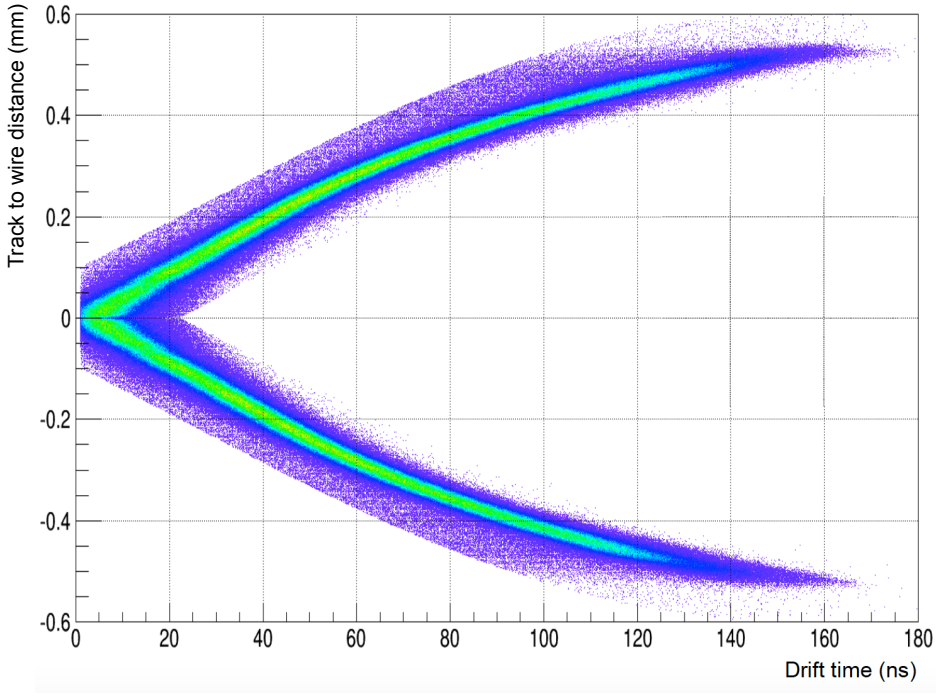

Figure 5.15: Track-to-wire distance vs. the measured drift time for reconstructed tracks obtained from data taken with the 0.550 GeV/c proton beam. The two arms of this figure are related to tracks placed above and below the anode wire.

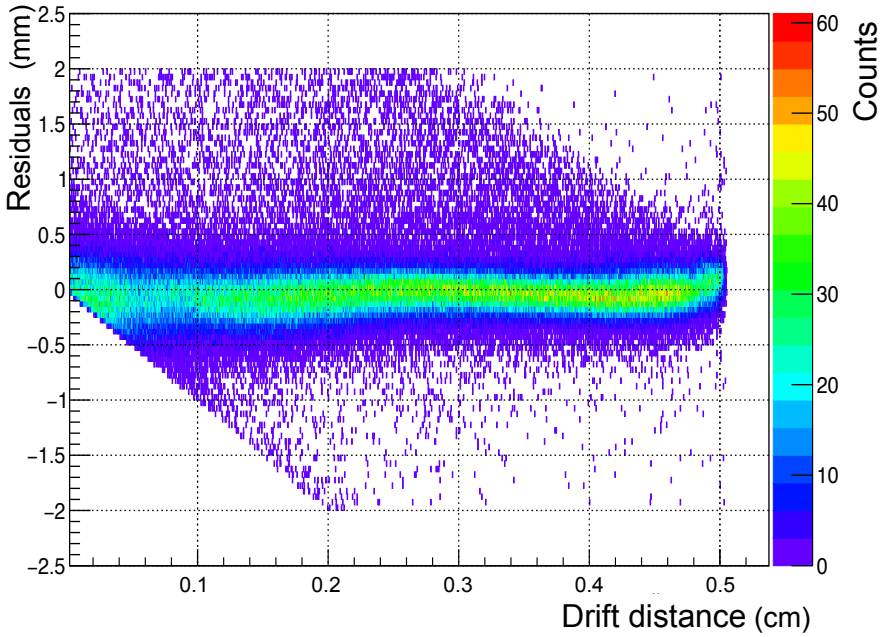

Figure 5.16: Residuals vs. drift distance, obtained from data taken with the 0.550 GeV/c proton beam.

5.6 Spatial Resolution

As explained in the previous sections, two beam tests were carried out at the COSY beam area (see Fig. 5.4). In the first test, proton beams with four different momenta (0.55 GeV/c, 0.75 GeV/c, 1.00 GeV/c and 2.95 GeV/c) were used, and the second test were carried out with deuteron beams with three different momenta (0.60 GeV/c, 0.75 GeV/c and 1.5 GeV/c). Fig. 5.2 and Fig. 5.3 show a view of the setup and the configuration of the straw prototype detector. In both tests, several data runs were taken for each momentum and for a range of operational settings such as high voltages and intensities. In addition to the $r(t)$ curve, which defines the most probable correlation between the drift time and the isochrone radius, the spatial resolution is another important parameter and must be determined. The spatial resolution of the STT is quantified by the width (σ) of the Gaussian function that was used in the fit to the residual distributions of the reconstructed tracks. The distribution of the residuals have obtained in the following way: the track-to-wire distance has divided into ten intervals of 0.5 mm each, from 0 to 5 mm. The standard deviation, σ, of each Gaussian fit is used as a measure for the spatial resolution. For

each interval, the residual distribution has been obtained and fit with a Gaussian function. Fig. 5.17(a) shows the cumulative residual spectrum obtained by integrating over the complete drift distance. The corresponding fit gives an overall spatial resolution of 146 μm. Fig. 5.17(b) depicts the resolution as a function of radial distance. The values of σ of each Gauss function that fits the peaks of the residual distributions has been used to derive the straw tube resolution shown in Fig. 5.17(a). The resolution is worse close to the wire than at the straw wall. This is due to the avalanche effects and high drift velocity close to the wire [133]. Close to the wire, the resolution is about 180 μm, and for larger distances to the wire, the resolution improves to about 100 μm close to the straw cathode, where the electron diffusion is a limiting factor during their drift to the anode.
For the first tests, we used four different proton beams with varying momenta. For the second series of measurements, deuteron beams were used with three different momenta. With these data sets, we could systematically study the momentum and particle-type dependence of the spatial resolutions under various parameter settings. All the steps of the data analysis presented in this section have been repeated also for the data sample collected while operating at three different high voltage settings for the proton and deuteron beams. Tables 5.6 and 5.7 summarizes the obtained spatial resolutions for proton and deuteron beams, respectively, as a function of beam momenta and high-voltage settings. The data are represented as well in Fig. 5.18. The achieved resolutions are between 146 μm to 171 μm for proton and 143 μm to 160 μm for deuteron beams. The results obtained for other high voltages are very similar to the results of 1800 V, which will be the working high voltage of $\bar{\text{P}}$ANDA STT for this gas mixture. In the case of 1850 V, the resolution is better by about 6-8 μm compared to the case of 1800 V. Increasing the high voltage by 50 V, leads to about a 5% improvement in the spatial resolutions. The goal was to check how spatial resolution depends on the high voltage applied to the detector.

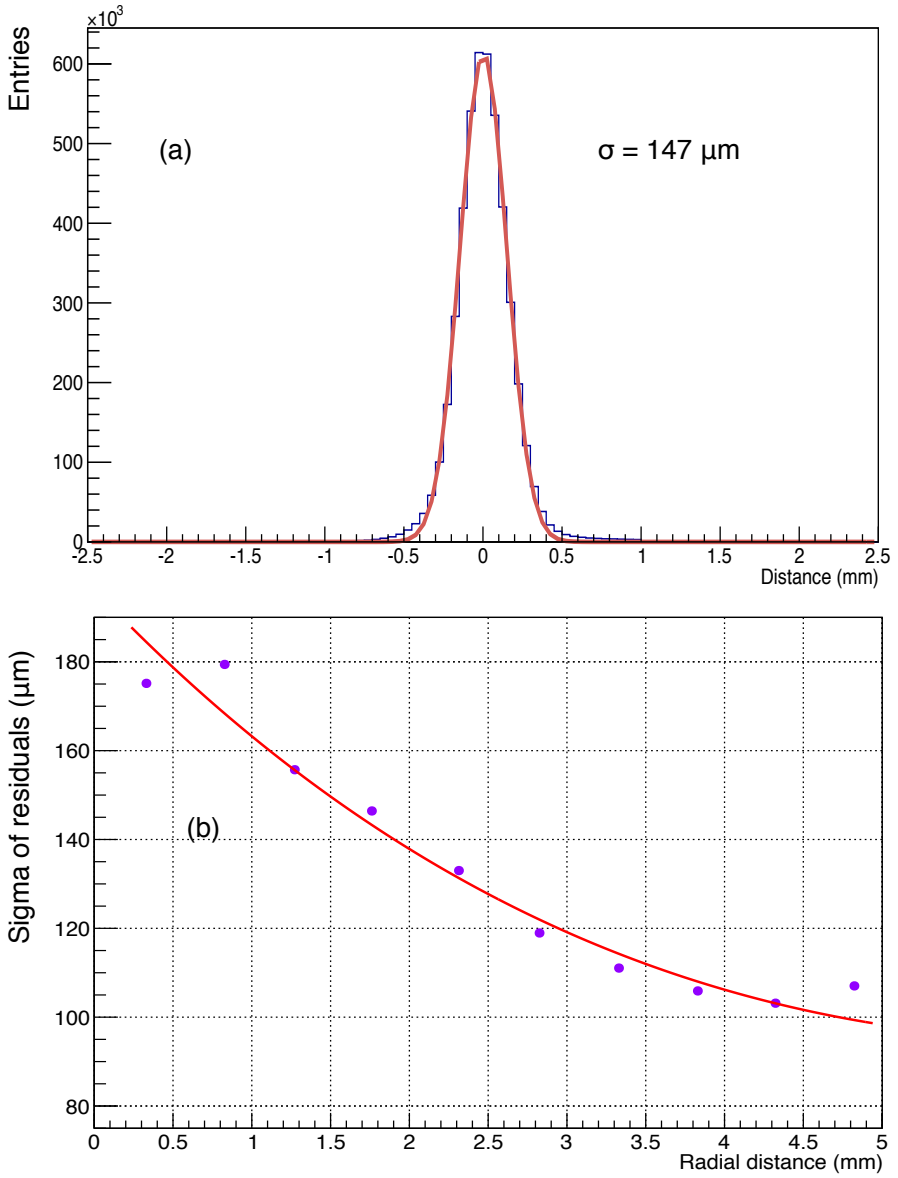

Figure 5.17: (a) The residual distribution obtained with data from the 0.550 GeV/c proton beam at an anode potential of 1800 V. The best residual resolution averaged over the complete drift distance is 146 μm. (b) Width (sigma) of the residual distribution for different intervals of the radial distance to the wire, obtained with data from the 0.550 GeV/c proton beam at an anode potential of 1800 V. The red line is the fit with a third-order polynomial.

Table 5.6: The mean spatial resolution obtained for four proton momenta at three different high voltage settings.

momentum (GeV/c)	$\sigma(\mu\text{m})$, 1750 V	$\sigma(\mu\text{m})$, 1800 V	$\sigma(\mu\text{m})$, 1850 V
0.55	151	146	138
0.75	159	151	144
1.00	164	158	150
2.95	185	171	165

Table 5.7: The mean spatial resolution obtained for three deuteron momenta at three different high voltage settings.

momentum (GeV/c)	$\sigma(\mu\text{m})$, 1750 V	$\sigma(\mu\text{m})$, 1800 V	$\sigma(\mu\text{m})$, 1850 V
0.60	150	143	140
0.75	158	148	143
1.50	169	160	152

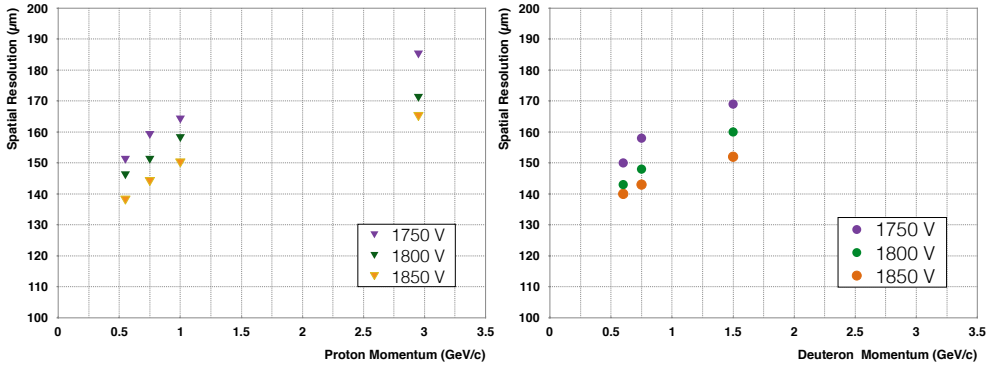

(a) (b)

Figure 5.18: The mean spatial resolution for the proton and deuteron beams as a function of beam momentum and anode potential. (a) Spatial resolution for the data collected in the proton beam test. (b) Spatial resolution for the data collected in the deuteron beam test.

5.7 Energy Resolution

The particle identification technique is based on the specific energy loss (dE/dx), which requires the knowledge of the deposited energy (dE) and the path length (dx). The aim is to extract the specific energy loss, dE/dx, from the data obtained during the prototype test. The deposited energy is obtained by summing over all the energy losses of each hit of the track. The fit of the tracks provides

us with the necessary information to extract the corresponding path length. To obtain the deposited energy, the signals have been integrated over different FADC samples. Since almost the whole charge of the signals is contained within the 50 to 60 samples, the integration window of 60 samples was chosen such that the resolution for dE/dx was optimized. Fig. 5.19 shows the energy loss distribution for data taken with 0.55 GeV/c proton beam. As expected, it shows a typical Landau distribution with a tail towards higher energy losses. This tail worsens the separation power using dE/dx. To optimize the resolution and to convert the Landau distribution into a more Gaussian-like shape, we apply a so-called truncated-mean method [134]. Energy-loss distributions were obtained with the straw tube signals for different truncation fractions, 10%, 20%, 30% and 40%. Fig. 5.19 and Fig. 5.20 show the results of the dE/dx distribution for data taken with 0.55 GeV/c proton beam and 0.6 GeV/c deuteron beam, respectively, with application of different truncation factors. A truncation of 40% turned out to give the best resolution and a distribution that comes the closest to a Gaussian shape. For the truncation fractions smaller than 40%, the shapes are not Gaussian and there are visible long tails. All the steps of the data analysis presented in this sections have been repeated also for the data sample collected while operating at three different high voltages with proton and deuteron beams.

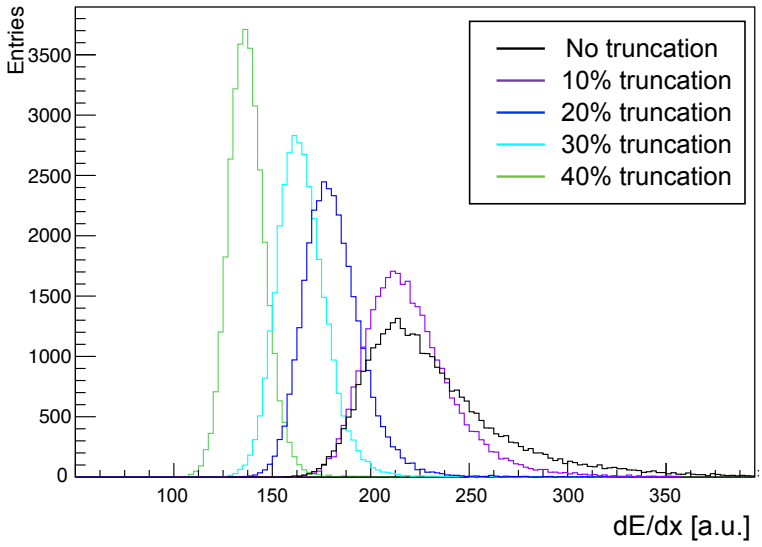

Figure 5.19: dE/dx distributions distribution for the 0.55 GeV/c proton beam. For each histogram a different truncation factor has been applied.

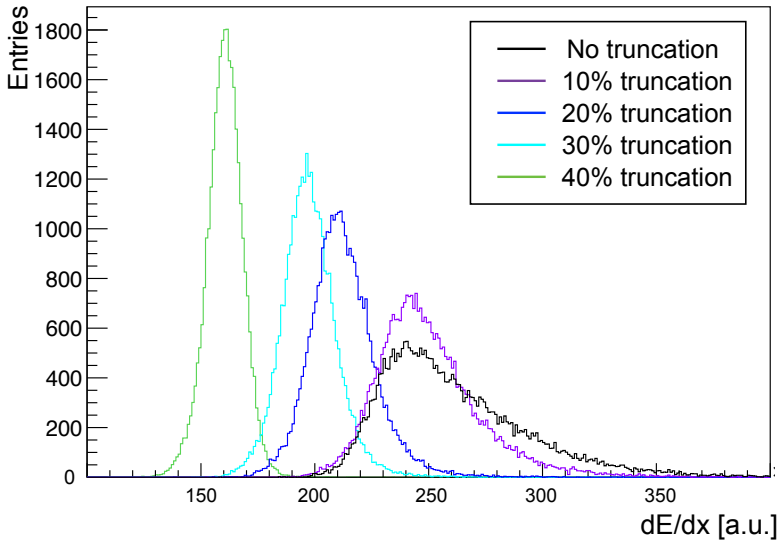

Figure 5.20: dE/dx distributions distribution for the 0.6 GeV/c deuteron beam. For each histogram a different truncation factor has been applied.

Tables 5.8 and 5.9 show the summary of the achieved energy resolution for the data collected with proton beam and deuteron beams, respectively, and at various high voltage settings. The data are represented as well in Fig. 5.21. The obtained resolutions are between 8.2% to 12.3% for proton and 8.9% to 10.6% for deuteron beams.

Table 5.8: The achieved energy resolution for the reconstructed tracks for four proton momenta and in three different high voltages.

Momentum (GeV/c)	dE/dx[%], 1750 V	dE/dx[%], 1800 V	dE/dx[%], 1850 V
0.55	9.0	8.2	7.9
0.75	10 .0	9.1	8.7
1.00	10.9	10.0	9.5
2.95	13.2	12.3	11.5

Table 5.9: The achieved energy resolution for the reconstructed tracks for three deuteron momenta and in three different high voltages.

Momentum (GeV/c)	dE/dx[%], 1750 V	dE/dx[%], 1800 V	dE/dx[%], 1850 V
0.60	9.9	8.9	8.4
0.75	10.8	9.6	9.0
1.50	12	10.6	10.0

The results obtained for other high voltages are very similar to the results of 1800 V, which will be the working high voltage of the $\bar{\text{P}}$ANDA STT for this gas mixture. Increasing the high voltage by 50 V, leads to 1% improvement in the energy resolution. The goal was to check how energy resolution depends on the high voltage applied to the detector.

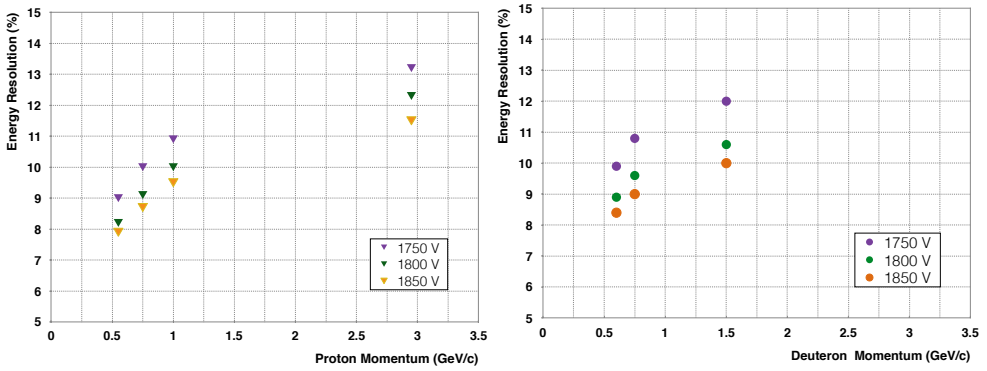

(a) (b)

Figure 5.21: The energy resolution for the proton and deuteron beams as a function of beam momentum and anode potential. (a) Energy resolution for the data collected in the proton beam test. (b) Energy resolution for the data collected in the deuteron beam test.

Fig. 5.22 (a) shows the distribution of dE/dx truncated mean values as a function of momentum for protons and deutrons. In order to evaluate our results, we have made use of the Bethe-Bloch formula [144]. According to the Bethe-Bloch formula, the energy dependence is, to a good approximation, inversely proportional to the square of the speed of the particle. We have evaluated our results by considering the effect of the term $\beta^2 = v^2/c^2$ in the Bethe-Bloch formula, (where v is the speed of the particle) and the results which are presented in Fig. 5.22 (b), are satisfactory and in a good agreement with the Bethe-Bloch formula for both protons and deuterons.

Since we used two different particle types (protons and deuterons) at similar momenta of 0.75 GeV/c, the PID performance of the STT prototype can be tested. Fig. 5.22 shows a satisfactory separation between protons and deuterons at 0.750 GeV/c. Usually, the separation power S between two particles of type A and B characterizes the performance of an identification technique. The separation power S between two particles is defined as the distance between the centers of the two bands $< dE/dx_A >$ and $< dE/dx_B >$, which is measured in terms of the standard deviations. It is obtained from the following equation [134]:

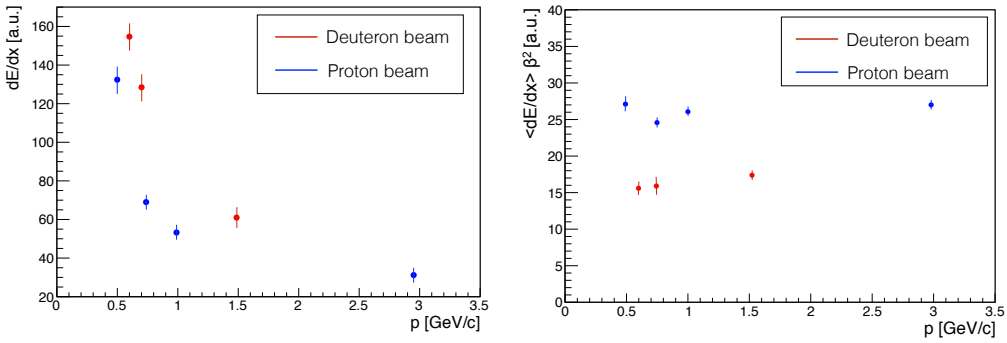

(a) **(b)**

Figure 5.22: (a) Distribution of dE/dx truncated mean values (with 40% truncation) vs momentum for protons and deuterons. (b) Distribution of $dE/dx \times \beta^2$ vs. momentum for protons and deuterons. The vertical error bars represent σ values.

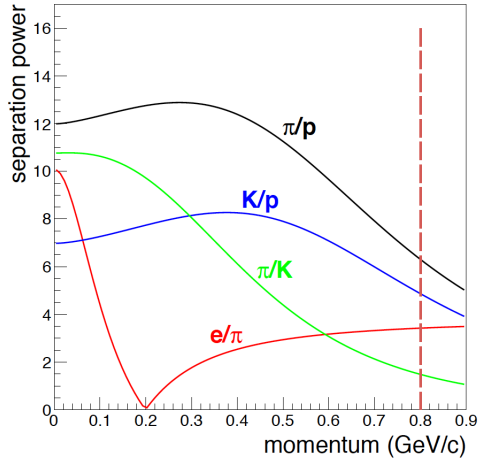

Figure 5.23: Separation power in the STT detector obtained from simulations [134]. The vertical line at 0.8 GeV/c is the chosen threshold for the momentum to perform the particle identification in the STT. Figure is taken from Ref. [134].

$$S = \frac{|< dE/dx_A > - < dE/dx_B > |}{\sigma_A/2 + \sigma_B/2}. \tag{5.5}$$

where $< dE/dx >$ and σ are the mean value and standard deviation of the distributions, respectively, for two particle types A and B. For the proton and deuteron beams at 0.75 GeV/c, the calculated separation power is equal to 6.6. Fig. 5.23 shows the separation power in the STT detector which is obtained from previous simulations [134]. In this figure the separation power is calculated for protons, kaons, pions and electrons, but there is no value for

the separation power between protons and deuterons. In order to compare our calculated separation power with the previous simulated data, we made an estimation using the Bethe-Bloch formula. So, the energy loss of a deuteron or proton with a given momentum can be related to that of a pion or kaon with different momentum but with the same β. Considering the mass of the deuteron, proton and kaon, we related the energy loss of deuterons and protons at a given momentum of 0.75 GeV/c to the energy loss of the protons and kaons at the corresponding momentum of 0.375 GeV/c. Finally, we compared the separation value at 0.75 GeV/c, with the separation power calculated from the simulations between protons and kaons at the corresponding momentum of 0.375 GeV/c. The separation power for the proton and kaon is around 7.75 at 0.375 GeV/c (see Fig. 5.22), and the one we obtained from the tests for the proton and deuteron at 0.75 GeV/c is 6.6 which is sufficiently close to the simulated separation power, and thus is deemed to meet the design requirements.

5.8 Summary and Discussion

The STT prototype, consisting of 128 $\bar{\text{P}}$ANDA straw tubes arranged in eight layers of 16 straws each, has been tested with proton and deuteron beams at COSY. In both measurements the electronic readout of the straw signals consists of trans-resistance amplifiers and flash analog to digital converters (FADC), which sample the analog signal amplitude with a frequency of 240 MHz. In our two in-beam test measurements, the feasibility of the analog readout without active electronics at the detector side by utilizing carefully shielded coaxial signal/HV cables and low noise pre-amplifier has been demonstrated. The tracking performance has been studied with the analysis method described in this chapter, including signal selection, calibration and track reconstruction followed by obtaining the residual distributions and energy measurement. The results of the obtained spatial and energy resolutions are summarized in the previous sections. The presented results indicate that the achieved spatial and energy resolutions in both measurements for proton and deuteron beams are satisfactory and reasonable. The obtained results show that we have achieved the requirements for spatial and energy resolutions, $\sim$150 μm and $\sim$10%, respectively. In addition, the PID performance of our prototype was checked by the separation of two different particles (protons and deuteron) for the similar momentum of 0.750/c GeV, and it represents a clear separation which is quite satisfactory. We obtained a separation power of 6.6 between protons and deuterons with momentum of 0.750 GeV/c, which is very close to the value obtained from simulations for the momentum of 0.375 GeV/c between protons and kaons.

The data have been collected and analyzed for three different high voltages settings (1750 V, 1800 V and 1850 V). The achieved results of the spatial and energy resolutions for these different high voltage setting are also summarized in the previous sections. The results indicate that increasing the high voltage by 50 V leads to a 1% improvement in the energy resolution and a 5% improvement in the spatial resolution. The goal was to check how spatial and energy resolutions depends on the high voltage applied to the detector. The previous studies have shown that for our gas mixtures of interest, by increasing the HV by 50 V, the tube remain in the region of direct proportionality and the gas gain increases from 5×10^4 to 7×10^4 [134]. For the current design of the STT, a moderate gas gain of about 5×10^4 is recommended, because a high gas gain significantly reduces the tube lifetime. Our obtained results show that increasing the HV by 50 V leads to the improvement in spatial and energy resolutions, which is the main goal of STT for PID. Proposing a change in the chosen HV of STT from 1800 V to 1850 V needs more investigation and optimization. In this study we did not take into account how the lifetime of the detector is influenced, we also did not look into the behavior of the detector at high rates.

There is room for improvements in our analysis method and the electronic read out. One can implement more accurate calibration and tracking algorithms. During our beam test measurements we encountered some problems with the pre-amplifiers with low gain and due to frequent tests with the detector, its geometrical stability has been slightly lost. The current setup needs some mechanical inspection and renovation. The new pre-amplifiers with higher gain will improve the specific energy loss resolutions. In addition, the work on highly integrated multi-channel sampling ADC coupled with fast FPGA modules for real time signal-shape analysis is ongoing.

Chapter 6

Summary and Outlook

In this thesis, the capability of $\bar{\text{P}}$ANDA for measuring the production cross section of charmed-baryon pairs in the channel $p\bar{p} \to \Lambda_c\bar{\Lambda}_c$ is studied together with the investigation of the PID capability of a STT prototype via two test measurements with proton and deuteron beams. This chapter summarizes both studies and presents an outlook for future investigations.

6.1 Simulation and Reconstruction Studies of the Production and Decay of $\Lambda_c\bar{\Lambda}_c$

Charmed baryon spectroscopy has received significant attention over the last several years. Experimental and theoretical studies of charmed baryons have been the focus of vigorous research. The $\bar{\text{P}}$ANDA experiment at FAIR is expected to provide new results to help experimentally map out the heavy-baryon sector. The physics program of $\bar{\text{P}}$ANDA focuses on the investigation of the hadron structure and the properties of the strong interaction. Hadron spectroscopy is one of the main topics of the $\bar{\text{P}}$ANDA physics program, and in particular the interest is focused on the charmonium, hidden- and open-charm spectroscopy. There is a great interest in studying the charmed baryon production, and in particular, Λ_c pair baryons production, in the proton-antiproton collisions. The Λ_c baryon plays a significant role in understanding both charm and bottom baryons. Λ_c, as the lightest charm baryon, is common to many decays of the more massive baryons. Compared to the proton, studying the Λ_c has the advantage: since it involves a heavy c-quark, which makes its interpretation easier. Exploiting heavy quark symmetry, allows for systematic analysis of di-quark structure in baryons.

6.1. Simulation and Reconstruction Studies of the Production and Decay of $\Lambda_c\bar{\Lambda}_c$

No experimental data exist for the reaction $p\bar{p} \to \Lambda_c\bar{\Lambda}_c$. This channel is uniquely accessible with $\bar{\text{P}}$ANDA. Chapter 4 of this thesis is devoted to the investigation of the feasibility for the charmed baryon production via the production of $\Lambda_c\bar{\Lambda}_c$ baryon pairs. We simulated the process $p\bar{p} \to \Lambda_c\bar{\Lambda}_c$, in which one or both of the Λ_c baryons decay into $p^{\pm}K^{\pm}\pi^{\pm}$. Our channel of interest, with a branching ratio of 6.35% is one of the most favorable modes of decay [8]. The final state products of the reaction chain are all charged particles. The absence of neutral final-state particles provides the best invariant-mass resolution. In addition, the absence of the neutral final-state particles leads to low multiplicity of tracks which keeps the efficiency high. The goal of this study is to reveal the capability of $\bar{\text{P}}$ANDA to measure the Λ_c baryons in terms of mass and momentum resolution and how well the signal events will be separated from the huge amount of background events. To make a quantitative statement about the production of the Λ_c baryon pairs, we use the statistical significance as a figure-of-merit (FOM) to evaluate the feasibility. The aim is to investigate the cross section sensitivity for a range of luminosities, thereby, reflecting the various operational phases of $\bar{\text{P}}$ANDA. In this thesis, the high beam momentum of 14 GeV/c, available at $\bar{\text{P}}$ANDA has been selected. The reason for choosing a high incident beam momentum is, because it has been predicted that the production cross section for the channel of interest increases with momentum.

For the feasibility study, we performed a Monte Carlo simulation of the decay channel $p\bar{p} \to \Lambda_c\bar{\Lambda}_c \to p^+K^-\pi^+p^-K^+\pi^-$, using the PandaRoot analysis framework. The Monte Carlo simulated data are generated using EvtGen and the final-state particles are further propagated through various materials using GEANT4. The specific detector and electronic responses are modeled as well. The goal is to make the simulation data as similar as possible to an actual experiment. The simulated data are further processed via high-level reconstruction and analysis tools. These include Kalman-based track finding and fitting algorithms and likelihood-based particle identification (PID) methods. For the PID, we exploited the information of the MVD, STT, EMC, DISK, DIRC, RICH and TOF. For the event reconstruction, we considered two different modes which we refer to as the inclusive and exclusive analysis. For the inclusive study, we only reconstructed the decay products of one of the charmed baryons. In the exclusive method, we reconstructed all the final-state particles of both charmed-baryon decays. In both methods of reconstruction, several cuts and kinematic fits were applied to optimize the FOM. We reconstructed the invariant mass of the Λ_c baryons pairs. For the inclusive reconstruction, we obtained a missing-mass resolution of 15.8 MeV/c^2 with a reconstruction efficiency of 14.3%. For the exclusive method, the invariant-mass resolution improves and a value of 6.8 MeV/c^2 has been obtained with a reduction in efficiency of 4.5%. The efficiencies were smaller than naively expected. The

reason for this has been traced back to the performance of the PID algorithm. We expect that there is still room for improvement by optimizing the PID framework in PandaRoot which is outside the scope of this thesis. For the inclusive reconstruction we obtained a cross section sensitivity of ∼15 nb at a 5σ statistical significance for the phase-one luminosity 2×10^{32} cm^{-2} s^{-1} of $\bar{\text{P}}$ANDA for a measurement time of one month. This cross section sensitivity of $\bar{\text{P}}$ANDA would be sufficient to observe a signal at phase-one according to various model predictions. For the exclusive mode, only an upper limit on the sensitivity is obtained (see Fig. 4.24). The calculation of the FOM has shown that for our channel of interest, although for the exclusive analysis a higher background suppression is obtained, on the other hand it suffers from the total branching fraction, which is lower than the inclusive mode, and a very low efficiency (∼4.5%). We made use of a pure phase space model, which is not very accurate. One aspect that certainly needs to be considered is to include a more realistic angular distribution of the production of Λ_c pairs and their decays.

In addition, since one part of this thesis is devoted to an in-beam test measurement of the STT prototype, the role and contribution of the STT in the PID of our channel of interest is investigated. For our channel of interest, the STT has a marginal contribution to the PID performance. The reason for this is that, a large fraction of the final-state particles has relativistic velocities, therefore, the energy loss dE/dx becomes minimum ionizing, which results in similar energy deposits for (anti)protons, kaons, and pions. In contrast, the DIRC detectors are the most effective PID detectors for the channel of interest. The STT will play an important role in the PID for decay channels, in which the daughter particles that have low momenta ($<$1 GeV/c).

It is worth mentioning that a more detailed study of the background is needed. This will require a larger data set of DPM events than we have produced. Moreover, to solve the problem with the statistics, one can use some filters and be more selective in which background channels to generate. The most important background contribution is the non-resonant reaction $p\bar{p} \to p^+K^-\pi^+p^-K^+\pi^-$. The cross section for this reaction is known to be 0.02 mb [146]. Another aspect is that the channels which contain hadrons with charm content are not included in DPM. For our channel of interest, we made use of the beam momentum of 14 GeV/c, which is far above the productions threshold of the Λ_c baryon pairs. Therefore, using such a relatively high beam momentum, we expect that other channels open up that contain excited charmed baryons. These excited charmed baryons will also contribute to the background. It would, therefore, be useful to generate such type of background events explicitly and study their contribution. Alternatively, one might consider to produce open-charm baryons close to their production threshold. This would avoid the production of ex-

cited states, but it will come with the price that the cross section of the signal channel is lower than at higher energies. The mass and momentum resolution should be investigated in that case, as it is expected to be better than when choosing a momentum very far above the Λ_c baryon production threshold. The simulation of the Λ_c baryon pairs can be extended to other decay modes as well. A difficulty is that the Λ_c has many decay modes with branching ratios of less than one percent [8]. Λ_c has a very short life time, $c\tau = 59.9$ μm [8], and decays very close to the interaction point. With such a short lifetime, a secondary vertex fit would not help to further reduce the background. In this respect, the decay $\Lambda_c \to \Lambda\pi^+$, which has a branching fraction of 1.3% [8], would be useful to consider since the Λ particle has a relatively large lifetime ($c\tau = 7.89$ cm) [8]. A secondary vertex fit would in this case be a powerful tool that can be used as a cut to optimize the signal-to-background ratio. Another interesting channel to consider is $\Lambda_c \to \Lambda\pi^+\pi^0$, with a branching fraction of 7.1% [8]. Besides the additional Λ particle with its long lifetime and the relatively large branching fraction, the momenta of the final-state particles will be lower compared to the channel discussed in this thesis which will result in a more effective PID. This decay channel includes a neutral pion which can be detected via its two-photon decay. These photons could convert externally and will give a large multiplicity of clusters in the electromagnetic calorimeter. This will likely result in combinatorial background and a reduction in the detection efficiency. In this case, one might need to consider using machine learning methods such as exploiting multi-variate analysis (MVA) techniques.

6.2 In-Beam test measurements with the STT prototype at COSY

The task of the tracking detectors is to measure the trajectories of charged particles through the magnetic fields, leading to measurements of the momenta of charged particles. In $\bar{\text{P}}$ANDA, such measurements will be provided by four tracking detectors (see Fig. 3.7 and Fig. 3.8). The STT is one of the main tracking detectors. The tasks of the STT are to determine the momenta of charged particles, via a precise spatial reconstruction of particle tracks in combination with a solenoid magnetic field, and to perform particle identification (PID) by a measurement of the specific energy loss (dE/dx). The PID information of the STT is necessary to separate protons, kaons and pions in the momentum region below 1 GeV/c. To achieve this goal the development of the electronic readout of the STT plays a crucial role and it is guided by optimizing the spatial and energy resolutions. Two electronic readout systems have been proposed for STT, a system based on FADCs and one based on ASICs. Since the $\bar{\text{P}}$ANDA detector is still under construction, the tracking performance of

the STT is studied via in-beam test measurements with the STT prototype. The data were obtained at the COSY accelerator in Jülich research center with proton and deuteron beams. The focus of this thesis is on the beam test of the STT prototype with the FADC read out and it describes the analysis of data from measurements with proton and deuteron beams. Using two different beams allow us to investigate the separation power of the STT between the different particle types. In both tests, the experimental setup was identical and in each test several beam momenta and high voltage settings were considered.

The STT prototype consists of 128 $\bar{\text{P}}$ANDA straw-type tubes which are arranged in eight layers of 16 straws. In our experimental setup the straw tubes were directly connected by 12 m coaxial signal/HV cables to the electronics placed outside of the detector prototype, in the experimental area. The raw signals from the straw tubes were transmitted via cables to analog and digital electronics. Placing electronics outside the detector solves radiation hardness and heat problems for the usage of the STT in the actual $\bar{\text{P}}$ANDA setup. In the two in-beam test measurements, the feasibility of using an analog readout with shielded coaxial signal and high-voltage cables and low-noise pre-amplifiers, thereby, avoiding active electronics near the detector, has been demonstrated. We studied the tracking performance, using signal selection, calibration and track reconstruction that is followed by residual distributions and energy measurements. To obtain a good track recognition, in all steps of the current analysis the track reconstruction efficiency was always considered above 80%. The spatial resolution is sensitive to the momentum of the particles traveling through the tubes. For momenta that are close to minimum ionizing, fewer clusters of electrons reach the wire which leads to a larger uncertainty in the distance determination of the nearest cluster to the wire. As the result, the error of this distance is larger which worsens the resolution. The results of the obtained spatial and energy resolutions for proton and deuteron beams are summarized in Tables 5.3 and 5.4. The obtained results show that we have achieved the requirements for spatial resolutions and the energy resolution of $\sim$150 μm and $\sim$10%, respectively. In addition, the results indicate that increasing the high voltage by 50 V leads to about a one percentage point improvement in the energy resolution and 5% improvement in the spatial resolution. The goal was to check how spatial and energy resolutions depends on the high voltage applied to the detector. For the current design of the STT a moderate gas gain of about 5×10^4 is recommended, because a high gas gain significantly reduces the tube lifetime. Our obtained results show that increasing the HV by 50 V leads to the improvement in spatial and energy resolutions, which is the main goal of STT for PID. Proposing a change in the chosen HV of STT from 1800 V to 1850 V needs more investigation and optimization, because in this study we did not take into account how the lifetime of the detector is influenced, and also the behavior at high rate was not addressed.

The PID performance of our prototype was checked by studying the separation power for two different particle types, namely protons and deuterons, at a similar momentum of 0.750 GeV/c. A clear separation has been observed. We obtained a separation power of 6.6 between protons and deuterons with momentum of 0.750 GeV/c, which is very close to the value obtained from simulations for the momentum of 0.375 GeV/c between protons and kaons (see section 5.7).

The analysis methods and techniques can be improved by modifying the feature-extraction algorithm from the raw signal and by modifying the calibration procedure. One might consider to use different methods to extract the time reference of each analog signal. For example, a performance study using the leading-edge or constant-fraction time could lead to different results. For the calibration, we made use of an empirical function. There might be room for improvement of this function to get a more accurate determination of the minimum and maximum drift times. Performing tests with muon beams would also be very beneficial for the reconstruction, since the muons leave clean tracks in the straw tubes. During our beam test measurement, we encountered some problems with the pre-amplifiers with low gain and due to frequent tests with detector, its geometrical stability has not been very optimal. The current setup needs some mechanical inspection and renovation. Performing tests using cosmic rays will also provide us with some information about the performance and imperfections in our mechanical setup. It is worth to mention that the development of the analog part of the readout (cables, shielding, coupling boards) and the new pre-amplifier and its integration into ADC board is ongoing. In addition, the work on highly integrated multi-channel sampling ADC coupled with fast FPGA modules for real time signal-shape analysis is ongoing. In the work presented in this thesis, we did not use the real-time pulse-shape algorithms that can be implemented in the FPGAs. For the $\bar{\text{P}}$ANDA experiment, one will make use of these online features. It is, therefore, worthwhile to perform benchmark studies comparing the results of the online and offline feature extraction. All the proposed changes in the electronic readout and the software have to be investigated in beam tests. Finally the optimum, based on the performance and cost has to be considered for the $\bar{\text{P}}$ANDA experiment.

Nederlandse Samenvatting

In de vorige eeuw was de Mendeleev tabel in staat de onderliggende structuren van de grote hoeveelheid chemische elementen aan te tonen, de relaties tussen de verschillende elementen te onthullen en om het bestaan van nog niet eerder getoonde elementen te voorspellen. In de zestiger en zeventiger jaren werd er geleidelijk aan een model ontwikkeld waarmee de tal van elementaire deeltjes, die werden onthuld in experimenten met versnellers, ingedeeld konden worden en waarmee nieuwe deeltjes voorspeld konden worden. Dit model staat nu bekend als het Standaard Model (SM) van de deeltjesfysica. Elke ontwikkeling dat verder gaat dan het huidige SM vraagt om verdere en meer precieze metingen van de eigenschappen van deze fundamentele deeltjes van de natuur.

Wereldwijd creëren veel wetenschappers geavanceerde machines om de fysica binnen het huidige SM te onderzoeken en de interacties tussen de deeltjes te begrijpen. Een van deze machines is de toekomstige multifunctionele detector "antiProton ANnihilatie in DArmstadt" ($\bar{\text{P}}$ANDA). $\bar{\text{P}}$ANDA zal een van de belangrijkste experimenten zijn bij de toekomstige Faciliteit voor Antiproton en Ion Onderzoek (FAIR), welke in aanbouw is in Darmstadt, Duitsland. Het $\bar{\text{P}}$ANDA experiment zal botsingen onderzoeken tussen een straal van antiprotonen en een gefixeerd proton of nucleair doelwit. $\bar{\text{P}}$ANDA heeft een unieke opstelling vergeleken met andere natuurkunde experimenten en zal een unieke toegang geven tot verschillende onderwerpen binnen het vakgebied van de sub-atomaire fysica. Eén specifiek aspect van het programma van $\bar{\text{P}}$ANDA is hadron spectroscopie, met in het bijzonder interesse voor verborgen- en open-charm spectroscopie en (strange-)baryon spectroscopie.

$\bar{\text{P}}$ANDA bestaat uit verschillende detector onderdelen die elk een bepaalde taak vervullen. Eén van de belangrijke taken is de reconstructie van de impuls van elektrisch geladen deeltjes, die gebaseerd is op informatie verkregen van de baandetectoren. $\bar{\text{P}}$ANDA heeft vier belangrijke baandetectoren en één daarvan is de Straw Tube Tracker (STT), een cilindrische detector die bestaat uit met gas gevulde buizen. De taken van de STT zijn het bepalen van de impuls van geladen deeltjes door een nauwkeurige ruimtelijke reconstructie van

de afgelegde banen gecombineerd met het magnetische veld van een solenoïde, en het uitvoeren van deeltjesidentificatie (PID) door het specifieke energieverlies te meten. De PID informatie van de STT is nodig om onderscheid te maken tussen protonen, kaonen en pionen met een impuls minder dan 1 GeV/c. De elektronische uitlezing van de STT speelt een cruciale rol in het bereiken van dit doel en is gericht op optimalisatie van de ruimtelijke en energie resoluties. Twee elektronische uitleessystemen zijn voorgesteld voor de STT, een systeem gebaseerd op FADCs en een systeem gebaseerd op ASICs. Aangezien de $\bar{\text{P}}$ANDA detector nog in aanbouw is zijn de prestaties van de STT bestudeerd aan de hand van test experimenten met het STT prototype. De data is verkregen bij de COSY versneller in het Jülich onderzoekscentrum met bundels van protonen en deuteronen. De focus van dit proefschrift ligt op het testen van het STT prototype met de FADC uitlezing en beschrijft de analyse van data verkregen door met bundels van protonen en deuteronen. Het gebruik van twee verschillende soorten bundels zorgt ervoor dat onderzocht kan worden hoe goed de STT onderscheid kan maken tussen de verschillende type deeltjes. In beide tests was de experimentele opstelling identiek en werd er geëxperimenteerd met verschillende bundelenergieën en hoogspanningswaarden. Het STT prototype bestaat uit 128 holle buizen die gerangschikt zijn in 8 lagen van 16 buizen. In onze experimentele opstelling waren de buizen met 12 m lange coaxiale signaal/HV kabels direct verbonden met de elektronica de elektronica welke buiten de experimentele ruimte was geplaatst. Wij hebben de baan detectie prestaties bestudeerd door middel van signaal selectie, kalibratie en baan reconstructie gevolgd door overige verdelings- en energiemetingen. De ruimtelijke resolutie is gevoelig voor de impuls van deeltjes die door de buizen bewegen. De verkregen resultaten laten zien dat wij de vereiste ruimtelijke resoluties en energie resolutie van respectievelijk $\sim$150 μm en $\sim$10%. behaald hebben. Verder laten de resultaten zien dat het verhogen van het hoge voltage met 50 V leidt tot ongeveer een procent verbetering in de energieresolutie en vijf procent in de ruimtelijke resolutie. De PID prestatie van ons prototype is getoetst door het onderscheidingsvermogen voor twee verschillende deeltjes, namelijk protonen en deuteronen, te meten bij dezelfde impuls van 0.750 GeV/c. Een duidelijk onderscheid was zichtbaar. Wij hebben een onderscheidingsvermogen van 6.6 verkregen voor protonen en deuteronen met een impuls van 0.750 GeV/c, wat zeer dichtbij de waarde ligt die is verkregen door simulaties voor protonen and kaonen met een impuls van 0.375 GeV/c.

De verwachting is dat het $\bar{\text{P}}$ANDA experiment zal voorzien in nieuwe resultaten die helpen de zware-baryon sector experimenteel in kaart te brengen. Het Λ_c baryon speelt een significante rol in het begrijpen van zowel charm als bottom baryonen. Λ_c, als lichtste charm baryon, is veelvoorkomend in het verval van zwaardere baryonen. Er bestaat geen experimentele data voor de reactie $p\bar{p} \rightarrow \Lambda_c\bar{\Lambda}_c$. Dit kanaal is enkel toegankelijk met $\bar{\text{P}}$ANDA. Een deel van dit

proefschrift is toegewijd aan het onderzoeken van de haalbaarheid van charm baryon studies via de productie van $\Lambda_c\bar{\Lambda}_c$ baryon paren. Wij hebben het proces $p\bar{p} \to \Lambda_c\bar{\Lambda}_c$ gesimuleerd, waarin één van beide Λ_c baryonen vervalt in $p^{\pm}K^{\pm}\pi^{\pm}$. Het doel van deze studie is aan te tonen wat de capaciteit van $\bar{\text{P}}$ANDA is om Λ_c baryonen te meten in termen van massa en impuls resolutie en hoe goed het signaal gescheiden kan worden van de gigantische hoeveelheid aan achtergrond. Om een kwalitatief statement te kunnen maken over de productie van Λ_c baryon paren gebruiken wij statistische significantie als graad van verdienste (FOM) om de haalbaarheid te evalueren. Het doel is om de gevoeligheid voor de werkzame doorsnede te bepalen voor een scala aan luminosteiten, die de verschillende operationele fases van $\bar{\text{P}}$ANDA weerspiegelen. Voor de haalbaarheidsstudie hebben wij een Monte Carlo simulatie gedaan van het verval $p\bar{p} \to \Lambda_c\bar{\Lambda}_c \to p^+K^-\pi^+p^-K^+\pi^-$ met gebruik van het PandaRoot analyse framework. Voor de reconstructie van de reactie hebben wij twee verschillende methodes gebruikt waar wij naar refereren als de inclusieve en de exclusieve analyse. Voor de inclusieve analyse hebben wij alleen de vervalproducten van één van de charm baryonen gesimuleerd. In de exclusieve methode hebben wij alle uiteindelijke vervalproducten van beide charm baryonen gesimuleerd. Voor de inclusieve reconstructie hebben wij een ontbrekende-massa resolutie van 15.8 MeV/c verkregen met een reconstructie efficiëntie van 14.3%. Voor de exclusieve methode verbetert de invariante-massa resolutie en een waarde van 6.8 MeV/c wordt verkregen met een afname in efficiëntie van 4.5%. Voor de inclusieve reconstructie hebben wij een werkzame-doorsnede gevoeligheid verkregen van $\sim$15 nb met 5σ statistische significantie voor een luminositeit van luminositeit 2×10^{31} cm^{-2} s^{-1} $\bar{\text{P}}$ANDA bij een meettijd van een maand. Deze werkzame-doorsnede gevoeligheid van $\bar{\text{P}}$ANDA zou volgens verschillende voorspellingen genoeg zijn om een signaal the observeren in de eerste meetperiode van $\bar{\text{P}}$ANDA. Voor de exclusieve modus is alleen een bovenlimiet voor de gevoeligheid verkregen. Aangezien een deel van deze thesis is toegewijd aan een testmeting van het STT prototype is daarnaast de rol en bijdrage van de STT in de PID van ons kanaal onderzocht. Voor ons kanaal heeft de STT een marginale bijdrage aan de PID prestatie.

Acronyms

ABS Acrylonitrile-Butadiene-Styrene
ADC Analog-to-Digital Converter
APPA Atomic Plasma Physics and Applications
ASIC Application-Specific-Integrated Circuit

BEMC Barrel ElectroMagnetic Calorimeter
BESIII BEijing Spectrometer III
BG Box Generator
BTOF Barrel Time-Of-Flight

CBM Compressed Baryonic Matter
COSY COoler SYnchrotron
CR Collector Ring

DAQ Data Acquisition
DB Digital Board
DIRC Detection of Internally Reflected Cherenkov light
DPM Dual Parton Model

EFT Effective Field Theory
EvtGen Event Generator

FADC Flash Analog-to-Digital Converter
FAIR Facility for Antiproton and Ion Research
FEMC Forward ElectroMagnetic Calorimeter
FMS Forward Muon System
FOM Figure-Of-Merit
FPGA Field-Programmable-Gate Array
FS Forward Spectrometer
FSC Forward Shashlyk-type Calorimeter
FTOF Forward Time-Of-Flight

FTS Forward Tracking System
FZJ Forschungszentrum Jülich

GEANT3 GEometry ANd Tracking version 3
GEANT4 GEometry ANd Tracking version 4
GEM Gas Electron Multiplier
GPD General Parton Distributions
GSI GSI Helmholtz Center for Heavy Ion Research

HESR High Energy Storage Ring
HL High-Luminosity
HR High-Resolution
HV-MAPSs High Voltage Monolythic Active Pixel Sensors

LHC Large Hadron Collider
LMD Luminosity Detector
LQCD Lattice Quantum ChromoDynamics

MC Monte Carlo
MCP-PMT Micro-Channel Plate Photo-Multiplier Tubes
MDT Mini-Drift Tubes
MVD Micro Vertex Detector

NUSTAR Nuclear Structure Astrophysics and Reactions

p-LINAC Proton LInear ACcelerator
PANDA antiProton ANnihilation in DArmstadt
PDG Particle Data Group
PID Particle IDentification

QCD Quantum ChromoDynamics
QED Quantum Electrodynamics

RESR Recuperated Experimental Storage Ring
RICH Ring Imaging Cherenkov
RS Range System

SM Standard Model
STT Straw Tube Tracker
Super-FRS Super Fragment Separator

TDC Time-to-Digital Converter
TOT Time-Over-Threshold

TS Target Spectrometer

UNILAC UNIversal Linear ACcelerator

List of Figures

List of Tables

Acknowledgments

This is the end to my exciting PhD journey. A PhD can seem endless when one first begins, and even more near the end, as working to finalize all of the things. Having gone through this stressful, frustrating, interesting and sometimes fun journey, that is doing a PhD, was extremely a challenging work. Although only my name appears on the cover of this thesis, many people have contributed and their support and profound impact had made this dissertation possible. I would like to thank all the people who helped me along this journey. I would like to apologize in advance, if I have forgotten to mention those who have supported me along this way.

My first thanks go to my promoters and supervisors. I would like to thank Prof. Nasser Kalantar-Nayestanaki, who gave me the opportunity to be a member of his group at KVI-CART and supported me during the course of my PhD. Nasser, your valuable supervision, immense patience and constructive criticism helped me to work efficiently on my project. Many thanks for everything.

I want to express my gratitude to Prof. James Ritman, I truly appreciate the chance of being part of your group at IKP, in Forschungszentrum Jülich. Jim, although you were very busy, the door of your office was always open to me. Your wealth of knowledge, understanding and kindness enabled me to discuss openly almost every single issue with you. Thanks for your support and supervision during my PhD.

It is time to thank my daily supervisor, Dr. Johan Messchendorp, who gave me the opportunity to work in the nuclear and hadronic group at KVI-CART, and supported me throughout my entire PhD. Johan, you have been the first one to read my writings and to comment on my mistakes patiently. You always had deep insights to tackle technical and programming problems, which I faced during my analysis and performing simulation. I am deeply grateful for everything you have done for me, and for your help.

I would like to thank Dr. Peter Wintz, my daily supervisor at IKP. I really appreciate the opportunity of being part of the STT group at Forschungszentrum Jülich. You have always been a source of motivation and useful advice. I really enjoyed all the beam times we had together. Peter, thanks for your support and supervision during my PhD. You were always so kind to me and I will never forget your calm character. Here, I also want to thank my collaborators in the STT group, Krzysztof Pysz and Pawel Kulessa. I can not imagine working in the lab, during the STT prototype in-beam tests, without their help. They have been greatly generous by offering programs, calibration data and useful advise.

Furthermore, I would like to acknowledge and thank the reading committee of my thesis, Prof. Olaf Scholten, Prof. Klaus Peters and Prof. Bernd Krusche, for their time and effort in improving my dissertation.

Dear Rosa and Victor, thank you for being my paranymphs. Rosa, thank you very much for translating the summary of my thesis into Dutch. I am grateful to all of my colleagues and friends at KVI. Prof Muhsin Harake (I am deeply inspired with your knowledge and insights in experimental and theoretical physics), Myroslav, Catherine, Oksana, Peter, Herbert, Mohammad Babai (thanks for your help in programming, PandaRoot installation issues and discussions), Jacco van de Weele (especial thanks for debugging problems in KVI cluster, without your technical help and knowledge I could not run my analysis smoothly), Julia Even, Hilde van der Meer, Ola, Gita, Soumya, Olena, Josbert, Stepfano, Christiaan, Ali Najafi, Hossein, Olga, Mehdi, Parisa, Hajar, Meisam, Brankica, Marcel, Alex, Reza, Ali Mollaebrahimi, Qader, Mina, Auke, Gia, Shahrzad, Soheil, Brian, Ikechi, thank you all for making my time at KVI unforgettable, I will carry the memory of being together for the rest of my life.

My truly appreciation goes to my best office-mate ever, Mohammad Bayat. Thanks for your company, support, discussions and the time we spend together at our office. Thank you for everything.

I would like to thank my colleagues and friends at Forschungszentrum Jülich. Dr. Elisabetta Prencipe, Dr. Tobais Stocockmanns, Dr. Albrecht Gilitzer, Dr. Susan Schadmand, Jennifer, Lu, Artur, Michael, Florian, Maria, Ludovico, Alessandra, Huagen, Andre, Andreas, Daniel, Shirin, Keivan, Maryam, Anahita, thank you all for making my time in Jülich unforgettable.

Finally, my foremost thanks and appreciation go to my family. Words can not express my gratitude to my family. My sweetheart sister and my beloved brother, thank you for your endless support, kindness and care. Being far

from you is very difficult and I miss you every moment. Mom and Dad, I am writing these lines with tears in my eyes. No words can express my feelings and I can not thank you enough for all that you have done for me. You have always encouraged me to go on and make my dreams come true. Without you, I could not survive in hard times of my life. Thank you very much for your company, care and endless support in every single moment of my PhD journey to become a doctor. Thank you for your infinite and unconditional love. This thesis could not have been accomplished without your patience, support and encouragement. This thesis is dedicated to you. I love you so much ...

October 1, 2018
Solmaz

Bibliography

[1] J. Renn. Einstein's invention of Brownian motion. *Ann. Phys. (Leipzig) 14*, 2005.

[2] I. Falconer. J. J. Thomson and the discovery of the electron. *Phys. Edu., Vol. 32, No. 4*, 1999.

[3] A. Lakhtakia. Models and modelers of hydrogen. *Am. J. Phys. 65, 933*, 1997.

[4] J. D. Rogers. The Neutron's Discovery - 80 Years on. *Physics Procedia, Vol. 43, pp. 1-9*, 2013.

[5] L. Wolfenstein. Inventing the neutrino. *Nucl. Phys. B, Proc. Suppl., Vol. 221, pp. 317-319*, 2011.

[6] E. D. Courant. Early milestones in the evolution of accelerators. *Rev. Acc. Sci. Tech., Vol. 1, pp. 1-5*, 2008.

[7] Picture by user E2m at Wikimedia Commons. The Standard model of elementary particles. `https://en.wikipedia.org/wiki/Standard_Model`.

[8] M. Tanabashi *et al.*, (Particle Data Group). Review of particle physics. *Phys. Rev. D 98, 030001*, 2018.

[9] A. Herten. GPU-based Online Track Reconstruction for $\bar{\text{P}}$ANDA and Application to the Analysis of $D \to K\pi\pi$. *PhD thesis. Ruhr-University Bochum*, 2015.

[10] N. Cabibbo. Unitary symmetry and leptonic decays. *Phys. Rev. Lett. 10, 531*, 1963.

[11] M. Kobayashi and T. Maskawa. CP violation in the renormalizable theory of weak interaction. *Prog. Theor. Phys. 49, 652*, 1973.

[12] S. L. Glashow. Partial-Symmetries of Weak Interactions. *Nucl. Phys. Vol. 22, No. 4*, Feb. 1961.

[13] F. Halzen and A. D. Martin. Quarks and Leptons: An Introductory Course in Modern Particle Physics. *John Wiley and Sons, Inc.*, 1984.

[14] G. Aad *et al.*, Observation of a new particle in the search for the Standard Model Higgs boson with the ATLAS detector at the LHC. *Phys. Lett. B 716*, 2012.

[15] S. Chatrchyan *et al.*, Observation of a new boson at a mass of 125 GeV with the CMS experiment at the LHC. *Phys. Lett. B 716*, 2012.

[16] V. Khachatryan *et al.*, Measurement of the inclusive 3-jet production differential cross section in protonproton collisions at 7 TeV and determination of the strong coupling constant in the TeV range. *Eur. Phys. J. C 75*, 2015.

[17] M. Thomson. Modern Particle Physics, *Cambridge University Press, QCD793.2.T46*, 2013.

[18] G. M. Prosperi, M. Raciti and C. Simolo. On the running coupling constant in QCD, *Prog. Part. Nucl. Phys. 58, pp. 387-438*, 2007.

[19] M. Gell-Mann. A schematic model of baryons and mesons. *Phys. Lett. 8(3), pp. 214-215*, 1964.

[20] Picture by user E2m at Wikimedia Commons. `https://commons.wikimedia.org/wiki/File:Meson_nonet_-_spin_0.svg`.

[21] E. Swanson. New Particle Hints at Four-Quark Matter. *University of Pittsburgh, Pittsburgh, PA 15260, USA*, 2013.

[22] A. Aaij *et al.*. Observation of the resonant character of the $Z^-(4430)$ state. *Phys. Rev. Lett. 112, 222002*, 2014.

[23] V. M. Abazov *et al.*, Evidence for a ${B_s}^0\pi^\pm$ state. *Phys. Rev. Lett. 117, 022003*. `https://doi.org/10.1103/PhysRevLett.117.022003`, 2016.

[24] Picture by user E2m at Wikimedia Commons. `https://commons.wikimedia.org/wiki/File:Meson_nonet_-_spin_1.svg`.

[25] N. Timneanu. The color of gluon interactions: studies of Quantum Chromodynamics in soft and hard processes. *PhD Thesis. Uppsala University*, 2002.

[26] R. Aaij *et al.*, Observation of $J/\Psi p$ resonances consistent with pentaquark states in ${\Lambda^0}_b \to J/\Psi k^- p$ decays. *Phys. Rev. Lett. 115, 072001*, 2015.

[27] P. Adlarson *et al.*, Abashian-Booth-Crowe effect in basic double-pionic fusion: a new resonance?. *Phys. Rev. Lett. 106, 242302*, 2011.

[28] M. Bashkanov, S. J.Brodsky and H. Clements. Novel six-quark hidden-color dibaryon states in QCD. *Phys. Rev. Lett. B 727, pp. 438-442*, 2013.

[29] P. Adlarson *et al.*, Evidence for a new resonance from polarized neutron-proton scattering. *Phys. Rev. Lett. 112(20), 202301*, 2014.

[30] W. Roberts and M. Pervin. Heavy Baryons in a Quark Model. *arXiv:0711.2492 [nucl-th]*, 2008.

[31] J. Richard. An introduction to the quark model. *arXiv:1205.4326v2 [hep-ph]*, 2012.

[32] P. Rubio, S. Collins and G. S. Baliy. Charmed baryon spectroscopy and light flavor symmetry from lattice QCD. *Phys. Rev. D 92, 034504*, 2015.

[33] E. Solovieva. Charmed Baryons Spectroscopy. *J. Phys. : Conf. Ser. 798 012099*, 2017.

[34] E. Cazzoli, *et al.*, Quantum Numbers and Decay Widths of the $\psi(3095)$. *Phys. Rev. Lett. 34, 1125*, 1975.

[35] B. Knapp *et al.*, Observation of a Narrow Antibaryon State at 2.26 GeV/c^2. *Phys. Rev. Lett. 37, 882*, 1976.

[36] The SELEX Collaboration. First Observation of the Doubly Charmed Baryon ${\Xi_{cc}}^+$. *arXiv:hep-ex/0208014v1*, 12 Aug 2002.

[37] The LHCb collaboration. Observation of the doubly charmed baryon ${\Xi_{cc}}^{++}$. *arXiv:1707.01621v2 [hep-ex]*, 14 Sep 2017.

[38] S. Ogilvy. Charmed baryons from LHCb. *arXiv:1509.05611v1 [hep-ex]*, 18 Sep 2015.

[39] R. Chistov *et al.*, Observation of new states decaying into ${\Lambda_c}^+ \ k^- \ \pi^+$ and ${\Lambda_c}^+ \ {k_s}^0 \ \pi^-$. *Phys. Rev. Lett. 97, 162001*, 2006.

[40] T. Lesiak. Charmed baryon spectroscopy with Belle. *arXiv: hep-ex /0605047*, 2006.

[41] R. Mizuk *et al.*, Observation of an isotriplet of excited charmed baryons decaying to ${\Lambda_c}^+ \ \pi$. *Phys. Rev. Lett. 94,122002*, 2005.

[42] B. Aubert *et al.*, A Study of excited charm-strange baryons with evidence for new baryons ${\Xi_{cc}}^+(3055)$ and ${\Xi_{cc}}^+(3123)$. *Phys. Rev. D 77, 012002*, 2008.

[43] FAIR- Facility for Antiproton and Ion Research. `http://www.fair-center.de`.

[44] The $\bar{\text{P}}$ANDA Collaboration. Physics performance report for $\bar{\text{P}}$ANDA, strong interaction studies with antiprotons. *arXiv: 0903.3905*, 2009.

[45] O. Kester *et al.*, Status of the FAIR accelerator facility. *Proceedings of IPAC2014, Dresden, Germany, pp. 2084-2087*, 2014.

[46] Collector Ring Working Group, Technical Design Report on the Collector Ring. *Tech. Rep.*, Nov. 2013.

[47] R. Maier *et al.*, The High-Energy Storage Ring (HESR). *Conf. Proc. C 110328*, 2011.

[48] K. Knie *et al.*, Concept for the antiproton production target at FAIR. *In: Proceedings of IPAC2012, New Orleans, Louisiana, USA*, 2012.

[49] H. Stockhorst *et al.*, Cooling scenario for the HESR complex. *AIP Conf. Proc. 821*, 2006.

[50] R. Maier. The High-Energy Storage Ring (HESR). *Proceedings of 2011 Particle Accelerator Conference. New York, NY, USA, pp. 21042106*, `https://accelconf.web.cern.ch/accelconf/PAC2011/papers/thocn2.pdf`, 2011.

[51] FAIR Joint Core Team. Green Paper: The Modularized Start Version. *Tech. Rep. FAIR*, `http://www.fair-center.eu/fileadmin/fair/publications_FAIR/20FAIR_GreenPaper_2009.pdf`, Oct. 2009.

[52] D. Prasuhn. Status of HESR. *$\bar{P}$ANDA XLIX. Collaboration Meeting (Talk), Darmstadt*, June 2014.

[53] R. Maier *et al.*, Status of stochastic cooling predictions at the HESR. *Conf. Proc. C110904*, 2011.

[54] The $\bar{\text{P}}$ANDA collaboration. Technical Progress Report for: $\bar{\text{P}}$ANDA strong interaction studies with antiprotons. *Tech. Rep.*, Feb. 2005.

[55] The BABAR Collaboration. Observation of a narrow meson decaying to $D_s^+\pi^0$ at a mass of 2.32 GeV/c^2. *Phys. Rev. Lett. 90, 242001*,2003.

[56] D. Besson *et al.*, Observation of a narrow resonance of mass 2.46 GeV/c^2 decaying to $D_s^{*+}\pi^0$ and Confirmation of the D_{sJ}^* (2317) State. *Phys. Rev. D 68, 032002*, 2003.

[57] E. Klempt *et al.*, Baryon spectroscopy. *Rev. Mod. Phys. 82*, 2010.

[58] J. Haidenbauer and G. Krein. The reaction $p\bar{p} \to \Lambda_c\bar{\Lambda}_c$ close to threshold. *Phys. Lett. B 687, pp. 314-319*, 2010.

[59] D. Thompson *et al.*, Evidence for exotic meson production in the reaction $\pi^- p \to \eta\pi^- p$ at 18 GeV/c. *Phys. Rev. Lett. 79, 1630*, 1997.

[60] G. Adams *et al.*, Observation of a new $J^{PC} = 1^{-+}$ exotic state in the reaction $\pi^- p \to \pi^+\pi^-\pi^- p$ at 18 GeV/c. *Phys. Rev. Lett. 81, 5760*, 1998.

[61] A. Abele *et al.*, Exotic $\eta\pi$ state in p^-d annihilation at rest into $\pi^-\pi^0\eta p$ spectator. *Phys. Lett. B 423, 175*, 1998.

[62] C. Morningstar and M. Peardon. Glueball spectrum from an anisotropic lattice study. *Phys. Rev. D 60, 034509*, 1999.

[63] A. V. Belitsky and A. V. Radyushkin. Unraveling hadron structure with generalized parton distributions. *Phys. Rept. 418, 1*, 2005.

[64] X. Ji. Generalized parton distributions. *Ann. Rev. Nucl. Part. Sci. 54, 413*, 2004.

[65] M. Diehl. Generalized parton distributions. *Phys. Rept. 388, 41*, 2003.

[66] J. Ralston and D. E. Soper. Production of dimuons from high energy polarized proton-proton collisions. *Nucl. Phys. B 152, 109*, 1797.

[67] A. B. Larionov, M. Bleicher, A. Gillitzer and M. Strikman. Charmonium production in antiproton-nucleus reactions at low energies. *arXiv:1303.0236 [nucl-th].10.1103/PhysRevC.87.054608*, 2014.

[68] M. Danysz and J. Pniewski. Delayed disintegration of a heavy nuclear fragment, *The London, Edinburgh, and Dublin Philosophical Magazine and Journal of Science, 44, 350, pp. 348350.* DOI: 10.1080/14786440308520318, 1953.

[69] M. Danysz *et al.*, The identification of a double hyperfragment. *Nucl. Phys. 49, pp. 121132.* DOI:10.1016/0029-5582(63)90080-4, 1963.

[70] N. Kaiser and W. Weise. Chiral SU(3) dynamics and Λ-hyperons in the nuclear medium. *Phys. Rev. C 71, 015203*, 2005.

[71] D. Boventura. CAD-Renderings of the $\bar{\text{P}}$ANDA Detector. `https://PANDA-wiki.gsi.de/foswiki/bin/view/Detector/Pictures`, Jan. 2015.

[72] The $\bar{\text{P}}$ANDA collaboration. Technical design report for the $\bar{\text{P}}$ANDA Straw Tube Tracker. *Eur. Phys. J. A 49, 25*, DOI: 10.1140/epja/i2013-13025-8, 2013.

[73] A. Sharma. Properties of some gas mixtures used in tracking detectors. *SLAC-JOURNAL-ICFA 16-3*, 1998.

[74] R. Veenhof. Choosing a gas mixture for the ALICE TPC. *European organization for nuclear research, ALICE-INT-2003-29 version 1.0*, 2003.

[75] The $\bar{\text{P}}$ANDA collaboration. Technical Design Report for $\bar{\text{P}}$ANDA Internal Targets, 2014.

[76] The $\bar{\text{P}}$ANDA collaboration. Technical Design Report for the: $\bar{\text{P}}$ANDA Micro Vertex Detector. `http://arxiv.org/abs/1207.6581`, Aug. 2012.

[77] Mylar polyester film registered trademark of DuPont. `www.dupont.com`.

[78] DESY FLC-TPC. `http://web.archive.org/web/20141122124357/`.

[79] CERN Gas Detectors Development. `http://gdd.web.cern.ch/GDD/`.

[80] M. J. Galuska *et al.*, Hough Transform Based Pattern Recognition for the $\bar{\text{P}}$ANDA Forward Tracking System. *PoS, Bormio2013, 023.* `http://inspirehep.net/record/1265424/`, 2013.

[81] C. Schwarz *et al.*, Particle identification for the $\bar{\text{P}}$ANDA detector. *Nucl. Instr. Meth. A 639, 1*, 2011.

[82] G. Calicy *et al.*, Status of the $\bar{\text{P}}$ANDA Barrel DIRC. *JINST 9, 05, C05060.* `http://stacks.iop.org/1748-0221/9/i=05/a=C05060`, 2014.

[83] J. Schweining. The barrel DIRC detector for the $\bar{\text{P}}$ANDA experiment. *JINST 13, 3, C03004.* `https://arxiv.org/abs/1803.10642`, 2018.

[84] I. Adam *et al.*, The DIRC particle identification system for the BaBar experiment. *Nucl. Instr. Meth. A 538*, 2005.

[85] K. Föhl *et al.*, First particle identification with a Disc-DIRC detector. *Nucl. Instr. Meth. A 732*, 2013.

[86] E. N. Cowie *et al.*, A focussing disc DIRC for $\bar{\text{P}}$ANDA. *Nucl. Instr. Meth. A 639,1*, 2011.

[87] The $\bar{\text{P}}$ANDA collaboration. Technical Design Report for the $\bar{\text{P}}$ANDA Barrel DIRC Detector, 2017.

[88] S. Brunner *et al.*, Time resolution below 100 ps for the SciTil detector of $\bar{\text{P}}$ANDA employing SiPM, *J. Instr. 9*, 2014.

[89] S. Belostotski. Status of FTOF detectors. *Talk at the XLVIII $\bar{\text{P}}$ANDA Collaboration Meeting, GSI*, Mar. 2014

[90] The $\bar{\text{P}}$ANDA collaboration. Technical Design Report for the $\bar{\text{P}}$ANDA Muon System. *Tech. Rep.*. `http://www.fair-center.eu/fileadmin/fair/publications_exp/Muon_TDR.pdf`, 2012.

[91] The $\bar{\text{P}}$ANDA collaboration: Technical Design Report for the $\bar{\text{P}}$ANDA Electromagnetic Calorimeter (EMC). *arXiv: 0810.1216*, Oct. 2008.

[92] J. E. Augustin *et al.*, Discovery of a Narrow Resonance in e^+e^- Annihilation. *Phys. Rev. Lett. 33, 1406*, 1974.

[93] The $\bar{\text{P}}$ANDA collaboration. Technical Design Report for the $\bar{\text{P}}$ANDA Forward Spectrometer Calorimeter. `https://arxiv.org/pdf/1704.02713`, 11 Apr. 2017,

[94] The $\bar{\text{P}}$ANDA collaboration. Technical Design Report for the $\bar{\text{P}}$ANDA Solenoid and Dipole Spectrometer Magnets. *Tech. Rep.*. arXiv: 0907.0169 [physics], May 2009.

[95] K. Korcyl *et al.*, Modelling event building architecture for the triggerless data accquisiton system for $\bar{\text{P}}$ANDA experiment at the HESR facility at FAIR/GSI. *J. Phys. 96, 012027*, 2012.

[96] S. Spataro. Event Reconstruction in the PandaRoot framework 2012. *J. Phys.: Conf. Ser. 396, 022048*. DOI:10.1088/1742-6596/396/2/022048, 2012.

[97] J. Messchendorp. The $\bar{\text{P}}$ANDA collaboration physics coordination report. *$\bar{P}$ANDA collaboration meeting*, June 2017.

[98] R. Kliemet. Simulations with the PANDA Micro-Vertex-Detector. *PhD Thesis, Friedrich-Wilhelms-Universität Bonn*, 2012.

[99] I. Antcheva *et al.*, ROOT- a C++ framework for petabyte data storage, statistical analysis and visualization. *Comput. Phys. Commun., Vol. 182, 6, pp. 1384-1385*. DOI:10.1016/j.cpc.2011.02.008, 2011.

[100] R. Brun and F. Rademakers. ROOT: An object oriented data analysis framework. *Nucl. Instr. Meth. A 389, pp. 81-86*. DOI: 10.1016/S0168-9002(97)00048-X, 1997.

[101] R. Brun and F. Rademakers: ROOT-an object oriented data analysis Framework. *Nucl. Instr. Meth. A 389, 1*, 1997.

[102] R. Brun *et al.*, GEANT3 user guide. *CERN/DD/EE/84-1*, 1987.

[103] A. S. Gostinelli *et al.*, GEANT4: A simulation toolkit. *Nucl. Instr. Meth. A 506*. DOI: 10.1016/S0168-9002(03)01368-8, 2003.

[104] I. Hrivnacova. The GEANT4 virtual Monte Carlo. *J. Phys. Conf. Ser. 396*, 2012.

[105] The ROOT team. ROOT User's Guide. `http://root.cern.ch/drupal/content/root-users-guide-534`, 2013.

[106] T. Sjostrand *et al.*, A brief introduction to PYTHIA 8.1. *Comput. Phys. Commun. 178*, 2008.

[107] M. Alturany *et al.*, The FairRoot framework. *J. Phys.: Conf. Ser., 396, 2.* DOI: 10.1088/1742- 6596/396/2/022001, 2012.

[108] S. Spataro. The PandaRoot framework for simulation, reconstruction and analysis. *J. Phys.: Conf. Ser., 331,3.* DOI: 10.1088/1742-6596/331/3/032031, 2011.

[109] D. J. Lange. The EvtGen particle decay simulation package. *Nucl. Instr. Meth. A 462,12* (2001). DOI: 10.1016/S0168- 9002(01)00089-4, 2001.

[110] A. Capella, U. Sukhatme, C. I. Tan, and J. Tran Thanh Van. Dual parton model. *Phys. Rep., 236, 4-5*, Jan. 1994.

[111] R. E. Kalman. A new approach to linear filtering and prediction problems. transactions of the ASME. *J. Basic. Eng., D 82*, 1960.

[112] J. Rauch and T. Schlüter. GENFIT- a generic track-fitting toolkit. *J. Phys.: Conf. Ser., 608, 1.* DOI: 10.1088/1742- 6596/608/1/012042, 2015.

[113] R. Frühwirth. Application of Kalman filtering to track and vertex fitting. *Nucl. Instr. Meth. A 262, 23, pp. 444-450.* DOI: 10.1016/0168-9002(87)90887-4, 1987.

[114] Rho-A framework for particle physics analysis. `https://code.google.com/p/rhoframework`.

[115] P. Avery. Vertexing and Kinematic Fitting. *Lectures Given at SLAC.* `http://www.phys.ufl.edu/~avery`, Aug. 1998.

[116] A.T. Goritschnig, P. Kroll and W. Schweiger. $p\bar{p} \to \Lambda_c\bar{\Lambda}_c$ within the generalized parton picture first results. arXiv:0811.2661 [hep-ph], 2008.

[117] A. Khodjamirian, Ch. Klein, Th. Mannel and Y.-M. Wang. How much charm can $\bar{\text{P}}$ANDA produce?, *Eur. Phys. J. A 48, 112.* http://dx.doi.org/10.1140/epja/i2012-12031-8, 2012.

[118] A. B. Kaidalov, P. E. Volkovitsky. Binary reactions in pp collisions at intermediate energies. *Zeitschrift fr Physik C Particles and Fields, 63, pp. 517524.* `http://dx.doi.org/10.1007/BF01580332`, 1994.

[119] E. Cazzoli, A. Cnops, P. Connolly, R. Louttit, M. Murtagh, R. Palmer, N. Samios, T. Tso, and H. Williams. Charm and strange particle production in neutrino interactions. *Phys. Rev. Lett. 34, 1125*, 1975.

[120] The CLEO collaboration. Charm physics results from CLEO. arXiv:hep-ex/0305006, 2003.

[121] The BABAR collaboration. Charm baryon results from BaBar. *AIP Conf. Proc. 1374, 577*, 2011.

[122] Y. Kato. Study of the charmed strange baryons at Belle. *Proc. Sci., Hadron 2013 053*, 2014.

[123] J. Haidenbauer and G. Krein. Charm production in antiproton-proton annihilation. *Few-Body Syst 50, 183*. DOI: 10.1007/s00601-010-0126-4, 2011.

[124] R. Shyam and H. Lenske. Reaction $p\bar{p} \rightarrow \Lambda_c\bar{\Lambda}_c$ within an effective Lagrangian mode. *Phys. Rev. D 90, 014017*. DOI:10.1103/PhysRevD.90.014017, 2014.

[125] M. Tanabashi *et al.*, (Particle Data Group). Review of particle physics. *Phys. Rev. D 98, 030001*, 2018.

[126] A.B. Kaidalov, P.E. Volkovitsky, J. Sov. Quark and diquark fragmentation functions in the model of quark gluon strings. *Nucl. Phys. 35, 909*, 1982.

[127] J. Haidenbauer and G. Krein. The reaction $p\bar{p} \rightarrow \Lambda_c\bar{\Lambda}_c$, close to threshold. *Phys. Lett. B 687, 314*, 2010.

[128] R. Anders *et al.*, EvtGen: A Monte Carlo Generator for B-Physics. `http://robbep.home.cern.ch/robbep/EvtGen/GuideEvtGen.pdf`, 2005.

[129] R. Kalman. A new approach to linear filtering and prediction problems. *Transactions of the ASMEJ. Basic. Eng. D 82*, 1960.

[130] A. Apostolou. Particle-identification capability of the straw tube tracker and feasibility studies for open-charm production with $\bar{\text{P}}$ANDA. *PhD thesis. University of Groningen*, 2018.

[131] W. R. Leo. Techniques for nuclear and particle physics experiments. Springer-Verlag, 1987.

[132] F. Sauli. Instrumentation in high energy physics. Advanced series on directions in high energy physics, *World Scientific Publishing, Vol. 9*, 1992.

[133] F. Sauli. Principles of operation of multiwire proportional and drift chambers, *CERN 77, 09*, 1977.

[134] The $\bar{\text{P}}$ANDA collaboration. Technical Design Report for the: $\bar{\text{P}}$ANDA Straw Tube Tracker. *Eur. Phys. J. A 49, 25*, 2013.

[135] H. H. Adam *et al.*, Proposal for the wide angle shower apparatus (WASA) at COSY. *arXiv:nucl-ex 0411038*, 2004.

[136] R. Maier. Cooler synchrotron COSY: Performance and perspectives. *Nucl. Instrum. Meth. A390*. DOI: 10.1016/S0168-9002(97)00324-0, 1997.

[137] IKP 2013 annual report. `http://www.fz-juelich.de/ikp/EN/Service/Download/Downloads/jahresbericht_2013.pdf`, 2013.

[138] G. Avolio *et al.*, Test of the first BIL tracking chamber for the ATLAS muon spectrometer. *Nucl. Instr. and Meth. A 523*, 2004.

[139] A. Biscossa *et al.*, Monitored drift tubes in ATLAS. *Nucl. Instr. and Meth. A 419*, 1998.

[140] F. James. MINUIT function minimization and error analysis, *CERN Program Library entry D506*. `https://root.cern.ch/sites/d35c7d8c.web.cern.ch/files/minuit.pdf`, 2013.

[141] W. Erven, P. Kulessa, P. Marciniewski, P. Wüstner, G. Kemmerling. Berichte zum Datenerfassungssystem für physikalische Experimente, Forschungszentrum Jülich Zentrallabor für Elektronik. *Private communication.*

[142] W. Erven *et al.*, Resolution and efficiency of the straw tracker for COSY-TOF. *IKP Annual Report 2004, Jülich* , 2005.

[143] The BABAR Collaboration. The BABAR detector. *Nucl. Instrum. and Meth. A479, 1*, 2002.

[144] The BESIII collaboration. The construction of the BESIII experiment. *Nucl. Instrum. and Meth. A614, 345*, 2010.

[145] The HADES Collaboration. The High-Acceptance Dielectron Spectrometer HADES. *Eur. Phys. J. A41, 243*, 2009.

[146] S. Bianco. Tracking and vertex reconstruction with the $\bar{\text{P}}$ANDA Micro Vertex Detector. *PhD thesis. Universität Bonn*, 2013.